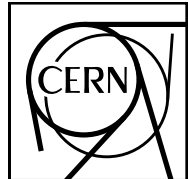


EUROPEAN ORGANISATION FOR NUCLEAR RESEARCH (CERN)



CERN-PH-EP-2014-143

Submitted to: JHEP

Search for top squark pair production in final states with one isolated lepton, jets, and missing transverse momentum in $\sqrt{s} = 8 \text{ TeV}$ pp collisions with the ATLAS detector

The ATLAS Collaboration

Abstract

The results of a search for top squark (stop) pair production in final states with one isolated lepton, jets, and missing transverse momentum are reported. The analysis is performed with proton–proton collision data at $\sqrt{s} = 8 \text{ TeV}$ collected with the ATLAS detector at the LHC in 2012 corresponding to an integrated luminosity of 20 fb^{-1} . The lightest supersymmetric particle (LSP) is taken to be the lightest neutralino which only interacts weakly and is assumed to be stable. The stop decay modes considered are those to a top quark and the LSP as well as to a bottom quark and the lightest chargino, where the chargino decays to the LSP by emitting a W boson. A wide range of scenarios with different mass splittings between the stop, the lightest neutralino and the lightest chargino are considered, including cases where the W bosons or the top quarks are off-shell. Decay modes involving the heavier charginos and neutralinos are addressed using a set of phenomenological models of supersymmetry. No significant excess over the Standard Model prediction is observed. A stop with a mass between 210 and 640 GeV decaying directly to a top quark and a massless LSP is excluded at 95% confidence level, and in models where the mass of the lightest chargino is twice that of the LSP, stops are excluded at 95% confidence level up to a mass of 500 GeV for an LSP mass in the range of 100 to 150 GeV. Stringent exclusion limits are also derived for all other stop decay modes considered, and model-independent upper limits are set on the visible cross-section for processes beyond the Standard Model.

© 2014 CERN for the benefit of the ATLAS Collaboration.

Reproduction of this article or parts of it is allowed as specified in the CC-BY-3.0 license.

Contents

1	Introduction	2
2	Analysis strategy	4
3	The ATLAS detector	5
4	Trigger and data collection	6
5	Simulated samples	7
5.1	Background samples	8
5.2	Signal samples	8
6	Physics object reconstruction and discriminating variables	10
6.1	Physics object reconstruction	10
6.2	Tools to discriminate signal from background	14
7	Signal selections	16
7.1	Event preselection	17
7.2	Selections for the $\tilde{t}_1 \rightarrow t\tilde{\chi}_1^0$ decay	18
7.3	Selections for the $\tilde{t}_1 \rightarrow b\tilde{\chi}_1^\pm$ decay	21
7.4	Selections for the mixed, three- and four-body decays	27
8	Background estimates	28
8.1	Control regions	29
8.2	Validation	32
9	Systematic uncertainties	36
10	Results	39
11	Summary and conclusions	45
12	Acknowledgements	47
A	Detailed description of the discriminating variables	62
B	Background fit results	65

1 Introduction

The hierarchy problem [1–4] has gained additional attention with the observation of a new particle consistent with the Standard Model (SM) Higgs boson [5, 6] at the LHC [7]. Supersymmetry (SUSY) [8–16], which extends the SM by introducing supersymmetric partners for all SM particles, provides an elegant solution to the hierarchy problem. The partner particles have identical quantum numbers except for a half-unit difference in spin. The superpartners of the left- and right-handed top quarks, \tilde{t}_L and \tilde{t}_R , mix to form the two mass eigenstates \tilde{t}_1 and \tilde{t}_2 , where \tilde{t}_1 (top squark or stop) is the lighter one. If the supersymmetric partners of the top quarks have masses $\lesssim 1$ TeV, loop diagrams involving top quarks, which are the dominant contribution to the divergence of the Higgs boson mass, can be largely cancelled [17–24]. Significant mass splitting between \tilde{t}_1 and \tilde{t}_2 is possible due to the large top Yukawa coupling¹. Furthermore, effects of the renormalisation group equations are strong for the third generation squarks, usually driving their masses significantly lower than those of the other generations. These considerations suggest a light stop which, together with the stringent LHC limits excluding other coloured supersymmetric particles up to masses at the TeV level, motivates dedicated stop searches.

SUSY models can violate the conservation of baryon number and lepton number, resulting in a proton lifetime shorter than current experimental limits [25]. This is commonly solved by introducing a multiplicative quantum number called *R*-parity, which is 1 and -1 for all SM and SUSY particles, respectively. A generic *R*-parity-conserving minimal supersymmetric extension of the SM (MSSM) [17, 26–29] predicts pair production of SUSY particles and the existence of a stable lightest supersymmetric particle (LSP). In a large variety of SUSY models, the lightest neutralino² ($\tilde{\chi}_1^0$) is the LSP, which is also the assumption throughout this paper. Since the $\tilde{\chi}_1^0$ interacts only weakly it is a candidate for dark matter.

The stop can decay into a variety of final states, depending amongst other things on the SUSY particle mass spectrum, in particular on the masses of the stop and the lightest neutralino. Figure 1 illustrates the simplest decay modes as a function of the stop and LSP masses. In the rightmost wedge, the stop mass is greater than the sum of the top quark and the LSP masses, hence the decay $\tilde{t}_1 \rightarrow t\tilde{\chi}_1^0$ is kinematically allowed. A lighter stop can undergo a three-body decay $\tilde{t}_1 \rightarrow bW\tilde{\chi}_1^0$ if the stop mass is still above the $b + W + \tilde{\chi}_1^0$ mass. For an even lighter stop, the decay proceeds via a four-body process $\tilde{t}_1 \rightarrow bf'f'\tilde{\chi}_1^0$, where f and f' are two distinct fermions, or flavour-changing neutral current (FCNC) processes, such as the loop-suppressed $\tilde{t}_1 \rightarrow c\tilde{\chi}_1^0$. If supersymmetric particles other than the $\tilde{\chi}_1^0$ are lighter than the stop, then additional decay modes can open up. The stop decay to a bottom quark and the lightest chargino ($\tilde{t}_1 \rightarrow b\tilde{\chi}_1^\pm$) is an important example,

¹The masses of the \tilde{t}_1 and \tilde{t}_2 are given by the eigenvalues of the stop mass matrix. The stop mass matrix involves the top-quark Yukawa coupling in the off-diagonal elements, which typically induces a large mass splitting. The stop mass matrix is diagonalised by the stop mixing matrix, which gives the \tilde{t}_L and \tilde{t}_R components of the mass eigenstates \tilde{t}_1 and \tilde{t}_2 .

²The charginos $\tilde{\chi}_{1,2}^\pm$ and neutralinos $\tilde{\chi}_{1,2,3,4}^0$ are the mass eigenstates formed from the linear superposition of the charged and neutral SUSY partners of the Higgs and electroweak gauge bosons (higgsinos, winos and binos).

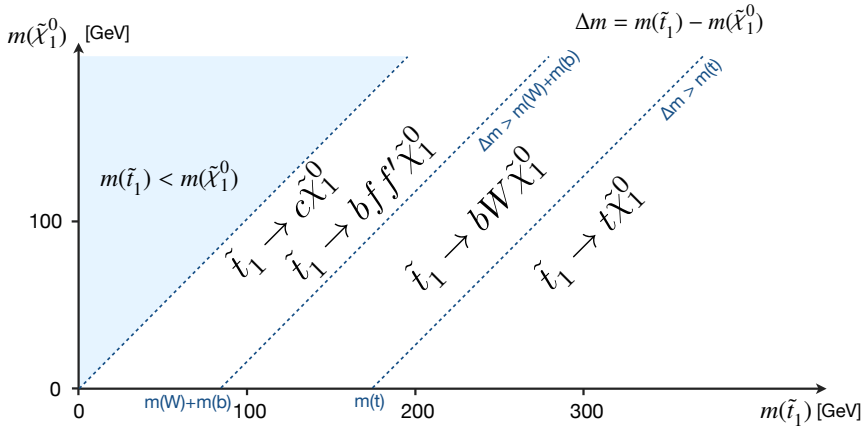


Figure 1. Illustration of stop decay modes in the plane spanned by the masses of the stop (\tilde{t}_1) and the lightest neutralino ($\tilde{\chi}_1^0$), where the latter is assumed to be the lightest supersymmetric particle. Stop decays to supersymmetric particles other than the lightest supersymmetric particle are not displayed.

where the $\tilde{\chi}_1^\pm$ can decay to the lightest neutralino by emitting an on- or off-shell W boson ($\tilde{\chi}_1^\pm \rightarrow W^{(*)}\tilde{\chi}_1^0$). The $\tilde{t}_1 \rightarrow b\tilde{\chi}_1^\pm$ decay is considered for a stop mass above around 100 GeV since the LEP limit on the lightest chargino is $m_{\tilde{\chi}_1^\pm} > 103.5$ GeV [30].

This article presents a search for direct \tilde{t}_1 pair production in final states with exactly one isolated charged lepton (electron or muon,³ henceforth referred to simply as ‘leptons’), several jets, and a significant amount of missing transverse momentum, the magnitude of which is referred to as E_T^{miss} . The lepton arises from the decay of either a real or a virtual W boson, and the potentially large E_T^{miss} is generated by the two undetected LSPs and neutrino(s). All stop decay modes described above except for the FCNC modes are considered, as illustrated in figure 2. With several decay modes kinematically available, the \tilde{t}_1 decay branching ratio is determined by factors including the stop mixing matrix and the field content of the neutralino/chargino sector. Results are mainly based on simplified models that have 100% branching ratio to one or a pair of these specific decay chains. In addition, phenomenological MSSM (pMSSM) [31] models are used to study the sensitivity to realistic scenarios where more complex decay chains are present alongside the simpler ones.

Searches for direct \tilde{t}_1 pair production have previously been reported by the ATLAS [32–38] and CMS [39–43] collaborations, as well as by the CDF and DØ collaborations (for example refs. [44, 45]) and the LEP collaborations [46]. Indirect searches for stops, mediated by gluino pair production, have been reported by the ATLAS [47–50] and CMS [39, 40, 51–55] collaborations.

³Electrons and muons from τ decays are included.

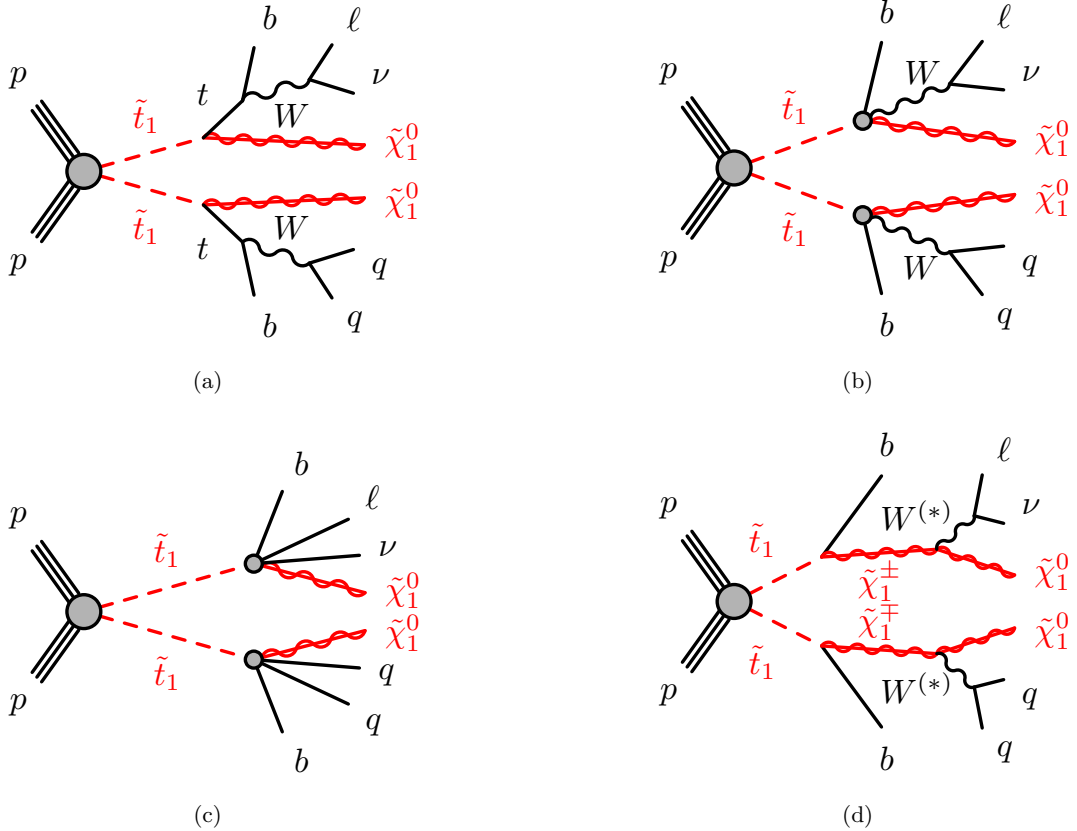


Figure 2. Diagrams illustrating the considered signal scenarios, which are referred to as (a) $\tilde{t}_1 \rightarrow t\tilde{\chi}_1^0$, (b) $\tilde{t}_1 \rightarrow bW\tilde{\chi}_1^0$ (three-body), (c) $\tilde{t}_1 \rightarrow bff'\tilde{\chi}_1^0$ (four-body), (d) $\tilde{t}_1 \rightarrow b\tilde{\chi}_1^\pm$. Furthermore, a non-symmetric decay mode where each \tilde{t}_1 can decay via either $\tilde{t}_1 \rightarrow t\tilde{\chi}_1^0$ or $\tilde{t}_1 \rightarrow b\tilde{\chi}_1^\pm$ is considered (not shown). In these diagrams, the charge-conjugate symbols are omitted for simplicity; all scenarios begin with a top squark–antisquark pair. The three-body and four-body decays are assumed to proceed through an off-shell top quark, and an off-shell top quark followed by an off-shell W boson, respectively.

2 Analysis strategy

Searching for \tilde{t}_1 pair production in the various decay modes and over a wide range of stop masses requires different analysis approaches. The \tilde{t}_1 pair production cross-section falls rapidly with increasing stop mass $m_{\tilde{t}_1}$: for the range targeted by this search, $m_{\tilde{t}_1} \sim 100\text{--}700\,\text{GeV}$, the cross-section at $\sqrt{s} = 8\,\text{TeV}$ proton–proton (pp) collisions decreases from 560 pb to 8 fb. While the various \tilde{t}_1 decay modes considered all have identical final state objects — one electron or muon accompanied by one neutrino (or more for a leptonic τ decay), two jets originating from bottom quarks (b -jets), two light-flavour jets, and two LSPs — their kinematic properties change significantly for the different decay modes and as a function of the masses of the stop, LSP, and lightest chargino (if present). The search presented in this paper is based on 15 dedicated analyses that target the various

scenarios. The identification of b -jets (b -tagging) is utilised in the event selections and for constructing kinematic variables. The search for a heavy stop exploits a specialised technique, which reconstructs several decay products in a single large-radius (large- R) jet. Low-momentum leptons (referred to as soft leptons) are reconstructed and identified to enhance the sensitivity for $\tilde{t}_1 \rightarrow b\tilde{\chi}_1^\pm$ decays where the $\tilde{\chi}_1^0$ and $\tilde{\chi}_1^\pm$ states are close in mass. These and other tools and variables to discriminate signal from background, described in section 6, are used to design sets of requirements for the event selection. Each of these sets of requirements is referred to as a signal region (SR), and is optimised to target one or more signal scenarios. Furthermore, two different analysis techniques are employed, which are referred to as ‘cut-and-count’ and ‘shape-fit’. The former is based on counting events in a single region of phase space (bin), while the latter employs several bins. By utilising different signal-to-background ratios in the various bins, shape-fits enhance the search sensitivity in challenging scenarios, where it is particularly difficult to separate signal from background. All SRs are described in section 7.

The dominant background in most SRs arises from top quark pair production ($t\bar{t}$) where both W bosons decay leptonically (dileptonic $t\bar{t}$) but one of the leptons is not identified, is outside the detector acceptance, or is a hadronically decaying τ lepton. The sub-leading background for most SRs stems from W +jets production. As part of each analysis, the $t\bar{t}$ and W +jets backgrounds are estimated using dedicated control regions (CRs), making the analysis more robust against potential mis-modelling effects in simulated events and reducing the uncertainties on the background estimates. Other small backgrounds are estimated using simulation only. Dedicated samples are used to validate the background predictions. The background estimation including the definition of all CRs is detailed in section 8.

The analysis results are based on maximum likelihood fits, which include the CRs to simultaneously normalise the $t\bar{t}$ and W +jets backgrounds. Systematic uncertainties due to theoretical and experimental effects are considered for all background and signal processes, and are described in section 9. The final results and interpretations, both in terms of model-dependent exclusion limits on the masses of relevant SUSY particles and model-independent upper limits on the number of beyond-SM events, are presented in section 10.

3 The ATLAS detector

The ATLAS experiment [56] is a multi-purpose particle physics detector with nearly 4π steradian coverage in solid angle. It consists of an inner detector of tracking devices surrounded by a thin superconducting solenoid, electromagnetic and hadronic calorimeters, and a muon spectrometer in a toroidal magnetic field. The inner detector, in combination with the 2 T axial field from the solenoid, provides precision tracking and momentum measurement of charged particles up to $|\eta| = 2.5$ and allows efficient b -jet identification.⁴ It consists

⁴ATLAS uses a right-handed coordinate system with its origin at the nominal interaction point in the centre of the detector and the z -axis along the beam pipe. Cylindrical coordinates (r, ϕ) are used in the transverse plane, ϕ being the azimuthal angle around the beam pipe. The pseudorapidity η is defined in

of a silicon pixel detector, a semiconductor microstrip detector and a straw-tube tracker which also provides transition radiation measurements for electron identification. High-granularity liquid-argon (LAr) sampling electromagnetic calorimeters cover the pseudorapidity range $|\eta| < 3.2$. The hadronic calorimeter system is based on two different technologies, a scintillator-tile sampling calorimeter ($|\eta| < 1.7$) and a LAr sampling calorimeter ($1.5 < |\eta| < 3.2$). LAr calorimeters in the most forward region ($3.1 < |\eta| < 4.9$) provide electromagnetic and hadronic measurements. The muon spectrometer has separate trigger and high-precision tracking chambers, the former provide trigger coverage up to $|\eta| = 2.4$ while the latter provide muon identification and momentum measurements for $|\eta| < 2.7$. Events are selected by a three-level trigger system [57], the first level (L1) is implemented in customised hardware while the two high-level triggers (HLT) are software-based.

4 Trigger and data collection

The data used in this analysis were collected from March to December 2012 with the LHC operating at a pp centre-of-mass energy of $\sqrt{s} = 8$ TeV. After application of beam, detector and data quality requirements, the total integrated luminosity is 20.3 fb^{-1} with an uncertainty of 2.8%. The uncertainty is derived, following the methodology detailed in ref. [58], from a preliminary calibration of the luminosity scale from beam-separation scans performed in November 2012.

The dataset was recorded using three different types of triggers based on requiring either an electron, a muon, or large E_T^{miss} . The single-electron trigger identifies electrons based on the presence of an energy cluster in the electromagnetic calorimeter with a shower shape consistent with that of an electron, low hadronic leakage, and a matching track in the inner detector. The HLT threshold⁵ on the energy deposit transverse to the beam (E_T) is 24 GeV. An electron isolation criterion at the HLT requires the scalar sum of the transverse momenta (p_T) of tracks within a cone of radius $\Delta R = 0.2$ around the electron (excluding the electron itself) to be less than 10% of the electron E_T . The single-muon trigger identifies muons using tracks reconstructed in the muon spectrometer and inner detector. The p_T threshold at the HLT is 24 GeV. An isolation criterion at the HLT requires the scalar sum of the p_T of tracks within a cone of radius $\Delta R = 0.2$ around the muon (excluding the muon itself) to be less than 12% of the muon p_T . To recover some of the small efficiency loss for high- p_T leptons, events were also collected using complementary single-lepton triggers. These triggers have less stringent shower-shape requirements and no hadronic leakage criterion for electrons, and no isolation criteria, but have an increased E_T (p_T) threshold of 60 GeV (36 GeV) for electrons (muons). Corrections are applied to the simulated samples to account for small differences between data and simulation in the lepton trigger efficiencies.

terms of the polar angle θ by $\eta = -\ln \tan(\theta/2)$, and the angular separation ΔR in the η - ϕ space is defined as $\Delta R = \sqrt{(\Delta\eta)^2 + (\Delta\phi)^2}$.

⁵The trigger thresholds refer to lower requirements on the given quantity, and the HLT thresholds are always more stringent than the corresponding L1 thresholds.

The E_T^{miss} trigger is based on the vector sum of the transverse energies deposited in projective calorimeter trigger towers. A more refined calculation based on the vector sum of all calorimeter cells above noise is made at the HLT. The trigger E_T^{miss} threshold at the HLT is 80 GeV, and it is fully efficient for offline-calibrated $E_T^{\text{miss}} > 150$ GeV in signal-like events. At the beginning of the 2012 data-taking, the E_T^{miss} trigger used in this analysis was disabled for the first three bunch crossings of every bunch train, causing a loss of 0.2 fb^{-1} in integrated luminosity.

Candidate events in the electron (muon) channel were collected using a logical-OR combination of the single-electron (single-muon) and E_T^{miss} triggers. Since the single-lepton trigger thresholds are too high for the soft-lepton selection, these candidate events were recorded using only the E_T^{miss} trigger. Consequently, the effective dataset for the soft-lepton selections amounts to an integrated luminosity of 20.1 fb^{-1} . All results quote a rounded value of 20 fb^{-1} , while inside the analysis the appropriate integrated luminosity values are used. The efficiency of the E_T^{miss} and lepton triggers are measured with $W \rightarrow \mu\nu$ and $Z \rightarrow \ell\ell$ data samples, respectively. In all cases the combined trigger efficiency is greater than 98% for simulated signal events satisfying the selection criteria for the analyses described in sections 7–8.

5 Simulated samples

Samples of Monte Carlo (MC) simulated events are used for the description of the background and to model the SUSY signals. As detailed below, the samples are generated with either POWHEG-R2129 [59], ACERMC-3.8 [60], MADGRAPH-5.1.4.8 [61], SHERPA-1.4.1 [62] or HERWIG++ 2.5.2 [63]. All POWHEG and SHERPA samples use the next-to-leading-order (NLO) parton distribution function (PDF) set CT10 [64], while samples generated with ACERMC, MADGRAPH or HERWIG++ use the CTEQ6L1 [65] PDF set. The ATLAS Underlying Event Tune 2B [66] is used for all MADGRAPH samples, while the samples generated with POWHEG or ACERMC use the PERUGIA 2011C [67] tune and samples generated with HERWIG++ use UEEE3 [68]. The SHERPA generator has an integrated underlying event tune. The fragmentation and hadronisation for the POWHEG, ACERMC, and MADGRAPH samples is performed with PYTHIA-6.426 [69], while SHERPA and HERWIG++ use their own built-in models.

The samples are processed with either a detector simulation [70] using GEANT4 [71] or a fast simulation framework where the showers in the electromagnetic and hadronic calorimeters are simulated using a parameterised description [72] and GEANT4 is used for the rest of the detector. The fast simulation has been validated against full GEANT4 simulation for several signal models and for the main background, $t\bar{t}$ production. All samples are produced with varying numbers of simulated minimum-bias interactions, generated with PYTHIA-8.160 [73], overlaid on the hard-scattering event to account for multiple pp interactions in the same or nearby bunch crossings (pileup). The average number of interactions per bunch crossing is reweighted to match the distribution in data that varies between approximately 10 and 30.

5.1 Background samples

A sample of $t\bar{t}$ events is generated with POWHEG using a top quark mass $m_t = 172.5$ GeV. The same top quark mass is used when simulating other signal or background processes involving top quarks. To account for discrepancies between data and simulated $t\bar{t}$ events, the simulated sample is reweighted as a function of the p_T of the $t\bar{t}$ system; the weights are based on the ATLAS measurement of the differential $t\bar{t}$ cross-section at 7 TeV, following the method described in ref. [74]. Single top quark production in the s -channel and the Wt mode are also generated with POWHEG, while the t -channel process is generated with ACERMC. In Wt production, the interference with $t\bar{t}$ at NLO in quantum chromodynamics (QCD) is treated by the diagram removal scheme [75]. Associated production of $t\bar{t}$ and vector bosons (W , Z and WW) as well as single top production in association with a Z boson, are generated with MADGRAPH with up to two additional partons. Samples of W +jets and Z/γ^* + jets are produced with SHERPA, containing up to four additional partons and the correct treatment of bottom and charm quark masses. The diboson processes (WW , ZZ and WZ) are also generated with SHERPA.

The processes are normalised using theoretical inclusive cross-sections, including higher-order QCD corrections where available. The $t\bar{t}$ production cross-section is calculated at next-to-next-to-leading order (NNLO) in QCD including resummation of next-to-next-to-leading logarithmic (NNLL) soft gluon terms with top++2.0 [76–81]. Cross-sections for single top quark production are calculated to approximate NLO+NNLL precision [82–84]. The production of $t\bar{t}$ in association with vector bosons is calculated at NLO [85, 86], while the production of a single top quark in association with a Z boson is normalised to the LO cross-sections from the generator, because NLO calculations are only available for t -channel production [87]. The cross-sections for the production of W and Z bosons are calculated with DYNNLO [88]. The production cross-sections for electroweak diboson production are calculated at NLO with MCFM [89, 90]. The $t\bar{t}$, single top, W , Z , and diboson calculations use the MSTW2008 NNLO PDF set [91], while the cross-sections for $t\bar{t}$ in association with a vector boson use the MSTW2008 NLO (W) or CTEQ6.6M [92] (Z) PDF set. The cross-sections for $t\bar{t}$ and W production are used for the optimisation of the selections, while for the final results the two processes are normalised to data in control regions.

5.2 Signal samples

Signal samples of top squark–antisquark pairs are generated with different stop decay and mass configurations. The first scenario assumes the $\tilde{t}_1 \rightarrow t\tilde{\chi}_1^0$ decay with a branching ratio (\mathcal{BR}) of 100%. The samples are generated with HERWIG++ in a grid across the plane of \tilde{t}_1 and $\tilde{\chi}_1^0$ masses with a spacing of 50 GeV for most of the plane; the grid is more finely sampled towards the diagonal region where $m_{\tilde{t}_1}$ approaches $m_t + m_{\tilde{\chi}_1^0}$. The \tilde{t}_1 is chosen to be mostly the partner of the right-handed top quark⁶ and the $\tilde{\chi}_1^0$ to be almost pure bino. This choice is consistent with a large \mathcal{BR} for the given \tilde{t}_1 decay. Different hypotheses on the left/right mixing in the stop sector and the nature of the neutralino lead to different

⁶ The \tilde{t}_R component is given by the off-diagonal entry of the stop mixing matrix. Here, this matrix is set with (off-) diagonal entries of approximately (± 0.83) 0.55.

acceptance values. The acceptance is affected because the polarisation of the top quark changes as a function of the field content of the supersymmetric particles, which impacts the boost of the lepton in the top quark decay. A subset of models where the \tilde{t}_1 is purely \tilde{t}_L are studied to quantify this effect.

The second signal scenario assumes the $\tilde{t}_1 \rightarrow b\tilde{\chi}_1^\pm \rightarrow bW^{(*)}\tilde{\chi}_1^0$ decay with a \mathcal{BR} of 100%.⁷ The stop pairs are always generated with MADGRAPH, while for the \tilde{t}_1 decay either MADGRAPH or PYTHIA is employed. For models where the W boson is on-shell, the full \tilde{t}_1 decay is performed by MADGRAPH, while PYTHIA is used to decay the \tilde{t}_1 in models where the W is off-shell. In the latter case, generating the full event with MADGRAPH would be computationally too expensive. Seven two-dimensional planes are defined to probe the three-dimensional parameter space of the \tilde{t}_1 , $\tilde{\chi}_1^\pm$, and $\tilde{\chi}_1^0$ masses. The typical grid spacing is 50 GeV; higher grid densities are generated in regions where a rapid change of sensitivity is expected. The boundary conditions are derived from the LEP chargino mass limit of 103.5 GeV [30], and by requiring the $\tilde{\chi}_1^\pm$ mass to be below the \tilde{t}_1 mass. Six out of the seven planes span the \tilde{t}_1 and $\tilde{\chi}_1^0$ masses. The first plane sets the chargino mass to twice the LSP mass ($m_{\tilde{\chi}_1^\pm} = 2m_{\tilde{\chi}_1^0}$), motivated by the pattern in GUT-scale models with gaugino universality. The second and third planes fix the chargino mass to be above ($m_{\tilde{\chi}_1^\pm} = 150$ GeV) or close to ($m_{\tilde{\chi}_1^\pm} = 106$ GeV) the chargino mass limit, respectively. In the fourth and fifth planes the chargino mass and neutralino mass are relatively close, $m_{\tilde{\chi}_1^\pm} - m_{\tilde{\chi}_1^0} = 5$ GeV and $m_{\tilde{\chi}_1^\pm} - m_{\tilde{\chi}_1^0} = 20$ GeV, respectively; small mass differences are motivated by higgsino-like states. The sixth plane sets the chargino mass to be slightly below the stop mass, $m_{\tilde{\chi}_1^\pm} = m_{\tilde{t}_1} - 10$ GeV. The last plane fixes the stop mass, $m_{\tilde{t}_1} = 300$ GeV, while varying the $\tilde{\chi}_1^\pm$ and $\tilde{\chi}_1^0$ masses. The samples in all planes assume that the \tilde{t}_1 is a \tilde{t}_L state. The $\tilde{t}_1 \rightarrow b\tilde{\chi}_1^\pm$ branching ratio might not reach 100% in the MSSM if the $\tilde{t}_1 \rightarrow t + \tilde{\chi}_1^0/\tilde{\chi}_2^0$ decays are kinematically allowed, but high branching ratios can occur in the allowed parameter space, such as for the above choices of particle field content.

The $\mathcal{BR} = 100\%$ assumption is relaxed in a third signal scenario where a stop can decay either via $\tilde{t}_1 \rightarrow t\tilde{\chi}_1^0$ or via $\tilde{t}_1 \rightarrow b\tilde{\chi}_1^\pm$. For this purpose, ‘asymmetric’ samples are generated where in each event one stop is forced to decay via one and the second stop via the other decay mode. The signal plane as a function of the \mathcal{BR} can be probed by combining, with appropriate reweighting, the asymmetric samples with the two $\mathcal{BR} = 100\%$ samples for the $\tilde{t}_1 \rightarrow t\tilde{\chi}_1^0$ and $\tilde{t}_1 \rightarrow b\tilde{\chi}_1^\pm$ decays. The asymmetric samples are generated with the same generator settings used for the other $\tilde{t}_1 \rightarrow b\tilde{\chi}_1^\pm$ samples, except for using the maximum stop mixing angle (yielding equal components of \tilde{t}_L and \tilde{t}_R) since the stop mixing is directly related to the \mathcal{BR} . The mass points generated are identical to those for the $m_{\tilde{\chi}_1^\pm} = 2m_{\tilde{\chi}_1^0}$ scenario.

The three- and four-body stop decay modes, $\tilde{t}_1 \rightarrow bW\tilde{\chi}_1^0$ and $\tilde{t}_1 \rightarrow bff'\tilde{\chi}_1^0$ respectively, are relevant for a relatively light stop, as shown in figure 1. Samples for each scenario are generated with the assumption of $\mathcal{BR} = 100\%$. The three-body samples are produced with HERWIG++, which performs the full matrix element calculation of the three-body decay, using the same settings as for the $\tilde{t}_1 \rightarrow t\tilde{\chi}_1^0$ decay mode. The four-body decay mode

⁷ All possible decays of the (possibly virtual) W boson are considered.

is generated with MADGRAPH interfaced with PYTHIA for the \tilde{t}_1 decay and for parton showering, and with up to one additional parton. The four-body decay itself is forced to proceed via a virtual W boson. The \tilde{t}_1 and $\tilde{\chi}_1^0$ mass parameters are varied with a grid spacing between 25 and 50 GeV.

Signal cross-sections are calculated in the MSSM at NLO, including the resummation of soft gluon emission at next-to-leading-logarithmic accuracy (NLO+NLL) [93–95]. The nominal cross-section and the uncertainty are taken from an envelope of cross-section predictions using different PDF sets and factorisation and renormalisation scales, as described in ref. [96]. The \tilde{t}_1 pair production cross-section obtained using this prescription is (5.6 ± 0.8) pb for $m_{\tilde{t}_1} = 250$ GeV, and (0.025 ± 0.004) pb for $m_{\tilde{t}_1} = 600$ GeV.

Although the simplified models described above can probe large regions of the allowed SUSY parameter space, more realistic SUSY models can feature more complex stop decays involving the heavier charginos and neutralinos. To study the sensitivity of the various analyses to these well-motivated scenarios, the pMSSM models described in ref. [97] are used. These models produce a Higgs boson in the mass range ($m_h = 126 \pm 3$ GeV), saturate the WMAP relic density [98] and produce values of fine-tuning no worse than 1 part in 100 using the measure proposed by Barbieri, Giudice and Ellis et al. [23, 99]. In all models the $\tilde{\chi}_1^0$ is the LSP. To investigate the impact of varying parameters other than the stop and LSP mass while at the same time avoiding the processing of a large number of events, only three different \tilde{t}_1 and $\tilde{\chi}_1^0$ mass regions are considered. Only models where both $\tilde{t}_1 \rightarrow t\tilde{\chi}_1^0$ and $\tilde{t}_1 \rightarrow b\tilde{\chi}_1^\pm$ are kinematically allowed are used. This serves to remove the models which have a branching ratio of 100% for only one decay mode, as these regions of parameter space are already probed by the simplified models. This results in a total of 27 models, for which top squark–antisquark pair events are generated with HERWIG++ and processed with the fast simulation. Some details of the models are given in table 1. By keeping the stop and LSP masses fixed, the impact on the sensitivity from varying other parameters can be studied, such as the branching ratios to the heavier charginos and neutralinos. The sensitivity for pMSSM models can then be compared to that obtained in the simplified models with the corresponding stop and LSP masses.

6 Physics object reconstruction and discriminating variables

6.1 Physics object reconstruction

The reconstruction and identification of all final state objects used in this search, such as vertices, jets, leptons, and missing transverse momentum, is described in the following. Two sets of lepton identification criteria are utilised. One set defines the leptons used in the overlap removal procedure with jets and other objects and to veto events with more than one lepton. The second set imposes tighter identification criteria, and is used to select the primary lepton in the event.

The reconstructed primary vertex is required to be consistent with the beam diamond envelope and to have at least five associated tracks with $p_T > 0.4$ GeV [100]. If there are multiple primary vertices in an event, the vertex with the largest summed p_T^2 of the

\tilde{t}_1	Mass [GeV]					Branching ratio $\tilde{t}_1 \rightarrow$					$[T_{11}]^2$	$[N_{11}]^2$
	$\tilde{\chi}_1^0$	$\tilde{\chi}_2^0$	$\tilde{\chi}_3^0$	$\tilde{\chi}_1^\pm$	$\tilde{\chi}_2^\pm$	$t\tilde{\chi}_1^0$	$t\tilde{\chi}_2^0$	$t\tilde{\chi}_3^0$	$b\tilde{\chi}_1^\pm$	$b\tilde{\chi}_2^\pm$		
404	40	221	230	220	1073	0.09	0.01	0.09	0.81	0.00	0.53	0.96
404	44	324	445	325	471	0.16	0.00	0.00	0.84	0.00	0.98	0.99
407	46	368	372	367	1515	0.74	0.00	0.00	0.26	0.00	0.02	0.98
408	49	187	207	188	376	0.02	0.31	0.23	0.41	0.04	0.97	0.95
409	39	211	212	206	1768	0.05	0.24	0.02	0.68	0.00	0.56	0.95
409	49	180	190	179	795	0.02	0.22	0.17	0.59	0.00	0.99	0.94
410	40	232	253	234	427	0.11	0.25	0.00	0.64	0.00	0.96	0.97
410	43	387	396	386	889	0.88	0.00	0.00	0.12	0.00	0.01	0.99
413	42	197	367	197	385	0.03	0.10	0.00	0.85	0.02	0.95	0.98
413	45	373	406	374	508	0.32	0.00	0.00	0.68	0.00	0.99	0.99
414	45	194	440	195	453	0.03	0.14	0.00	0.83	0.00	0.96	0.99
416	45	394	397	393	1975	0.90	0.00	0.00	0.10	0.00	0.99	0.99
417	46	333	350	335	573	0.65	0.00	0.00	0.35	0.00	0.96	0.98
418	39	206	209	202	1779	0.09	0.05	0.28	0.59	0.00	0.47	0.95
546	46	292	310	292	520	0.02	0.28	0.24	0.44	0.01	0.98	0.98
547	46	346	374	346	500	0.12	0.49	0.00	0.22	0.16	0.93	0.98
550	40	225	235	225	760	0.02	0.28	0.24	0.46	0.00	0.98	0.96
551	43	351	366	351	621	0.07	0.38	0.21	0.35	0.00	0.98	0.99
552	41	249	275	252	420	0.02	0.20	0.21	0.44	0.13	0.98	0.97
552	42	332	337	331	1496	0.05	0.47	0.35	0.13	0.00	0.99	0.98
552	43	346	350	344	1501	0.08	0.27	0.52	0.13	0.00	0.97	0.98
552	43	385	397	385	731	0.36	0.00	0.00	0.64	0.00	0.97	0.99
554	44	439	445	439	1007	0.21	0.00	0.00	0.79	0.00	0.99	0.99
555	47	279	287	280	933	0.04	0.54	0.38	0.04	0.00	0.97	0.97
553	147	169	444	168	455	0.31	0.12	0.00	0.27	0.30	0.07	0.93
554	151	195	207	191	1969	0.09	0.35	0.43	0.12	0.00	0.88	0.68
546	154	210	213	200	434	0.07	0.40	0.34	0.05	0.14	0.86	0.70

Table 1. Properties of the 27 selected pMSSM models. The table contains the masses of the stop, of neutralinos and of the charginos, the branching ratios of the stop decays, the \tilde{t}_L content of the \tilde{t}_1 ($[T_{11}]^2$, with T being the stop mixing matrix) and the bino content of the $\tilde{\chi}_1^0$ ($[N_{11}]^2$, with N being the neutralino mixing matrix).

associated tracks is chosen. Relevant quantities such as the track impact parameters are calculated with respect to the selected primary vertex.

Jets are reconstructed from three-dimensional noise-suppressed calorimeter energy clusters [101] using the anti- k_t jet clustering algorithm [102, 103] with a radius parameter (R) of 0.4. The impact of pileup is statistically subtracted based on the jet area method [104]. To calibrate the reconstructed energy, jets are corrected for the effects of calorimeter response and inhomogeneities using energy- and η -dependent calibration factors based on simulation and validated with extensive test-beam and collision-data studies. In the simulation, this procedure calibrates the jet energies to those of the corresponding jets constructed from stable simulated particles (particle-level jets). In-situ measurements are used to further correct the data to match the energy scale in simulated events [105, 106].

Events containing jets that are likely to have arisen from detector noise, cosmic-ray muons, or machine-induced backgrounds such as beam-gas interactions and beam-halo particles, are removed [106]. Only jets with $p_T > 20$ GeV are considered. After the overlap removal procedure (described below), jets are required to have $|\eta| < 2.5$.

A second collection of anti- k_t jets reconstructed with $R = 1.0$ is used to collect collimated decay products of high- p_T top quarks and W bosons; these jets are referred to as large- R jets [107]. The energy calibration is based on the same strategy as used for the jets with $R = 0.4$ [107]. Jet trimming [108] – a procedure to remove contributions from pileup and from the underlying event by discarding softer components of the jet – is applied with a k_t sub-jet size $R_{\text{sub}} = 0.3$ and a transverse momentum of the sub-jet relative to the large- R jet, f_{cut} , greater than 0.05. Large- R jets are required to have $p_T > 150$ GeV and $|\eta| < 2.0$. The invariant mass of large- R jets is obtained from the energy and momentum of the jet constituents (themselves treated as massless) after the trimming procedure. In addition to the energy calibration, a mass calibration is applied to both data and simulation that accounts for differences between the jet masses derived at particle- and reconstruction-level. Large- R jets may overlap with other physics objects such as jets or leptons; no overlap removal procedure between large- R jets and other objects is applied. Consequently, large- R jets are neither an input to the calculation of the missing transverse momentum, nor considered for the identification of b -jets.

The identification of b -jets uses the ‘MV1’ b -tagging algorithm (defined in refs. [109, 110]), which is based on a neural network and exploits both impact parameter and secondary vertex information. It is trained to assign high weights to b -jets and low weights to jets originating from light-flavour quarks or gluons. Three working points are chosen to maximise the search sensitivity for the various selections. They correspond to an average b -tagging efficiency of 60%, 70% and 80% for b -jets with $p_T > 20$ GeV and $|\eta| < 2.5$ in simulated $t\bar{t}$ events. For these three working points, the average rejection factors for light-quark or gluon jets are approximately 600, 140, and 25 in the same simulated $t\bar{t}$ events [111], respectively. In the simulated samples, the efficiency of identifying b -jets and the probability for mis-identifying (mis-tagging) jets from light-flavour quarks, gluons and charm quarks are corrected to match those found in data.

Electron candidates are reconstructed from energy clusters in the electromagnetic calorimeter matched to a track measured in the inner detector [112, 113]. They are required to have $p_T > 10$ GeV, $|\eta| < 2.47$, and to satisfy the ‘loose’ shower shape and track selection criteria (defined in ref. [114]). The energy is corrected in data to match simulation, while the reconstruction efficiency is scaled in simulated samples to match that observed in data. Muons are reconstructed and identified either as a combined track in the muon spectrometer and inner detector systems, or as an inner detector track matched with a muon spectrometer segment [115–117]. Candidate muons are required to have $p_T > 10$ GeV and $|\eta| < 2.4$. Corrections are applied to the momentum and to the reconstruction efficiency in simulation to match the data. For the soft-lepton selections, the thresholds are lowered to $p_T > 7$ GeV (electrons) and $p_T > 6$ GeV (muons), and electron candidates are required to satisfy the ‘medium’ identification criteria (defined in ref. [114]).

Potential ambiguities between overlapping candidate objects are resolved based on

their angular separation. If an electron candidate and a non-*b*-tagged jet (using the 70% efficiency *b*-tagging working point) overlap within $\Delta R < 0.2$ of each other, then the object is considered to be an electron and the jet is dropped. If an electron candidate and any jet overlap within $0.2 < \Delta R < 0.4$ of each other, or if an electron candidate and a *b*-tagged jet overlap within $\Delta R < 0.2$ of each other, then the electron is dropped and the jet is retained. If a muon candidate and any jet overlap within $\Delta R < 0.4$ of each other, then the muon is not considered and the jet is kept. For the analysis exploiting a large-*R*-jet, the last requirement is changed to $\Delta R < 0.1$, still between the muon and the $R = 0.4$ jets, to recover efficiency losses in boosted topologies. The remaining leptons are referred to as ‘baseline’ leptons, and are used to veto events with more than one lepton.

Photons are not used in the main selections in this analysis, but they are used to select events for one validation sample. Photon candidates must satisfy the ‘tight’ quality criteria with $p_T > 20$ GeV and $|\eta| < 2.47$ [118, 119]. For the validation sample selection only, jets close to a photon, with $\Delta R < 0.2$, are dropped.

An event-veto based on identifying hadronically decaying τ leptons (τ_{had}) is used in some selections to reject $t\bar{t}$ background. The τ_{had} candidates are reconstructed in the same way as jets with $p_T > 15$ GeV and $|\eta| < 2.47$, but calibrated separately to account for a different calorimeter response. The τ -identification is performed with a boosted decision tree (BDT) discriminator [120, 121], which combines tracking information and the transverse and longitudinal shapes of the energy deposits in the calorimeter. If a τ_{had} candidate overlaps with any baseline lepton within $\Delta R < 0.2$, the τ_{had} is not counted.

The missing transverse momentum vector \vec{p}_T^{miss} is the negative vector sum of the p_T of reconstructed objects in the event: jets with $p_T > 20$ GeV, charged lepton (electron and muon) and photon candidates with $p_T > 10$ GeV, and calibrated calorimeter clusters not assigned to these physics objects [122, 123].

The lepton identification criteria are tightened for the selection of the primary electron or muon in the event. The lepton p_T is required to be above 25 GeV, except for the soft-lepton selections where the baseline thresholds of 7 GeV (electron) or 6 GeV (muon) are kept. Electrons are required to satisfy the ‘tight’ selection criteria (defined in ref. [114]), and are required to satisfy a track-isolation criterion. The scalar sum of the p_T of tracks associated with the primary vertex and found within a cone of radius $\Delta R = 0.2$ around the electron (excluding the electron itself) is required to be less than 10% of the electron p_T . Similarly, a muon isolation criterion is imposed: the track isolation is required to be less than 1.8 GeV in a cone of radius $\Delta R = 0.2$. A less stringent muon isolation criterion is used for the analysis using a large-*R* jet: the track isolation is required to be less than 12% of the muon p_T . This helps to recover signal efficiency losses in boosted topologies. For the analyses based on a soft lepton, the ‘tight’ electron selection is omitted (keeping the ‘medium’ criteria from the baseline selection), and a modified version of the track-isolation is applied to electrons and muons: the scalar sum of the p_T of tracks within a cone of radius $\Delta R = 0.3$ around the lepton (excluding the lepton itself) is required to be less than 16% (12%) of the electron (muon) p_T . Furthermore, the impact parameters along the beam direction (z_0) and in the transverse plane (d_0) are used to impose additional soft-lepton requirements: $|z_0 \sin \theta| < 0.4(0.4)$ mm and $|d_0/\sigma_{d_0}| < 5(3)$ for electrons (muons), where σ_{d_0}

is the uncertainty on d_0 . The modified criteria of the soft-lepton selection are specifically optimised to suppress low- p_T jets mis-identified as isolated leptons.

6.2 Tools to discriminate signal from background

Requiring one isolated lepton (ℓ), several jets, and E_T^{miss} selects a sample enriched in semi-leptonic $t\bar{t}$ and $W+\text{jets}$ events. Both backgrounds are reduced by requiring the transverse mass (m_T) to be above the W boson mass, where m_T is defined by

$$m_T = \sqrt{2 \cdot p_T^\ell \cdot E_T^{\text{miss}} (1 - \cos \Delta\phi(\vec{\ell}, \vec{p}_T^{\text{miss}}))}.$$

Here p_T^ℓ is the lepton p_T , and $\Delta\phi(\vec{\ell}, \vec{p}_T^{\text{miss}})$ is the azimuthal angle between the lepton and the \vec{p}_T^{miss} directions.⁸ The dominant background after this requirement stems from dileptonic $t\bar{t}$ events, where one lepton is not identified, or is outside the detector acceptance, or is a hadronically decaying τ lepton. In all of these cases, the $t\bar{t}$ decay products include two or more high- p_T neutrinos, resulting in large E_T^{miss} and large m_T values. Requiring one or more b -tagged jets further removes $W+\text{jets}$ events, while a b -tag veto reduces the $t\bar{t}$ background but also the stop signal in most models. All but one SR require at least one or two b -tagged jets.

A number of variables and tools have been developed specifically to suppress the different types of dileptonic $t\bar{t}$ events. The detailed definitions of the variables are provided in appendix A.

- am_{T2} and m_{T2}^τ are two variants of the variable m_{T2} [124], which is a generalisation of the transverse mass applied to signatures with two particles that are not directly detected. Figure 3 illustrates the $t\bar{t}$ event topologies targeted by the two variables.

The first variant is a form of asymmetric m_{T2} (am_{T2}) [125–127] in which the undetected particle is the W boson for the branch with the lost lepton and the neutrino is the missing particle for the branch with the observed charged lepton. For dileptonic $t\bar{t}$ events with a lost lepton, am_{T2} is bounded from above by the top quark mass, whereas new physics can exceed this bound.

The second m_{T2} variant (m_{T2}^τ) is designed for events with a hadronically decaying τ lepton by using the ‘ τ -jet’ as a visible particle for one branch and the observed lepton for the other branch. For $t\bar{t}$ events where one W boson decays leptonically and the other to a τ_{had} , the endpoint is the W boson mass in the limit of collinear neutrinos.

- *topness* is a variable designed to identify and suppress partially reconstructed dileptonic $t\bar{t}$ events, as proposed in ref. [128]. The *topness* variable is based on minimising a χ^2 -type function indicating the similarity of the event to dileptonic $t\bar{t}$ events. Similar to the am_{T2} variable, one lepton is assumed to be lost.
- A hadronic top mass, $m_{\text{had-top}}$, is designed to reject dileptonic $t\bar{t}$ events while retaining signal events that contain a hadronically decaying on-shell top quark, as in the $\tilde{t}_1 \rightarrow t\tilde{\chi}_1^0$

⁸This formula of m_T makes the assumption that the lepton mass is negligible.

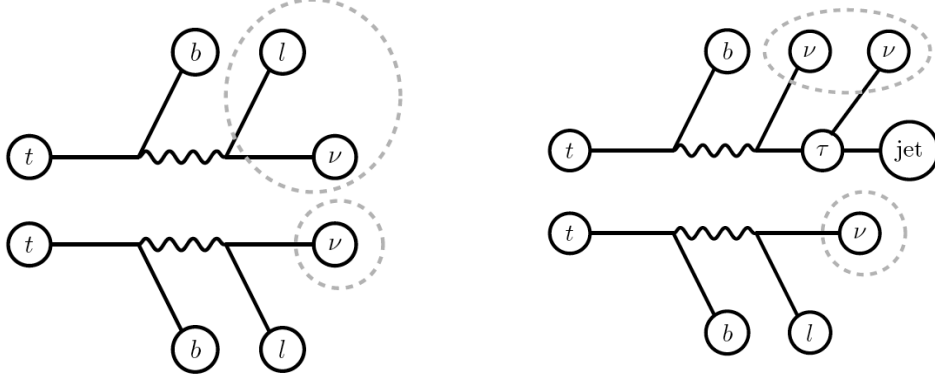


Figure 3. Illustration of the construction of the am_{T2} (left) and m_{T2}^{τ} (right) variables, which are used to discriminate against dileptonic $t\bar{t}$ background with one lost lepton (left) or with a hadronically decaying τ (right). The dashed lines indicate the objects that are assumed to be undetected ('lost') for the purpose of defining the two variables.

decay mode. The $m_{\text{had-top}}$ variable is a three-jet invariant mass, where the jets are selected by minimising a χ^2 -distribution taking into account the jet momenta and energy resolutions [105, 129].

- Dedicated τ -identification criteria are used to reject $t\bar{t}$ events which contain a hadronic τ decay. For the construction of the τ -veto, the reconstructed τ_{had} candidates, as previously defined, are subject to further selection requirements (described in appendix A). Three τ -veto working points are defined: loose, tight, and extra-tight.
- A track-veto is designed to reject events which contain an isolated track not associated with a baseline lepton. This complements the second-lepton veto, and helps to reject $t\bar{t}$ events with a one-prong τ_{had} . The selection criteria are detailed in appendix A.

Multijet events can pass the event selection if a jet is mis-identified as a lepton or when a real lepton from a heavy-flavour decay satisfies the isolation criteria, and if large $E_{\text{T}}^{\text{miss}}$ occurs due to mis-measured jets. The former is suppressed by the lepton isolation criteria, while the following variables are used to reduce the latter effect.

- $\Delta\phi(\text{jet}_i, \vec{p}_{\text{T}}^{\text{miss}})$, the azimuthal opening angle between jet i and $\vec{p}_{\text{T}}^{\text{miss}}$, is used to suppress multijet events where $\vec{p}_{\text{T}}^{\text{miss}}$ is aligned with a jet.
- $E_{\text{T}}^{\text{miss}}/\sqrt{H_{\text{T}}}$, where H_{T} is defined as the scalar p_{T} sum of the four leading jets, is an approximation of the $E_{\text{T}}^{\text{miss}}$ significance.
- $E_{\text{T}}^{\text{miss}}/m_{\text{eff}}$, where $m_{\text{eff}} = H_{\text{T}} + p_{\ell}^{\ell} + E_{\text{T}}^{\text{miss}}$.
- $H_{\text{T},\text{sig}}^{\text{miss}}$ is an object-based missing transverse momentum, divided by the per-event resolution of the jets. The object-based missing transverse momentum is the negative sum of the jets and lepton vectors. A detailed description is given in appendix A.

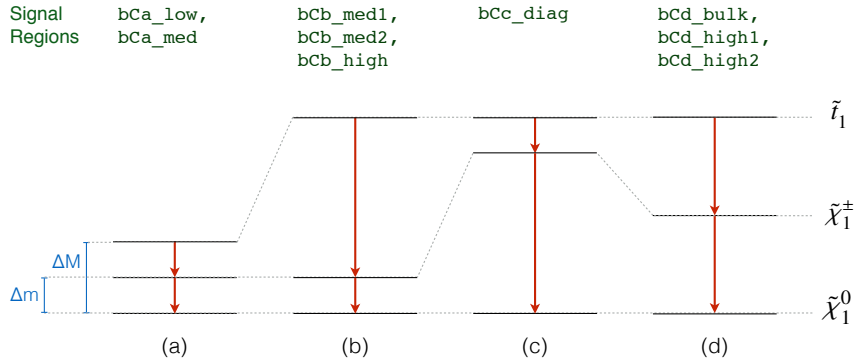


Figure 4. Schematic diagram of the mass hierarchies for the $\tilde{t}_1 \rightarrow b\tilde{\chi}_1^\pm$ decay mode, with a subsequent $\tilde{\chi}_1^\pm \rightarrow W^{(*)}\tilde{\chi}_1^0$ decay. A list of the corresponding signal regions is given above the diagram.

7 Signal selections

Signal selections are optimised using simulated samples only. The metric of the optimisation is to maximise the exclusion sensitivity for the various decay modes, and for different regions of SUSY simplified model parameter space. A set of signal benchmark models, selected to cover the various stop scenarios, was used for the optimisation considering all studied discriminating variables and including statistical and systematic uncertainties. The shape-fits employ multiple bins in one or two discriminating variables, which were selected considering the signal and background separation potential, inter-variable correlations, systematic uncertainties, and modelling of the data.

Table 2 summarises all 15 SRs with a brief description of the targeted signal scenarios, the exclusion analysis techniques, and forward references to the tables which list the event selection details. Four SRs target the $\tilde{t}_1 \rightarrow t\tilde{\chi}_1^0$ decay. The corresponding SR labels begin with tN, which is an acronym for ‘top neutralino’; additional text in the label describes the stop mass region, for example tN_diag targets the ‘diagonal’ of the $\tilde{t}_1-\tilde{\chi}_1^0$ mass plane. Nine SRs target the $\tilde{t}_1 \rightarrow b\tilde{\chi}_1^\pm$ decay, where the SR labels follow the same logic: the first two characters bC stand for ‘bottom chargino’, a third letter (‘a’ to ‘d’) denotes the four different mass hierarchies illustrated in figure 4, and the last piece of text describes the stop mass region. Furthermore, two SRs labelled 3body and tNbC_mix are dedicated to the three-body decay mode ($\tilde{t}_1 \rightarrow bW\tilde{\chi}_1^0$), and the mixed scenario where $\tilde{t}_1 \rightarrow t\tilde{\chi}_1^0$ and $\tilde{t}_1 \rightarrow b\tilde{\chi}_1^\pm$ decays both occur, respectively. The SRs are not mutually exclusive.

All SRs employ selection requirements to suppress the multijet background, and most SRs use the tools described in section 6.2 to reduce the dileptonic $t\bar{t}$ background. Shape-fit techniques are employed to derive model-dependent exclusion limits where useful, while for all model-independent results a simple cut-and-count approach is used. This procedure implies that for SRs using shape-fits one bin is probed at a time to extract the model-independent results. Only a single bin, or the four bins with highest signal-to-background ratio are included; these are referred to as signal-sensitive bins. The model-dependent

SR	Signal scenario	Exclusion technique	Table
<code>tN_diag</code>	$\tilde{t}_1 \rightarrow t\tilde{\chi}_1^0$, $m_{\tilde{t}_1} \gtrsim m_t + m_{\tilde{\chi}_1^0}$	shape-fit (E_T^{miss} and m_T)	4
<code>tN_med</code>	$\tilde{t}_1 \rightarrow t\tilde{\chi}_1^0$, $m_{\tilde{t}_1} \sim 550 \text{ GeV}$, $m_{\tilde{\chi}_1^0} \lesssim 225 \text{ GeV}$	cut-and-count	4
<code>tN_high</code>	$\tilde{t}_1 \rightarrow t\tilde{\chi}_1^0$, $m_{\tilde{t}_1} \gtrsim 600 \text{ GeV}$	cut-and-count	4
<code>tN_boost</code>	$\tilde{t}_1 \rightarrow t\tilde{\chi}_1^0$, $m_{\tilde{t}_1} \gtrsim 600 \text{ GeV}$, with a large- R jet	cut-and-count	4
<code>bCa_low</code>	$\tilde{t}_1 \rightarrow b\tilde{\chi}_1^\pm$, $\Delta M \lesssim 50 \text{ GeV}$ $\tilde{t}_1 \rightarrow bff'\tilde{\chi}_1^0$	shape-fit (lepton p_T)	5
<code>bCa_med</code>	$\tilde{t}_1 \rightarrow b\tilde{\chi}_1^\pm$, $50 \text{ GeV} \lesssim \Delta M \lesssim 80 \text{ GeV}$ $\tilde{t}_1 \rightarrow bff'\tilde{\chi}_1^0$	shape-fit (lepton p_T)	5
<code>bCb_med1</code>	$\tilde{t}_1 \rightarrow b\tilde{\chi}_1^\pm$, $\Delta m \lesssim 25 \text{ GeV}$, $m_{\tilde{t}_1} \lesssim 500 \text{ GeV}$	shape-fit (am_{T2})	5
<code>bCb_high</code>	$\tilde{t}_1 \rightarrow b\tilde{\chi}_1^\pm$, $\Delta m \lesssim 25 \text{ GeV}$, $m_{\tilde{t}_1} \gtrsim 500 \text{ GeV}$	shape-fit (am_{T2})	5
<code>bCb_med2</code>	$\tilde{t}_1 \rightarrow b\tilde{\chi}_1^\pm$, $\Delta m \lesssim 80 \text{ GeV}$, $m_{\tilde{t}_1} \lesssim 500 \text{ GeV}$	shape-fit (am_{T2} and m_T)	6
<code>bCc_diag</code>	$\tilde{t}_1 \rightarrow b\tilde{\chi}_1^\pm$, $m_{\tilde{t}_1} \gtrsim m_{\tilde{\chi}_1^\pm}$	cut-and-count	6
<code>bCd_bulk</code>	$\tilde{t}_1 \rightarrow b\tilde{\chi}_1^\pm$, $(\Delta M, \Delta m) \gtrsim 100 \text{ GeV}$, $m_{\tilde{t}_1} \lesssim 500 \text{ GeV}$	shape-fit (am_{T2} and m_T)	6
<code>bCd_high1</code>	$\tilde{t}_1 \rightarrow b\tilde{\chi}_1^\pm$, $(\Delta M, \Delta m) \gtrsim 100 \text{ GeV}$, $m_{\tilde{t}_1} \gtrsim 500 \text{ GeV}$	cut-and-count	6
<code>bCd_high2</code>	$\tilde{t}_1 \rightarrow b\tilde{\chi}_1^\pm$, $\Delta M \gtrsim 250 \text{ GeV}$, $m_{\tilde{t}_1} \gtrsim 500 \text{ GeV}$	cut-and-count	6
<code>3body</code>	$\tilde{t}_1 \rightarrow bW\tilde{\chi}_1^0$, $m_{\tilde{t}_1} \lesssim 300 \text{ GeV}$	shape-fit (am_{T2} and m_T)	7
<code>tNbC_mix</code>	non-symmetric ($\tilde{t}_1 \rightarrow t\tilde{\chi}_1^0$, $\tilde{t}_1 \rightarrow b\tilde{\chi}_1^\pm$)	cut-and-count	7

Table 2. Overview of all signal regions (SRs) together with the targeted signal scenario, the analysis technique used for model-dependent exclusions, and a reference to the table with the event selection details. For the $\tilde{t}_1 \rightarrow b\tilde{\chi}_1^\pm$ decay mode, the mass splittings $\Delta M = m(\tilde{t}_1) - m(\tilde{\chi}_1^0)$ and $\Delta m = m(\tilde{\chi}_1^\pm) - m(\tilde{\chi}_1^0)$ are used to characterise the mass hierarchies, as illustrated in figure 4. The SRs `bCa_low`, `bCa_med`, `bCb_med1` and `bCb_high` employ selections based on a soft lepton.

and model-independent selections are defined in this section, and the corresponding fit configurations are described in section 10.

7.1 Event preselection

Common preselection criteria are employed as follows. Events are required to contain a reconstructed primary vertex. Furthermore, a set of quality requirements to avoid badly reconstructed jets, mismeasured- E_T^{miss} and detector-related problems is imposed on all events. Events with a bad quality muon or with a cosmic-ray muon candidate⁹ are rejected.

⁹ Defined as a muon candidate with a transverse or longitudinal impact parameter of $|d_0| > 0.2 \text{ mm}$ or $|z_0| > 1 \text{ mm}$.

Preselection	Description
Trigger	logical-OR combination of single-lepton and E_T^{miss} triggers; soft lepton: E_T^{miss} trigger only.
Data quality	jet and E_T^{miss} cleaning, cosmic-ray muon veto, primary vertex.
Lepton	one isolated electron or muon with $p_T > 25 \text{ GeV}$; soft lepton: the p_T threshold is $6(7) \text{ GeV}$ for muons (electrons).
2nd-lepton veto	No additional baseline lepton with $p_T > 10 \text{ GeV}$; soft lepton: no further baseline soft muon (electron) with $p_T > 6(7) \text{ GeV}$.
Jets	The minimum jet multiplicity requirement varies between 2 and 4.
E_T^{miss}	$E_T^{\text{miss}} > 100 \text{ GeV}$ or tighter is required in all selections.

Table 3. Preselection criteria common to all signal selections.

Exactly one isolated lepton is required with $p_T > 25 \text{ GeV}$ except for the soft-lepton selections which employ a $p_T > 6(7) \text{ GeV}$ requirement for muons (electrons). The common lepton isolation criteria are tightened for the soft-lepton selections while they are relaxed for the analysis exploiting a large- R jet (cf. section 6). Events containing additional baseline leptons are rejected. A minimum number of jets ranging between 2 and 4, and $E_T^{\text{miss}} > 100 \text{ GeV}$ are common requirements amongst all analyses. Table 3 summarises the preselection criteria.

Figure 5 illustrates the separation power for a selection of discriminating variables. For these distributions, events are required to pass the preselection (table 3), to have at least four jets with $p_T > 25 \text{ GeV}$, one of which above 60 GeV , and with at least one of them b -tagged using the 70% working point, and to have $E_T^{\text{miss}} > 100 \text{ GeV}$, $m_T > 60 \text{ GeV}$ and $E_T^{\text{miss}}/\sqrt{H_T} > 5 \text{ GeV}^{1/2}$. The $W+\text{jets}$ background is normalised to match data in a sample selected in the same way, except that a b -veto is imposed. The other processes are normalised to their theoretical cross-sections. Data and background estimation are seen to be in good agreement.

7.2 Selections for the $\tilde{t}_1 \rightarrow t\tilde{\chi}_1^0$ decay

Stop pair production with subsequent $\tilde{t}_1 \rightarrow t\tilde{\chi}_1^0$ decays leads to final state objects similar to that of $t\bar{t}$ production augmented by two $\tilde{\chi}_1^0$. Four SRs, labelled `tN_diag`, `tN_med`, `tN_high`, and `tN_boost`, target different regions in the $\tilde{t}_1 - \tilde{\chi}_1^0$ mass plane and implement different analysis strategies. Table 4 details the event selections for these SRs. Criteria based on a subset of the variables outlined in section 6.2, as well as optimised jet thresholds, a more stringent E_T^{miss} requirement, and a requirement on the angular separation between the highest- p_T b -tagged jet and the lepton, $\Delta R(b\text{-jet}, \ell)$, are used to suppress $t\bar{t}$ and $W+\text{jets}$ backgrounds as well as to reduce the multijet background to a negligible level.

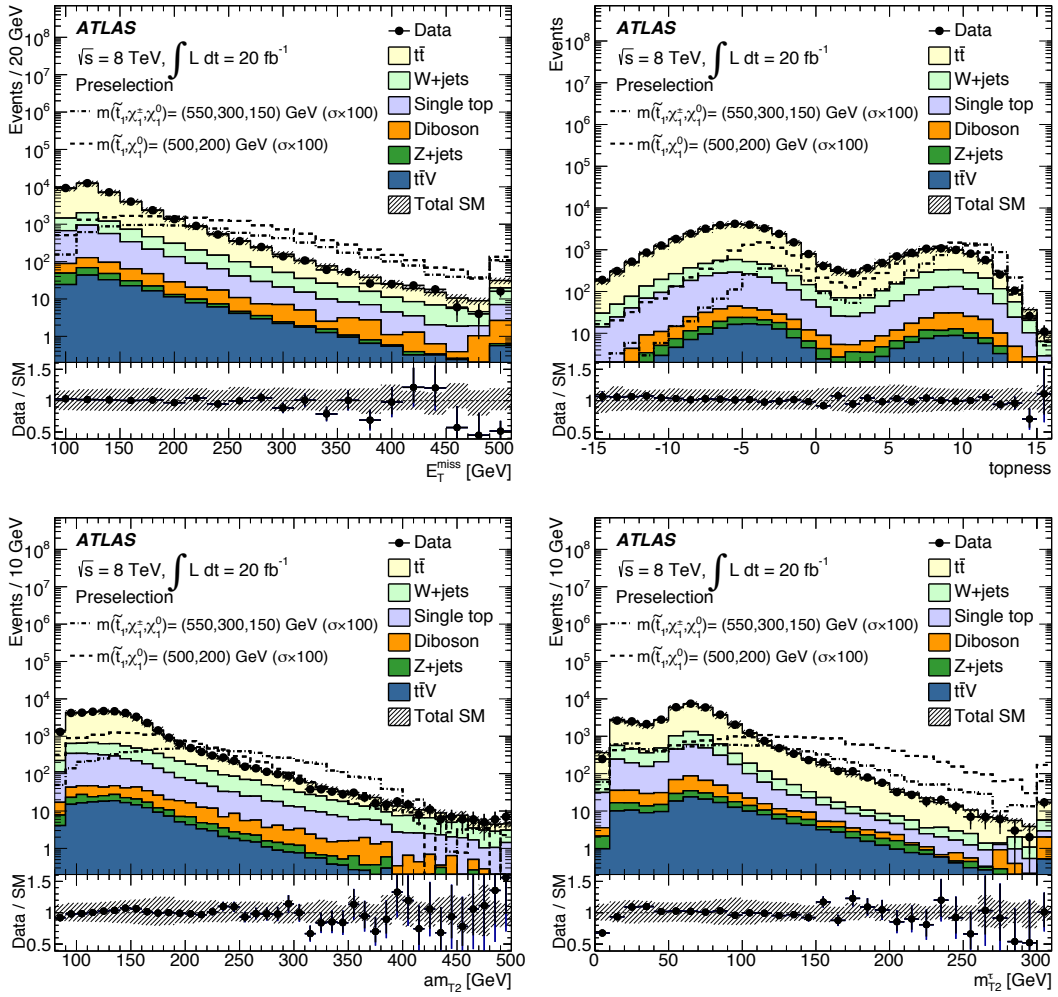


Figure 5. Comparison of data with estimated backgrounds in the E_T^{miss} (top left), topness (top right), am_{T_2} (bottom left), and $m_{T_2}^{\tau}$ (bottom right) distributions for the preselection defined in the text. The uncertainty band includes statistical and all experimental systematic uncertainties. The last bin includes overflows. Benchmark signal models with cross-sections enhanced by a factor of 100 are overlaid for comparison.

The loosest selection, `tN_diag`, employs a multi-binned shape-fit that targets the challenging parameter space where the stop and its decay products are nearly mass degenerate ($m_{\tilde{t}_1} \gtrsim m_t + m_{\tilde{\chi}_1^0}$), also referred to as the ‘diagonal’. The strategy of exploiting binned shape information significantly improves the sensitivity. The two-dimensional shape-fit in the variables m_T and E_T^{miss} is illustrated in figure 6 (left plot). The top 12 bins serve both to probe a signal and to normalise the $t\bar{t}$ background; a subset of the 12 bins has a high purity in $t\bar{t}$ events. Three additional bins with a b -tag veto, shown in the bottom part, are used to derive the normalisation of the $W+\text{jets}$ background. The bins with $E_T^{\text{miss}} > 150$ GeV

	tN_diag	tN_med	tN_high	tN_boost
Preselection	Default preselection criteria, cf. table 3.			
Lepton	$= 1$ lepton			
Jets	≥ 4 with $p_T >$ 60, 60, 40, 25 GeV	≥ 4 with $p_T >$ 80, 60, 40, 25 GeV	≥ 4 with $p_T >$ 100, 80, 40, 25 GeV	≥ 4 with $p_T >$ 75, 65, 40, 25 GeV
b-tagging	≥ 1 b-tag (70% eff.) amongst four selected jets			
large-R jet	–			≥ 1 , $p_T > 270$ GeV and $m > 75$ GeV
$\Delta\phi(\text{jet}_2^{\text{large-}R}, \vec{p}_T^{\text{miss}})$	–			> 0.85
E_T^{miss}	> 100 GeV	> 200 GeV	> 320 GeV	> 315 GeV
m_T	> 60 GeV	> 140 GeV	> 200 GeV	> 175 GeV
am_{T2}	–	> 170 GeV	> 170 GeV	> 145 GeV
m_{T2}^{τ}	–	–	> 120 GeV	–
<i>topness</i>	–	–	–	> 7
$m_{\text{had-top}}$	$\in [130, 205]$ GeV	$\in [130, 195]$ GeV	$\in [130, 250]$ GeV	
τ-veto	tight	–	–	modified, see text.
$\Delta R(b\text{-jet}, \ell)$	< 2.5	–	< 3	< 2.6
$E_T^{\text{miss}}/\sqrt{H_T}$	> 5 GeV $^{1/2}$	–		
$H_{T,\text{sig}}^{\text{miss}}$	–	> 12.5		> 10
$\Delta\phi(\text{jet}_i, \vec{p}_T^{\text{miss}})$	> 0.8 ($i = 1, 2$)	> 0.8 ($i = 2$)	–	$> 0.5, 0.3$ ($i = 1, 2$)
Model-dependent selection:				
	shape-fit in m_T and E_T^{miss} , cf. figure 6.	cut-and-count		
Model-independent selection:				
	test 4 most signal-sensitive bins one-by-one.	cut-and-count		

Table 4. Selection criteria for SRs employed to search for $\tilde{t}_1 \rightarrow t\tilde{\chi}_1^0$ decays.

or $m_T > 140$ GeV are defined without upper boundaries.

The two SRs `tN_med` and `tN_high` target medium and high stop mass regions, respec-

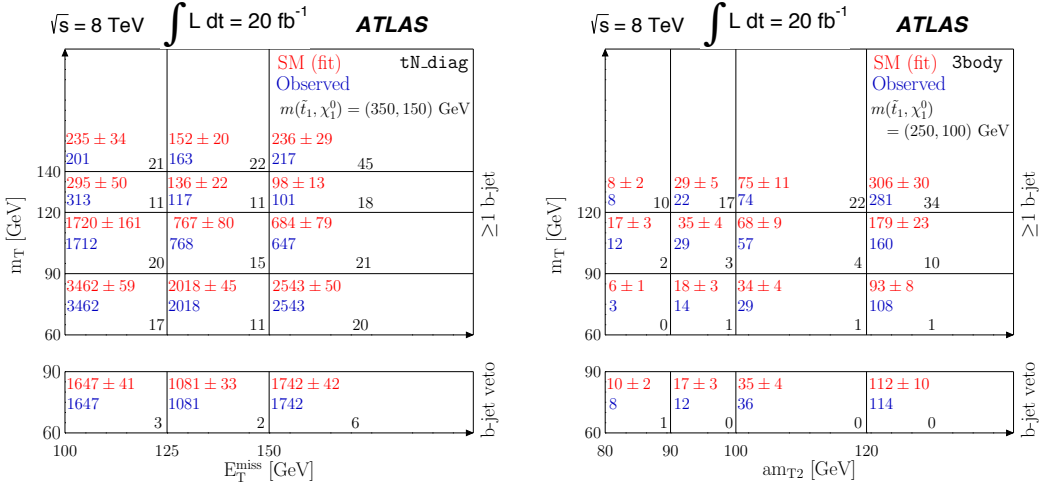


Figure 6. Schematic illustration of the **tN_diag** (left) and **3body** (right) shape-fit binning. The m_T and E_T^{miss} (left) or am_{T2} (right) variables are used to define a matrix of 4×3 bins (left) or 3×4 (right) in the top part, which is sensitive to stop models, while also being enriched with $t\bar{t}$ background. The bottom bins invert the b -tag requirement into a veto, and serve to normalise the $W + \text{jets}$ background. The numbers of observed events together with the estimated background, obtained using the background-only fit described in section 8, are given for each bin. The data and estimated background are in perfect agreement in the six bottom bins for the left plot because the fit is configured to use these six bins together with six free parameters; the fit used for the right plot employs the bottom eight bins and two free parameters. For comparison the expected numbers of events for one signal model are shown.

tively. Both SRs are based on a cut-and-count approach with relatively tight selections. The SR labelled **tN_boost** also targets models with a high stop mass and a nearly massless LSP, but takes advantage of the ‘boosted’ topology. The selection assumes that either all decay products of the hadronically decaying top quark, or at least the decay products of the hadronically decaying W boson, collimate into a jet with a radius of $\lesssim 1.0$. Figure 7 shows some of the relevant large- R jet related distributions. The overlaid heavy stop benchmark model illustrates the separation power of the variables. The **tN_boost** selection requires at least one large- R jet with $p_T > 270$ GeV and an invariant mass above 75 GeV. To further discriminate stop decays from the $t\bar{t}$ background, events with a second (ordered by p_T) large- R jet are required to have a minimum azimuthal distance between \vec{p}_T^{miss} and the second large- R jet, $\Delta\phi(\text{jet}_2^{\text{large-}R}, \vec{p}_T^{\text{miss}})$. The extra-tight τ -veto is applied to discard events with τ_{had} candidates well separated from large- R jets, $\Delta R(\tau_{\text{had}}, \text{large-}R\text{-jet}) > 2.6$, that satisfy the above p_T and mass requirements.

7.3 Selections for the $\tilde{t}_1 \rightarrow b\tilde{\chi}_1^\pm$ decay

Nine SRs target scenarios where both stops decay as $\tilde{t}_1 \rightarrow b\tilde{\chi}_1^\pm$ followed by subsequent $\tilde{\chi}_1^\pm \rightarrow W^{(*)}\tilde{\chi}_1^0$ decays. The mass of the lightest chargino $m(\tilde{\chi}_1^\pm)$ relative to the \tilde{t}_1 and $\tilde{\chi}_1^0$ masses largely defines the kinematic properties. Figure 4 schematically illustrates the four

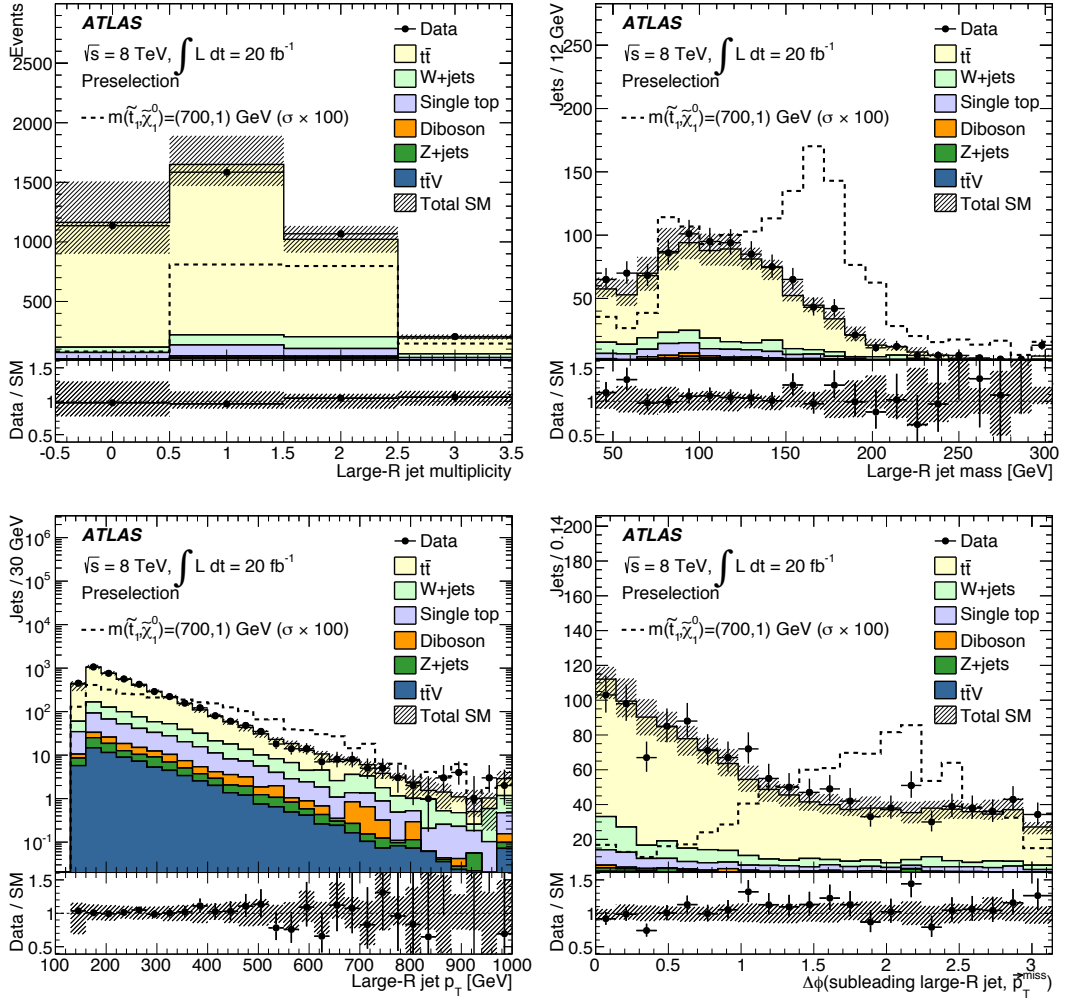


Figure 7. Comparison of data with background expectations of large- R jet distributions: multiplicity (top left), invariant mass (top right), transverse momentum (bottom left), and distance in ϕ space between the second-highest- p_T large- R jet and \vec{p}_T^{miss} . Events are required to pass the preselection defined in section 7.1. In addition, the jet thresholds are tightened ($p_T > 75, 65, 40, 25 \text{ GeV}$) and a requirement of $m_T > 120 \text{ GeV}$ is imposed. The uncertainty band includes statistical and all experimental systematic uncertainties. The last bin includes overflows. A benchmark signal model, with cross-section enhanced by a factor of 100, is overlaid for comparison.

distinct mass hierarchies, whose SRs are described below.

Selections for mass hierarchy (a):

The selection of signal events with a small overall mass splitting, $\Delta M = m(\tilde{t}_1) - m(\tilde{\chi}_1^0)$, relies on the presence of an initial-state radiation (ISR) jet, against which the stop decay products recoil. Consequently, events with a hard leading jet are selected together with a soft lepton and relatively soft sub-leading jets. The leading jet must not satisfy the

	<code>bCa_low</code>	<code>bCa_med</code>	<code>bCb_med1</code>	<code>bCb_high</code>
Preselection	soft-lepton preselection, cf. table 3.			
Lepton	$= 1$ soft lepton		$= 1$ soft lepton with $p_T < 25 \text{ GeV}$	
Jets	≥ 2 with $p_T > 180, 25 \text{ GeV}$	≥ 3 with $p_T > 180, 25, 25 \text{ GeV}$	≥ 2 with $p_T > 60, 60 \text{ GeV}$	
$\Delta\phi(jet_i, \vec{p}_T^{\text{miss}})$	–		> 0.4 (i=1,2)	
Jet veto	–		$H_{T,2} < 50 \text{ GeV}$	–
b-tagging	≥ 1 sub-leading jet b -tagged (70% eff.)		Leading two jets b -tagged (60% eff.)	
b-veto	1 st jet not b -tagged (70% eff.)		–	
m_{bb}	–		$> 150 \text{ GeV}$	
E_T^{miss}	$> 370 \text{ GeV}$	$> 300 \text{ GeV}$	$> 150 \text{ GeV}$	$> 250 \text{ GeV}$
$E_T^{\text{miss}}/m_{\text{eff}}$	> 0.35	> 0.3	–	
m_T	$> 90 \text{ GeV}$	$> 100 \text{ GeV}$	–	
Model-dependent selection: shape-fit				
	4 bins in lepton p_T range [6(7), 50] GeV		6 bins in am_{T2} range [0, 500] GeV	
Model-independent selection: 1 bin with				
	lepton $p_T < 25 \text{ GeV}$		$am_{T2} > 170 \text{ GeV}$	$am_{T2} > 200 \text{ GeV}$

Table 5. Selection criteria for soft-lepton SRs, employed to search for $\tilde{t}_1 \rightarrow b\tilde{\chi}_1^\pm$ decays. The two leftmost/rightmost SRs target mass hierarchies (a)/(b), illustrated in figure 4.

b -tagging criteria, while at least one b -tagged jet amongst the sub-leading jets is required.

Two SRs, labelled `bCa_low` and `bCa_med`, are defined to probe scenarios with a mass splitting $\Delta M \lesssim 50 \text{ GeV}$, and $50 \text{ GeV} \lesssim \Delta M \lesssim 80 \text{ GeV}$, respectively. The SR event selections are listed in table 5. The requirement of ≥ 3 jets suppresses the $W + \text{jets}$ background in `bCa_med`. For `bCa_low`, the jet multiplicity requirement is lowered to ≥ 2 to avoid large signal acceptance losses, but tighter E_T^{miss} and $E_T^{\text{miss}}/m_{\text{eff}}$ thresholds are applied to keep the $W + \text{jets}$ and multijet backgrounds suppressed. Figure 8 compares data with estimated backgrounds in the lepton p_T and $E_T^{\text{miss}}/m_{\text{eff}}$ distributions. The overlaid stop benchmark model motivates the selection of low- p_T leptons, and the background estimates show the non-negligible contribution from multijet events (with mis-identified leptons).

Model-dependent exclusion results are obtained using a shape-fit in the lepton p_T variable with four bins of approximately uniform widths in the range [6(7), 50] GeV for muons (electrons). For model-independent results, the cut-and-count approach is used with an additional lepton $p_T < 25 \text{ GeV}$ requirement.

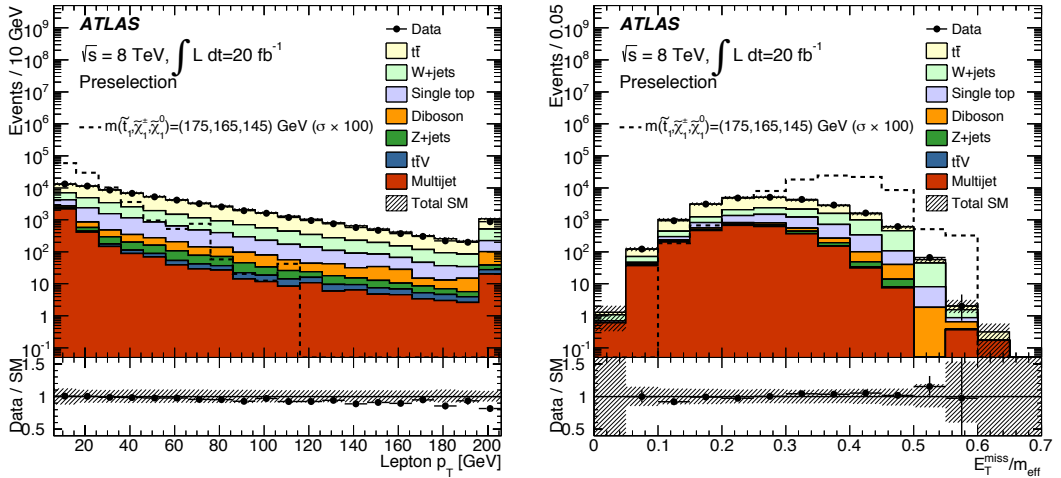


Figure 8. Comparison of data with estimated backgrounds in the lepton p_T (left) and $E_T^{\text{miss}}/m_{\text{eff}}$ (right) distributions. Events are required to satisfy the soft-lepton preselection criteria (cf. table 3), have $m_T > 40 \text{ GeV}$, and contain two or more jets ($p_T > 130, 25 \text{ GeV}$) of which the leading one must not be b -tagged while the sub-leading one is required to be b -tagged. The $t\bar{t}$ and $W+\text{jets}$ backgrounds are normalised using control regions, the multijet background is estimated directly from data, and all other backgrounds are normalised to their theoretical predictions (as described in section 8). The uncertainty band includes statistical and all experimental systematic uncertainties. The last bin includes overflows. A benchmark signal model, with cross-section enhanced by a factor of 100, is overlaid for comparison.

Selections for mass hierarchy (b):

Signal scenarios with a moderately large ΔM but a small $\Delta m = m(\tilde{\chi}_1^\pm) - m(\tilde{\chi}_1^0)$ feature two high- p_T b -jets and low-momentum decay products from the two off-shell W bosons.

Two SRs, labelled `bCb_med1` and `bCb_high`, employ event selections based on the presence of one soft lepton and two b -tagged jets. They target medium and high stop mass regions, respectively. The complete event selections are listed in table 5. The `bCb_med1` SR employs an $E_T^{\text{miss}} > 150 \text{ GeV}$ requirement, the lowest possible to retain full E_T^{miss} trigger efficiency. For models with a heavier \tilde{t}_1 , a higher E_T^{miss} threshold improves the sensitivity. The dominant background stems from $t\bar{t}$ production and is suppressed by vetoing additional hard jet activity. The variable $H_{T,2}$ is defined like H_T but without including the two leading jets. The `bCb_high` SR omits the jet activity veto to compensate for the loss in signal acceptance associated with the more stringent E_T^{miss} requirement. Beyond the kinematic am_{T2} bound, the dominant source of background arises from mis-tagged c -jets in semileptonic $t\bar{t}$ events, and the production of a W boson in association with heavy-flavour jets. To minimise the mis-tagged background, the b -tagging algorithm is operated at the 60% efficiency working point. A minimum requirement on the invariant mass of the two b -tagged jets, m_{bb} , is imposed to reduce the contribution from $W + b\bar{b}$ events.

Exclusion results are obtained using a shape-fit in the am_{T2} variable with six bins

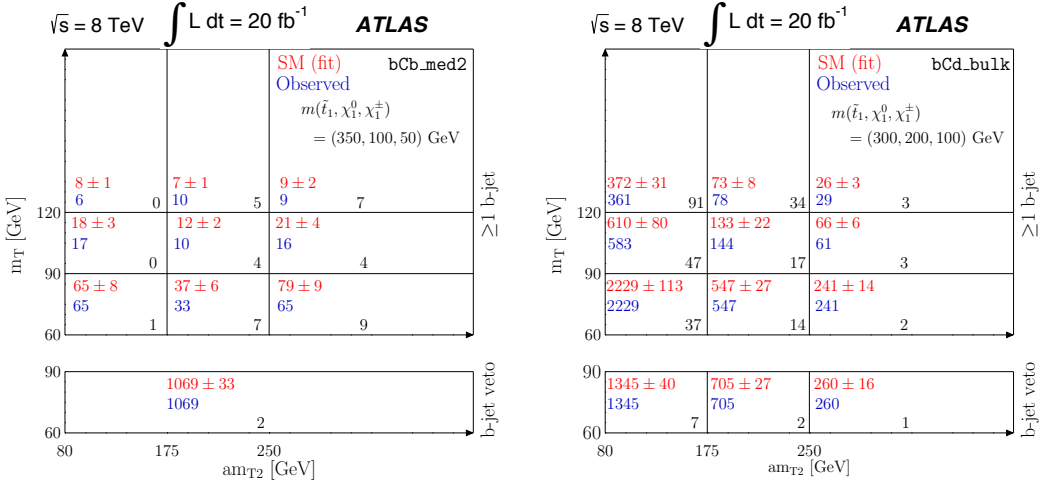


Figure 9. Schematic illustration of the **bCb_med2** (left) and **bCd_bulk** (right) shape-fit binning. More details are given in the caption of figure 6. The data and estimated background are in perfect agreement in the six bottom bins of the right plot because the fit is configured to use these six bins together with six free parameters; the fit used for the left plot employs the bottom four bins and two free parameters.

in the range $[0, 500]$ GeV with a uniform bin width. For all model-independent results, the cut-and-count approach is used but applying an $am_{T2} > 170(200)$ GeV requirement in **bCb_med1** (**bCb_high**).

A third SR, labelled **bCb_med2**, also targets intermediate stop masses. It is based on the default lepton selection ($p_T > 25$ GeV), and requiring at least two high- p_T b -tagged jets to exploit larger $\tilde{t}_1 - \tilde{\chi}_1^\pm$ mass splittings than **bCb_med1**. The full event selection is detailed in the leftmost column in table 6. The analysis employs a two-dimensional shape-fit technique similar to the one used for **tN_diag** but in the m_T and am_{T2} variables. Figure 9 (left plot) illustrates the configuration. The highest signal sensitivity is obtained from bins in the top-right region.

Selections for mass hierarchy (c):

Models with $m_{\tilde{\chi}_1^\pm}$ just below $m_{\tilde{t}_1}$ yield two low-momentum b -jets. The signal selection strategy is based on vetoing events with b -tagged jets, assuming both signal b -jets are below the jet p_T acceptance of the analysis, and therefore suppressing the $t\bar{t}$ background. The sensitivity for low- $m(\tilde{t}_1)$ models is improved by selecting events with ISR-like jet activity. One SR, labelled **bCc_diag**, is employed and defined in table 6. The suffix ‘diag’ refers to the diagonal region of the $m_{\tilde{\chi}_1^\pm} = 2m_{\tilde{\chi}_1^0}$ scenario, the benchmark region used to optimise this SR. The event selection includes one central lepton ($|\eta| < 1.2$) to suppress the $W + \text{jets}$ background, and three or more jets, of which none must satisfy the b -tagging criteria. In signal events, two of the three required jets tend to originate from the hadronic W boson decay, while the highest- p_T jet typically arises from ISR. The b -veto strongly suppresses $t\bar{t}$ events, leaving $W + \text{jets}$ as the dominant background. Requirements on the $\Delta R(j_1, \ell)$ and

	bCb_med2	bCc_diag	bCd_bulk	bCd_high1	bCd_high2
Preselection	Default preselection criteria, cf. table 3.				
Lepton	= 1 lepton	= 1 lepton with $ \eta(\ell) < 1.2$	= 1 lepton		
Jets	≥ 4 with $p_T > 80, 60, 40, 25 \text{ GeV}$	≥ 3 with $p_T > 80, 40, 30 \text{ GeV}$	≥ 4 with $p_T > 80, 60, 40, 25 \text{ GeV}$		≥ 4 with $p_T > 80, 80, 40, 25 \text{ GeV}$
b-tagging/veto	≥ 2 (80% eff.) with $p_T > 140, 75 \text{ GeV}$	$= 0$ (70% eff.) with $p_T > 25 \text{ GeV}$	≥ 1 (70% eff.) with $p_T > 25 \text{ GeV}$	≥ 2 (80% eff.) with $p_T > 75, 75 \text{ GeV}$	≥ 2 (80% eff.) with $p_T > 170, 80 \text{ GeV}$
E_T^{miss}	$> 170 \text{ GeV}$	$> 140 \text{ GeV}$	$> 150 \text{ GeV}$		$> 160 \text{ GeV}$
m_T	$> 60 \text{ GeV}$	$> 120 \text{ GeV}$	$> 60 \text{ GeV}$	$> 120 \text{ GeV}$	
$E_T^{\text{miss}}/\sqrt{H_T}$	$> 6 \text{ GeV}^{1/2}$	$> 5 \text{ GeV}^{1/2}$	$> 7 \text{ GeV}^{1/2}$	$> 9 \text{ GeV}^{1/2}$	$> 8 \text{ GeV}^{1/2}$
am_{T2}	$> 80 \text{ GeV}$	–	$> 80 \text{ GeV}$	$> 200 \text{ GeV}$	$> 250 \text{ GeV}$
Track, τ-veto	track & loose τ -veto	–	track & loose τ -veto		
$\Delta R(j_1, \ell)$	–	$\in [0.8, 2.4]$	–		
$\Delta\phi(\text{jet}, \vec{p}_T^{\text{miss}})$	> 0.8 (1 st and 2 nd jet)	> 2.0 (1 st jet), > 0.8 (2 nd jet)	> 0.8 (1 st and 2 nd jet)		
Model-dependent selection:					
	shape-fit in m_T and am_{T2} , cf. figure 9.	cut-and-count	shape-fit in m_T and am_{T2} , cf. figure 9.	cut-and-count	
Model-independent selection:					
	test 4 most signal-sensitive bins one-by-one.	cut-and-count	test 4 most signal-sensitive bins one-by-one.	cut-and-count	

Table 6. Selection criteria for SRs employed to search for $\tilde{t}_1 \rightarrow b\tilde{\chi}_1^\pm$ decays. The first SR targets mass hierarchy (b), the next SR is designed for mass hierarchy (c), and the last three SRs are optimised for mass hierarchy (d), as illustrated in figure 4.

E_T^{miss} variables further enhance the signal-to-background ratio, by selecting events where the two stops recoil from an ISR jet.

Selections for mass hierarchy (d):

Signal models with relatively large mass splittings between the three mass states, \tilde{t}_1 , $\tilde{\chi}_1^\pm$, and $\tilde{\chi}_1^0$, result in events where all particles from the two \tilde{t}_1 decays are well above the identification p_T thresholds. Three SRs, labelled `bCd_bulk`, `bCd_high1`, and `bCd_high2`, target specific mass regions.

The `bCd_bulk` SR employs a two-dimensional shape-fit technique with bins in the $m_T - am_{T2}$ plane. Figure 9 (right plot) illustrates the binning. Compared to `bCb_med2`, which uses the same two variables in a shape-fit, a loose and more inclusive event selection is employed. The `bCd_high1` and `bCd_high2` SRs are based on tight event selections, leading to low expected background yields. Table 6 details the event selections.

7.4 Selections for the mixed, three- and four-body decays

Three additional stop decay modes are considered: Events where $\tilde{t}_1 \rightarrow t\tilde{\chi}_1^0$ and $\tilde{t}_1 \rightarrow b\tilde{\chi}_1^\pm$ decays are both allowed, with the branching ratios of the two decays summing to one; both stops decay via a three-body process ($\tilde{t}_1 \rightarrow bW\tilde{\chi}_1^0$); and both stops undergo a four-body decay ($\tilde{t}_1 \rightarrow bff'\tilde{\chi}_1^0$).

In the mixed decay mode, models with a very large and a very small $\mathcal{BR}(\tilde{t}_1 \rightarrow t\tilde{\chi}_1^0)$ are well covered by the SRs targeting the pure $\tilde{t}_1 \rightarrow t\tilde{\chi}_1^0$ and $\tilde{t}_1 \rightarrow b\tilde{\chi}_1^\pm$ decays, respectively. A dedicated SR with the label `tNbC_mix` is optimised for models with $\mathcal{BR}(\tilde{t}_1 \rightarrow t\tilde{\chi}_1^0) \sim 0.5$. It employs a requirement on the *topness* variable, which was designed specifically for the mixed decay mode, to suppress the dominant dileptonic $t\bar{t}$ background. Diboson events that pass the selection tend to have a leptonic W boson decay and a hadronic W or Z decay, accompanied by at least two additional jets. Large E_T^{miss} can be generated by the neutrino when the diboson system is sufficiently boosted; the two additional jets hence typically arise from ISR activity. The diboson background is suppressed by placing a loose upper requirement on the three-jet invariant mass, m_{jjj} . The jet-jet pair with an invariant mass above 60 GeV that has the smallest ΔR is selected to form the hadronic V boson. The mass m_{jjj} is reconstructed from the third jet closest in ΔR to the hadronic V boson momentum vector. Table 7 lists the entire event selection.

A dedicated SR labelled `3body` is optimised for the three-body decay mode. Compared to the scenario with on-shell top quarks, three-body decays yield the same final state objects but with significantly lower momenta, although typically still above the reconstruction thresholds. The dileptonic $t\bar{t}$ background is separated from signal in the very low am_{T2} regime. The three-body signal peaks in am_{T2} below around 100 GeV due to the kinematic construction of the variable and the fact that $m(\tilde{t}_1) - m(\tilde{\chi}_1^0)$ is below the top quark mass. A two-dimensional shape-fit technique using the m_T and am_{T2} variables is employed, similar to that used in `bCd_bulk` and `bCb_med2`, but with different binning. The configuration is illustrated in figure 6 (right plot). Fine binning is used in the low am_{T2} region where the highest signal sensitivity is obtained. The full `3body` event selection is detailed in table 7.

	tNbC_mix	3body
Preselection	Default preselection criteria, cf. table 3.	
Lepton	$= 1$ lepton	
Jets	≥ 4 jets with $p_T > 80, 70, 50, 25$ GeV	≥ 4 jets with $p_T > 80, 25, 25, 25$ GeV
b-tagging	≥ 1 b-tag (70% eff.) with $p_T > 60$ GeV	≥ 1 b-tag (70% eff.) with $p_T > 25$ GeV
E_T^{miss}	> 270 GeV	> 150 GeV
m_T	> 130 GeV	> 60 GeV
am_{T2}	> 190 GeV	> 80 GeV
<i>topness</i>	> 2	—
m_{jjj}	< 360 GeV	—
$E_T^{\text{miss}}/\sqrt{H_T}$	> 9 GeV $^{1/2}$	> 5 GeV $^{1/2}$
τ-veto	loose	
$\Delta\phi(\text{jet}_i, \vec{p}_T^{\text{miss}})$	> 0.6 ($i = 1, 2$)	> 0.2 ($i = 1, 2$)
$\Delta\phi(\ell, \vec{p}_T^{\text{miss}})$	> 0.6	> 1.2
$\Delta R(\ell, \text{jet}_i)$	< 2.75 ($i = 1$)	> 1.2 ($i = 1$), > 2.0 ($i = 2$)
$\Delta R(\ell, b\text{-jet})$	< 3.0	—
Model-dependent selection:		
	cut-and-count	shape-fit in m_T and am_{T2} , cf. figure 6.
Model-independent selection:		
	cut-and-count	test 4 most signal-sensitive bins one-by-one.

Table 7. Selection criteria for the two SRs employed to search for the mixed $\tilde{t}_1 \rightarrow t\tilde{\chi}_1^0$ and $\tilde{t}_1 \rightarrow b\tilde{\chi}_1^\pm$ decay mode (left), and the three-body decay, $\tilde{t}_1 \rightarrow bW\tilde{\chi}_1^0$ (right).

The four-body decay mode is characterised by events with final state objects that tend to have even lower momenta than for three-body decays. The selections based on a soft lepton designed for the overall ‘compressed’ mass hierarchy (a) provide good search sensitivity for this scenario.

8 Background estimates

The dominant sources of background are the production of $t\bar{t}$ events and $W+\text{jets}$ where the W decays leptonically. Other background processes considered are single top, dibosons, $Z+\text{jets}$, $t\bar{t}$ produced with a vector boson ($t\bar{t}V$), and multijet events.

The $t\bar{t}$ and W +jets backgrounds are estimated by isolating each of them in a dedicated control region, normalising simulation to match data in that control region, and then using simulation to extrapolate the background predictions into the SR. A detailed description of the method and its validation are given below.

The multijet background is estimated from data using a matrix method described in refs. [130, 131]. The contribution is found to be negligible for all but the soft-lepton selections. All other (small) backgrounds are determined entirely from simulation, normalised to the most accurate theoretical cross-sections available (cf. section 5).

8.1 Control regions

Each cut-and-count analysis has two orthogonal CRs which are enriched in either $t\bar{t}$ events (TCR) or W +jets events (WCR). These CRs are used to normalise the corresponding backgrounds in data, specifically for the associated SR. For the two-dimensional shape-fits, bins enriched in $t\bar{t}$ events are already part of the SR and act as a TCR, while additional bins are used to normalise the W +jets background. The one-dimensional shape-fits are set up similar to the cut-and-count analyses, with two additional bins acting as TCR and WCR. The CRs are designed to select events as similar as possible to those selected by the corresponding SR while keeping the contamination from other backgrounds and potential signal low. The CRs are also chosen to retain a sufficiently large number of events to not be limited by the statistical precision. This background estimation approach improves the robustness against potential mis-modelling effects in simulation since the dependence on simulation is reduced, and hence it reduces the uncertainties on the background estimates.

A likelihood fit is performed for each analysis, involving all associated bins: SR, TCR, WCR for cut-and-count or all bins of a shape-fit. Each bin is modelled by a separate probability density function based on a Poisson term, where the expected number of events is given by the sum over all background processes, and optionally a signal model. The normalisation of the $t\bar{t}$ and W +jets backgrounds is controlled by two free parameters in the fit.¹⁰ To obtain a set of background predictions that is independent of the observation in the SRs, the fit can be configured to use only the CRs to constrain the fit parameters: the SR bins (or signal-sensitive bins in shape-fits) are removed from the likelihood and any potential signal contribution is neglected everywhere. This fit configuration, referred to as the background-only fit, is used throughout this section. The treatment of systematic uncertainties in the likelihood fits is discussed in section 9. To quantify a potential excess, or to derive exclusion limits, the SR bins are included in the likelihood, as further detailed in section 10.

The key observable used to define the TCR and WCR for most analyses is the transverse mass. Figure 10 shows the m_T distribution for events passing the preselection defined in section 7.1 and with ≥ 1 (left) or ≥ 2 b -tagged jets (right) using the 70% and 80% working points, respectively. The $t\bar{t}$ and W +jets backgrounds drop sharply beyond the W boson mass, while signal events can exceed this kinematic endpoint due to the two additional

¹⁰ For some of the two-dimensional shape-fits, the $t\bar{t}$ and W +jets backgrounds are controlled by more than two parameters, as discussed later in the text.

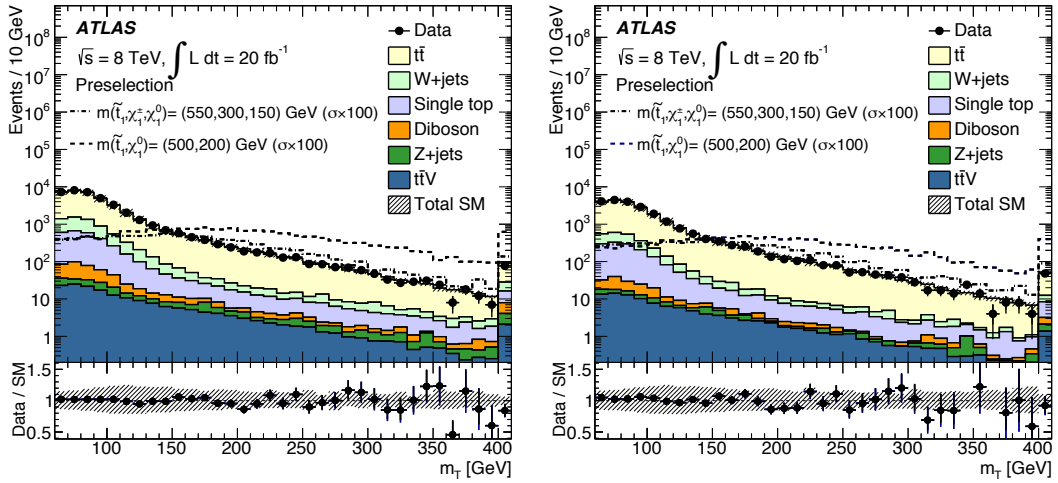


Figure 10. Distribution of the transverse mass, m_T , for events that pass the same preselection as used in figure 5 and with at least one (left) or at least two (right) b -tagged jets. The uncertainty band includes statistical and all experimental systematic uncertainties. The last bins include the overflows. Benchmark signal models with cross-sections enhanced by a factor of 100 are overlaid for comparison.

LSPs in the event. In all cut-and-count analyses the CRs differ from the associated SR by the m_T requirement, which is set to $60 \text{ GeV} < m_T < 90 \text{ GeV}$ for the CRs. For the four SRs based on a soft lepton, which all employ one-dimensional shape-fits, the two CRs are defined by loosening the E_T^{miss} and m_T requirements (`bCa_med` and `bCa_low`), or the soft-lepton selection of $6(7) \text{ GeV} < p_T(\ell) < 25 \text{ GeV}$ for muons (electrons) in the SR is changed to a $p_T(\ell) > 25 \text{ GeV}$ requirement in the CRs (`bCb_med1` and `bCb_high`). All WCRs have a b -tag veto instead of a b -tag requirement to reduce the $t\bar{t}$ contamination; consequently all requirements related to the presence of a b -jet are removed. The b -tag requirement used in all but one SR enhances the heavy-flavour contribution of the $W+\text{jets}$ background, while the WCRs with the b -tag veto predominantly select light-flavour $W+\text{jets}$ events. A systematic uncertainty and a dedicated validation related to this effect are described in section 9 and in the next subsection, respectively. The TCRs employ the same b -tagging requirement as used in the associated SRs, except for `bCc_diag` where the b -tag veto in the SR is turned into a ≥ 1 b -tag requirement in the TCR (using the same b -tagging working point as for the b -tag veto in the SR). Furthermore, some other kinematic requirements are slightly loosened or removed to increase the event yields in the CRs. The event selections for all CRs associated with the cut-and-count or the one-dimensional shape-fit analyses are specified in table 8. In each analysis the same two CRs are used for the model-dependent and the model-independent fit configurations.

The four two-dimensional shape-fits (`tN_diag`, `3body`, `bCb_med2`, and `bCd_bulk`) have built-in bins enhanced in $t\bar{t}$ events, which act as TCRs, while additional WCR bins are added with a b -tag veto and with a $60 \text{ GeV} < m_T < 90 \text{ GeV}$ requirement (as can be seen

Analysis	Variable	Control regions		Validation regions		Signal reg. SR
		TCR	WCR	TVR	WVR	
All tN_*	m_T N_b	[60, 90] ≥ 1	[60, 90] $= 0$	[90, 120] ≥ 1	[90, 120] $= 0$	$> [140, 200]$ ≥ 1
tN_med	am_{T2}	> 120	> 120	> 120	> 120	> 170
tN_high	am_{T2}	-	-	-	-	> 170
	m_{T2}^τ	-	-	-	-	> 120
	E_T^{miss}	> 225	> 225	> 225	> 225	> 320
	H_T^{sig}	> 8.8	> 8.8	> 8.8	> 8.8	> 12.5
tN_boost	am_{T2}	> 130	> 130	> 130	> 130	> 145
	E_T^{miss}	> 260	> 260	> 260	> 260	> 315
	topness	-	-	-	-	> 7
All bCa_*	$p_T(\ell)$ N_b	$> 6(7)$ ≥ 1	$> 6(7)$ $= 0$	[6(7),25] ≥ 1	[6(7),25] ≥ 1	[6(7),25/50] ≥ 1
bCa_low	E_T^{miss}	[200,250]	[200,250]	[250,370]	[250,370]	> 370
	m_T	[90,120]	[90,120]	> 90	> 90	> 90
	$E_T^{\text{miss}}/m_{\text{eff}}$	-	-	-	> 0.35	> 0.35
bCa_med	E_T^{miss}	[200,250]	[200,250]	[250,300]	[250,300]	> 300
	m_T	[100,120]	[100,120]	> 100	> 100	> 100
	$E_T^{\text{miss}}/m_{\text{eff}}$	-	-	-	> 0.3	> 0.3
All bCb_*	$p_T(\ell)$ N_b m_T m_{bb}	> 25 $= 2$ -	> 25 $= 0$ [40, 80]	[6(7),25] $= 2$ -		[6(7),25] $= 2$ -
bCb_med1	am_{T2}	-	-	-		> 170
bCb_high	am_{T2}	-	-	-		> 200
	E_T^{miss}	> 250	> 150	> 250		> 250
All bCc_*, bCd_*	m_T	[60, 90]	[60, 90]	[90, 120]	[90, 120]	> 120
bCc_diag	N_b	≥ 1	$= 0$	≥ 1	$= 0$	$= 0$
All bCd_*	N_b	≥ 2	$= 0$	≥ 2	$= 0$	≥ 2
bCd_high1	am_{T2}	> 120	> 200	> 120	> 200	> 200
bCd_high2	am_{T2}	> 120	> 250	> 120	> 250	> 250
tNbC_mix	m_T	[60, 90]	[60, 90]	[90, 120]	[90, 120]	> 130
	N_b	≥ 1	$= 0$	≥ 1	$= 0$	≥ 1
	am_{T2}	> 120	> 120	> 120	> 120	> 190
	E_T^{miss}	> 170	> 170	> 170	> 170	> 270
	$E_T^{\text{miss}}/\sqrt{H_T}$	> 5	> 5	> 5	> 5	> 9

Table 8. Event selections for control regions, validation regions, and the signal regions of the model-independent selection (defined in tables 4–6) associated with cut-and-count or one-dimensional shape-fit analyses. The asterisk symbol ‘*’ is used as a wildcard to describe variable requirements common to several regions. Only one validation region is defined for the bCb_med1 and bCb_high selections. Variables for which the requirements are the same between the regions are not listed. Requirements related to the presence of a b -tagged jet are removed in all selections with a b -tag veto (WCRs and WVRs). All units are in GeV except for unitless quantities and $E_T^{\text{miss}}/\sqrt{H_T}$ which is quoted in $\text{GeV}^{1/2}$.

in figures 6 and 9). For the background-only fits, the WCRs and the subset of the TCR shape-fit bins with $m_T < 90\text{ GeV}$ are used to constrain the likelihood fit. The $t\bar{t}$ and $W+\text{jets}$ backgrounds are normalised separately in each E_T^{miss} or am_{T2} slice in the `tN_diag` and `bCd_bulk` shape-fits, as these two have sufficiently large numbers of events in the low- m_T bins. Thus, there are three $t\bar{t}$ and three $W+\text{jets}$ normalisation parameters, which are applied to all m_T bins in the given E_T^{miss} or am_{T2} range. This approach increases the robustness of the fit against potential mis-modelling in the simulation at the expense of a reduced statistical precision. For the other two shape-fits with lower event yields, `3body` and `bCb_med2`, one $t\bar{t}$ and one $W+\text{jets}$ normalisation parameter is applied across all bins. All shape-fit bins are used to extract model-dependent exclusion limits, while a subset is used for the model-independent results and for the background only fits. This subset includes all bins with $m_T < 90\text{ GeV}$, acting as CR bins, and in addition for the model-independent results one signal-sensitive bin is included.

Top pair and $W+\text{jets}$ production accounts for 70–80% of events in the TCRs and WCRs. The signal contamination, for all signal models studied and all CRs, is typically at the percent level and never exceeds 10%. It is explicitly taken into account when setting model-dependent exclusion limits.

Table 9 shows the background predictions in each SR. The number of $t\bar{t}$ and $W+\text{jets}$ events are estimated using the background-only fit configuration. For the four two-dimensional shape-fits, the background predictions are given for the four bins with the highest signal-sensitivity. The quoted uncertainties include all statistical and systematic effects, described in section 9. The numbers of $t\bar{t}$ events normalised in the various TCRs are compatible with the predictions entirely based on simulation and the theoretical cross-section, while the $W+\text{jets}$ estimates are about 30% lower than, but nonetheless compatible with the predictions from simulation normalised to the theoretical cross-section. Tables showing the estimated and fitted number of background events in the CRs, validation regions, and SRs of all analyses are shown in appendix B.

8.2 Validation

The background fit predictions are validated using dedicated event samples. For each cut-and-count and one-dimensional shape-fit analysis one or more dedicated validation regions (VRs) are defined for the $t\bar{t}$ and $W+\text{jets}$ backgrounds. The VRs are designed to be kinematically close to the associated SRs to test the background estimates in regions of phase space as similar as possible to the SRs. For most analyses the associated VRs are defined following a similar strategy as used for the CRs but with a $90\text{ GeV} < m_T < 120\text{ GeV}$ requirement, which leads to a set of events orthogonal to both the associated CRs and the SR. The event selections for the $t\bar{t}$ and $W+\text{jets}$ VRs, TVR and WVR respectively, are given in table 8. Another set of $t\bar{t}$ validation regions, referred to as TVR2 but not shown in the table, is defined where applicable by inverting the SR requirement on am_{T2} while keeping all other requirements the same as in the SR. For the four two-dimensional shape-fits, a subset of the shape-fit bins in the region falling in between that dominated by $t\bar{t}$ and the region enhanced by a potential signal is used for the $t\bar{t}$ background validation. These signal-depleted shape-fit bins are referred to as validation bins.

Signal region	Total bkg.	$t\bar{t}$	$W+\text{jets}$	Single top	Diboson	$Z+\text{jets}$	$t\bar{t}V$	Multijet
tN_med	13.0 ± 2.2	6.5 ± 1.7	2.1 ± 0.5	1.1 ± 0.5	1.4 ± 0.6	0.009 ± 0.005	2.0 ± 0.6	—
tN_high	5.0 ± 1.0	2.0 ± 0.6	0.87 ± 0.26	0.54 ± 0.19	0.86 ± 0.31	0.0030 ± 0.0020	0.75 ± 0.25	—
tN_boost	3.3 ± 0.7	1.1 ± 0.4	0.28 ± 0.14	0.39 ± 0.15	0.72 ± 0.25	0.0040 ± 0.0020	0.85 ± 0.28	—
bCa_low	6.5 ± 1.4	2.8 ± 0.9	1.1 ± 0.5	0.9 ± 0.4	1.0 ± 0.6	0.018 ± 0.017	0.23 ± 0.09	$0.6^{+0.8}_{-0.6}$
bCa_med	17 ± 4	10.5 ± 3.1	1.2 ± 0.5	1.7 ± 0.9	1.1 ± 0.6	$0.022^{+0.134}_{-0.022}$	0.47 ± 0.17	2.5 ± 2.0
bCb_medi	32 ± 5	15 ± 4	9.5 ± 2.8	6.2 ± 1.2	0.060 ± 0.018	0.23 ± 0.13	0.13 ± 0.04	$0.7^{+2.1}_{-0.7}$
bCb_high	9.8 ± 1.6	3.8 ± 0.8	2.5 ± 0.9	2.9 ± 0.8	0.075 ± 0.024	0.10 ± 0.06	0.27 ± 0.10	$0.18^{+0.52}_{-0.18}$
bCc_diag	470 ± 50	140 ± 40	248 ± 27	12.1 ± 3.0	59 ± 17	5.2 ± 2.6	3.3 ± 1.1	—
bCd_high1	11.0 ± 1.5	5.2 ± 1.0	1.9 ± 0.5	1.9 ± 0.8	0.38 ± 0.18	0.047 ± 0.024	1.5 ± 0.5	—
bCd_high2	4.4 ± 0.8	1.8 ± 0.4	0.71 ± 0.33	1.1 ± 0.5	0.25 ± 0.19	0.047 ± 0.024	0.48 ± 0.16	—
tNbC_mix	7.2 ± 1.0	2.9 ± 0.6	1.30 ± 0.30	0.70 ± 0.30	0.8 ± 0.4	< 0.001	1.4 ± 0.4	—
tN_diag								
$125 < E_T^{\text{miss}} < 150 \text{ GeV}, 120 < m_T < 140 \text{ GeV}$	136 ± 22	123 ± 22	6.5 ± 2.5	5.3 ± 2.2	0.29 ± 0.18	0.17 ± 0.08	1.5 ± 0.5	—
$125 < E_T^{\text{miss}} < 150 \text{ GeV}, m_T > 140 \text{ GeV}$	152 ± 20	137 ± 20	5.8 ± 2.6	5.8 ± 2.1	0.8 ± 0.5	0.24 ± 0.12	2.9 ± 0.9	—
$E_T^{\text{miss}} > 150 \text{ GeV}, 120 < m_T < 140 \text{ GeV}$	98 ± 13	85 ± 12	4.6 ± 1.5	5.8 ± 2.1	0.34 ± 0.32	0.30 ± 0.15	2.5 ± 0.8	—
$E_T^{\text{miss}} > 150 \text{ GeV}, m_T > 140 \text{ GeV}$	236 ± 29	202 ± 27	10 ± 4	9.0 ± 3.5	4.0 ± 1.8	0.53 ± 0.26	10.8 ± 3.3	—
bCb_med2								
$175 < am_{T2} < 250 \text{ GeV}, 90 < m_T < 120 \text{ GeV}$	12.1 ± 2.0	8.5 ± 1.8	1.8 ± 0.8	1.6 ± 0.7	0.018 ± 0.007	< 0.001	0.26 ± 0.10	—
$175 < am_{T2} < 250 \text{ GeV}, m_T > 120 \text{ GeV}$	7.4 ± 1.4	4.8 ± 1.2	0.47 ± 0.19	1.2 ± 0.6	0.01 ± 0.10	< 0.001	0.85 ± 0.27	—
$am_{T2} > 250 \text{ GeV}, 90 < m_T < 120 \text{ GeV}$	21 ± 4	12.1 ± 3.1	3.9 ± 1.4	4.5 ± 2.0	0.32 ± 0.12	< 0.001	0.25 ± 0.08	—
$am_{T2} > 250 \text{ GeV}, m_T > 120 \text{ GeV}$	9.1 ± 1.6	4.0 ± 1.1	2.2 ± 0.9	1.8 ± 0.8	0.29 ± 0.13	0.047 ± 0.024	0.74 ± 0.27	—
bCd_bulk								
$175 < am_{T2} < 250 \text{ GeV}, 90 < m_T < 120 \text{ GeV}$	133 ± 22	87 ± 16	29 ± 7	13 ± 5	2.2 ± 1.0	0.019 ± 0.010	1.5 ± 0.5	—
$175 < am_{T2} < 250 \text{ GeV}, m_T > 120 \text{ GeV}$	73 ± 8	46 ± 7	12.2 ± 3.5	6.9 ± 2.5	3.0 ± 1.4	0.29 ± 0.15	4.8 ± 1.4	—
$am_{T2} > 250 \text{ GeV}, 90 < m_T < 120 \text{ GeV}$	66 ± 6	33 ± 7	20 ± 4	11 ± 4	1.8 ± 1.0	0.11 ± 0.06	0.56 ± 0.18	—
$am_{T2} > 250 \text{ GeV}, m_T > 120 \text{ GeV}$	26.5 ± 2.6	10.8 ± 2.5	6.9 ± 1.6	4.7 ± 1.6	1.9 ± 0.9	0.22 ± 0.11	2.0 ± 0.6	—
3body								
$100 < am_{T2} < 120 \text{ GeV}, 90 < m_T < 120 \text{ GeV}$	68 ± 9	60 ± 9	3.9 ± 2.1	3.0 ± 2.8	0.38 ± 0.20	0.08 ± 0.04	0.28 ± 0.12	—
$100 < am_{T2} < 120 \text{ GeV}, m_T > 120 \text{ GeV}$	75 ± 11	67 ± 12	4.1 ± 1.8	2.3 ± 1.4	0.55 ± 0.18	0.16 ± 0.08	0.73 ± 0.23	—
$am_{T2} > 120 \text{ GeV}, 90 < m_T < 120 \text{ GeV}$	179 ± 23	145 ± 21	22 ± 6	9 ± 5	1.4 ± 0.7	0.20 ± 0.10	1.1 ± 0.4	—
$am_{T2} > 120 \text{ GeV}, m_T > 120 \text{ GeV}$	306 ± 30	239 ± 32	35 ± 10	18 ± 7	5.8 ± 2.2	1.6 ± 0.8	6.5 ± 2.1	—

Table 9. Background estimates in the SRs (model-independent selection) of the 15 analyses obtained from CRs for $t\bar{t}$ and $W+\text{jets}$, from data for multijet events, and from simulation normalised to theoretical cross-sections for all other backgrounds. The quoted uncertainties include all statistical and systematic effects. The sum in quadrature of the uncertainties of all backgrounds may not add up to the total uncertainty due to correlations.

For the cut-and-count and one-dimensional shape-fit analyses, the VRs are not used in any fit configuration to constrain the fit parameters. The validation bins of the two-dimensional shape-fits, on the other hand, are not used in the background-only fit configuration but are included in the model-dependent fit configuration. The number of background events in each VR or validation bin is predicted by the background-only fit (using simulation for the extrapolation) and compared to the data, as shown in the upper panel of figure 11. The lower panel shows the pull for each bin, where the pull is defined as the difference between the predicted background and the observed number of events divided by the total uncertainty. The latter is given by the full uncertainty of the prediction (described in section 9) added in quadrature with the statistical uncertainty of the observed number of events. No indication of background mis-modelling is found. VRs or validation bins belonging to different analyses can share events, and the systematic uncertainties are correlated across different regions and bins.

Several other cross checks are performed to further validate the background estimations. For the SRs requiring more than two jets, dileptonic $t\bar{t}$ events can pass the event selection only if they contain additional jets beyond the two b -jets from the leading-order description of the decay. The modelling of these additional jets, which in the simulation arise from radiation or higher-order-corrections, and which is relevant for the background estimation, is validated using a dedicated sample. The event selection is based on requiring one isolated electron and one oppositely-charged, isolated muon, as well as two or more jets of which at least one is b -tagged using the 70% working point. This selects a clean sample of $t\bar{t}$ events, which is used in figure 12 (left) to compare the jet multiplicity distributions between data and simulation. Data is modelled sufficiently well within the systematic uncertainties. Further dedicated validation samples are used to test the modelling of the $t\bar{t}$ background with a τ_{had} or isolated track. These samples are based on the common event preselection and inverting either the track- or τ -veto. The simulation is found to model data well within uncertainties.

The W +jets light- vs heavy-flavour composition in the WCR can be different from that in the SR. A dedicated validation is performed by selecting a sample enriched with W +heavy-flavour jets events. The event selection is based on exactly one isolated lepton, and exactly three jets (the fourth jet veto reduces $t\bar{t}$ events), of which at least one is b -tagged. Furthermore, events are required to have $60 \text{ GeV} < m_T < 90 \text{ GeV}$, $E_T^{\text{miss}} > 150 \text{ GeV}$, and the two jets with the highest b -tagging weights are required to yield an invariant mass below 80 GeV and to have a limited separation in η - ϕ space to increase the sensitivity to pair-produced heavy-flavour jets in association with a W boson. The selected sample of 166 events has a predicted W +heavy-flavour jets component of about 40%; data are found to be in good agreement with simulation, predicting 171 events, when the overall W +jets background is normalised to match data in a b -veto control region.¹¹

Another dedicated validation sample is constructed to test the background prediction for $t\bar{t}$ produced with a Z boson that decays to two neutrinos, $t\bar{t}Z(\rightarrow\nu\bar{\nu})$. This process

¹¹The W +jets background is normalised using the WCR associated with `bCc_diag`, which requires three or more jets with a jet p_T selection similar to that used in the validation sample.

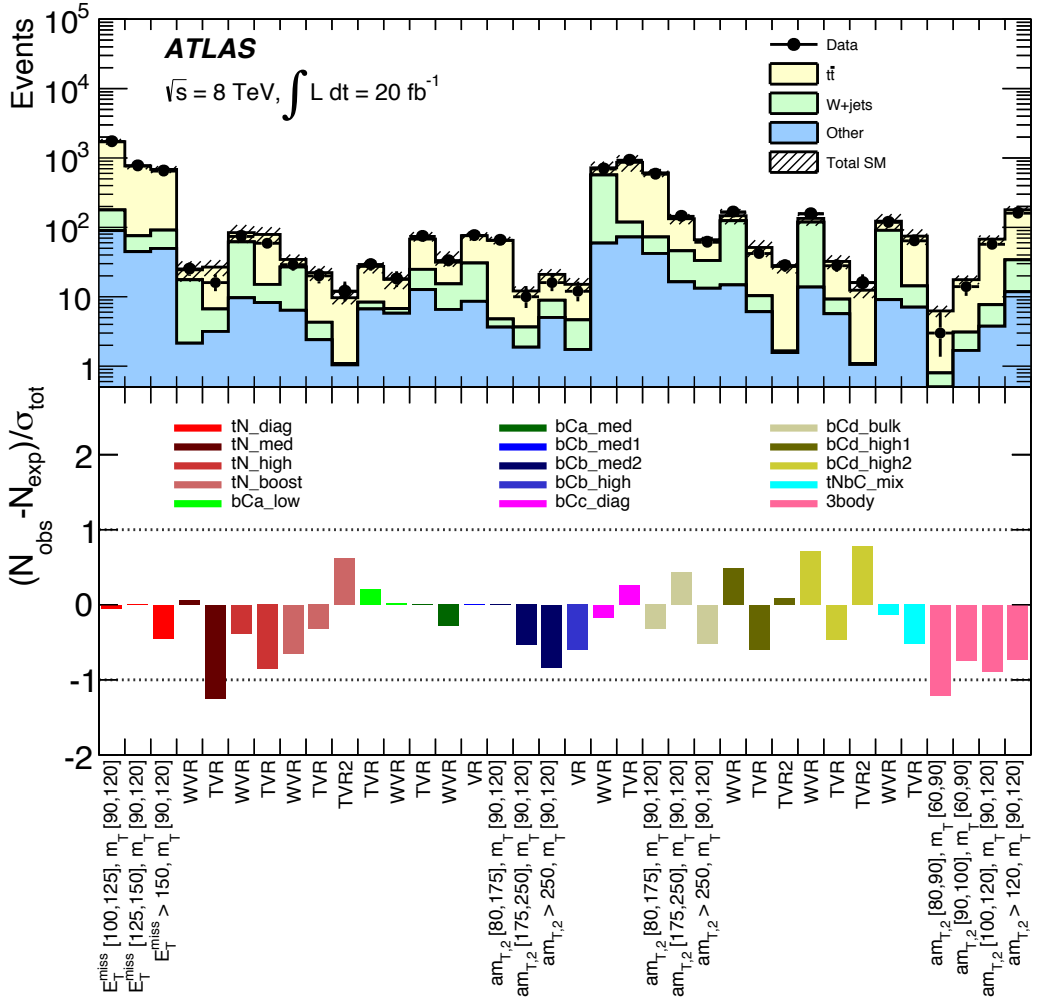


Figure 11. The upper panel compares data with background predictions in the VRs of the cut-and-count and one-dimensional shape-fit analyses as well as the validation bins of the two-dimensional shape-fit analyses. The lower panel shows the pull of the same bins. The $t\bar{t}$ and $W+\text{jets}$ background estimates are obtained using the background-only fit to the CRs (described in the text). All statistical and systematic uncertainties are included.

represents an irreducible background that becomes important for SRs with stringent requirements on kinematic variables, such as tN_{high} or tN_{boost} . The validation strategy is to select $t\bar{t}$ events produced in association with a photon, $t\bar{t}\gamma$. This process closely resembles $t\bar{t}Z(\rightarrow \nu\bar{\nu})$ in terms of Feynman diagrams and kinematic properties when the vector boson p_T is well above m_Z . The event selection is based on one isolated lepton, four or more jets with at least one b -tag, one high- p_T photon, as well as requirements on modified versions of m_T and E_T^{miss} where photons are treated as invisible particles. Figure 12 (right)

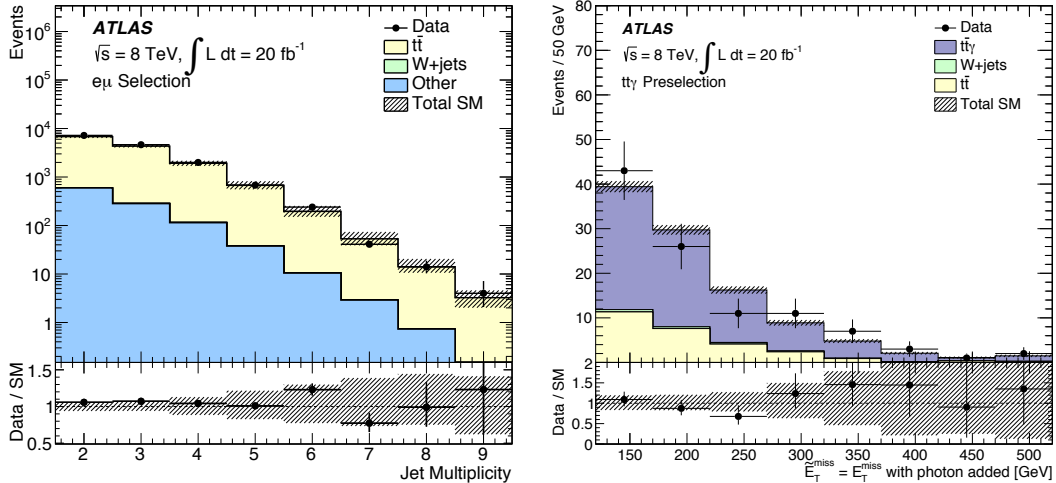


Figure 12. Left: Jet multiplicity distribution for events with one opposite charged electron-muon pair and at least two jets of which one or more is b -tagged. Other processes include single top quark production, $t\bar{t}$ production in association with a vector boson, $Z+jets$, and diboson production. Right: Missing transverse momentum where photons are treated as invisible particles ($\tilde{E}_T^{\text{miss}}$) for an event selection of $t\bar{t}\gamma$ + photon (described in the text). Both plots: The uncertainty band includes all statistical and experimental uncertainties, and the last bins include overflows.

compares data and background predictions, illustrating the accuracy of data modelling. The sample of 104 events has a purity in $t\bar{t}\gamma$ of more than 70%. The production of $t\bar{t}\gamma$ events is estimated using simulation, based on the same generator (MADGRAPH) as used for the $t\bar{t}Z$ process, and normalised to the NLO theoretical cross-section [132].

9 Systematic uncertainties

The systematic uncertainties affecting the results can be divided into two classes: uncertainties due to theoretical predictions and modelling, and uncertainties stemming from experimental effects. The impact of both types of uncertainty is evaluated for all background and signal samples. Since the yields for the dominant background sources, $t\bar{t}$ and $W+jets$, are obtained in dedicated control regions, the modelling uncertainties for these processes affect only the extrapolation from the CRs into the signal regions (and between TCR and WCR), but not the overall normalisation. The systematic uncertainties are included as nuisance parameters and profiled in the likelihood fits. The nuisance parameters are constrained by Gaussian terms with widths corresponding to the sizes of the systematic uncertainties. The same set of nuisance parameters is used across all bins, with the exception of the two shape-fits that have three $t\bar{t}$ and three $W+jets$ normalisation parameters and hence also have three sets of nuisance parameters. The effects of the sources of uncertainties discussed in this section are quantified in terms of the corresponding relative

uncertainty on the estimated number of background events in the various signal regions, this is referred to as the ‘impact on the background estimate’.

The dominant experimental uncertainties arise from imperfect knowledge of the jet energy scale (JES) and jet energy resolution (JER) as well as from the modelling of the b -tagging efficiency. The JES uncertainty is derived from a combination of simulation and data samples [105, 106] taking into account the dependence on the p_T , η and flavour of the jet as well as the amount of pileup. The impact of JES on the background estimate varies from 1% to 13%. The JER uncertainties are determined with in-situ measurements of the jet response balance in dijet events [129], and the impact on the background estimate is 1%–21%. The JES, JER, and jet mass scale and resolution uncertainties for large- R jets are derived from a combination of data and simulation samples [107, 133], and their combined impact on the background estimate amounts to 3%. The b -tagging uncertainty is estimated by varying the b -tagging efficiency and mis-tag rate correction factors, obtained from data-driven measurements of these quantities in $t\bar{t}$ and dijet events [111, 134–136], within their uncertainties. The impact of these uncertainties on the background estimate ranges from 1% to 8%, and is dominated by the uncertainty on the b -tagging efficiency. Other sources of experimental uncertainty are the modelling of the average number of pp interactions per bunch crossing, the modelling of the contribution to the E_T^{miss} from energy deposits not associated with any reconstructed objects and from pileup, the modelling of lepton-related quantities (trigger and identification efficiency, energy and momentum scale and resolution, isolation and τ -veto) as well as imperfect knowledge of the integrated luminosity. The combined impact of these sources on the background estimate is between 1% and 5%.

Uncertainties related to theoretical predictions and MC modelling are evaluated for all signal and background processes obtained entirely or partly from simulated events. The sources of uncertainty considered for both the $t\bar{t}$ and $W+\text{jets}$ background processes are the variations of the renormalisation and factorisation scales by factors of 0.5 and 2.0 as well as PDF variations, which are studied following the PDF4LHC recommendations [137] comparing CT10 NLO, MSTW2008 NNLO and NNPDF21_100 [138] PDF error sets. For the $t\bar{t}$ background, the uncertainty on the hadronisation modelling is derived from a comparison between events generated with POWHEG and interfaced with PYTHIA for the shower model and those generated in the same way, but interfaced with HERWIG+JIMMY [139]. Furthermore, the effect of the modelling of ISR and final-state radiation (FSR) is studied using samples of $t\bar{t}$ events generated with ACERMC with reduced and increased amounts of additional radiation (constrained by the measurement of ref. [140]). The impact of the $t\bar{t}$ modelling on the background estimate is 2%–6%. For the $W+\text{jets}$ background, the effect of varying the number of partons used in the hard-scatter process is estimated by comparing samples generated with up to four extra partons to samples generated with up to five extra partons. The impact of merging matrix elements and parton showers is studied by varying the SHERPA scales related to the matching scheme. As the $W+\text{jets}$ background is normalised in a region with a b -tag veto, additional uncertainties on the flavour composition of the $W+\text{jets}$ events in the signal region, based on the uncertainties on the measurement of ref. [141] extrapolated to higher jet multiplicities, are applied in all regions requiring at

least one b -tagged jet. The impact of the $W + \text{jets}$ modelling on the background estimate is 1%–7%.

Background sources other than $t\bar{t}$ and $W + \text{jets}$ are estimated from simulated events and are normalised to the most accurate cross-section predictions available. The cross-section uncertainty for the single-top process is 7% [82–84], while it is 22% for $t\bar{t}V$ [85, 86]. The ZZ and WZ cross-section uncertainties are 5% and 7%, respectively [89, 90]. Other sources of systematic uncertainty considered depend on the physics process, but include the choice of renormalisation and factorisation scales, PDF variations, hadronisation modelling, choice of MC generator, modelling of ISR and FSR, variations of the matrix element to parton shower matching scales, the generation of a finite number of partons, and the interference between single-top and $t\bar{t}$ production at NLO. The uncertainty on the interference treatment is estimated using inclusive $WWbb$ samples at LO generated with ACERMC (which includes both the $t\bar{t}$ and Wt processes). The total impact of the modelling of the smaller backgrounds on the background estimate ranges from 1% to 11%.

The theoretical uncertainties affecting the signal yields originate from the uncertainty on the production cross-section [96], and from the uncertainty on the acceptance. The latter includes PDF variations assessed using the PDF4LHC prescription [137], as well as modelling uncertainties of ISR and FSR and variations of the renormalisation and factorisation scales, evaluated by varying the relevant parameters in MADGRAPH. The total uncertainty on the production cross-section varies as a function of the stop mass; it amounts to about 15% for $m_{\tilde{t}_1} = 200$ GeV and increases to 18% for $m_{\tilde{t}_1} = 700$ GeV. The impact of the ISR/FSR modelling uncertainty on the signal acceptance ranges from 10% to 20% for signal regions that select events with ISR activity, such as `bCc_diag`, and for signal models of mass hierarchy (c). It is negligible for the other signal regions.

The search sensitivity is directly connected to the fitted uncertainty of the signal strength parameter, where the signal strength is a fit parameter that scales the signal yield predicted by the model in question; a signal strength of one corresponds to the nominal signal yield. The impact of the various sources of uncertainty, including the statistical precision, on the signal strength uncertainty is quantified in table 10 for selected signal regions and signal benchmark models. The breakdown of the size of the systematic uncertainties is evaluated by re-running the fit, fixing the relevant nuisance parameter in question to its value from the nominal fit, and taking the difference in quadrature between the signal strength uncertainty of this fit and the nominal fit. The statistical uncertainty is obtained from re-running the fit without any systematic uncertainties, again fixing the nuisance parameters to their values from the nominal fit. The tightest signal regions, such as `tN_boost`, are statistically limited. Systematic uncertainties dominate the looser signal regions. Overall, the largest contributions to the systematic uncertainty on the signal strength come from JER and $t\bar{t}$ modelling. The energy scale and energy resolution of large- R jets is relevant in the `tN_boost` signal region.

Uncertainty on signal strength	tN_boost	tN_diag	bCc_diag	bCd_bulk
Total	0.37	0.19	0.11	0.16
Statistical	0.36	0.05	0.07	0.09
Systematic	0.09	0.18	0.09	0.13
Contribution of systematic uncertainty components				
Jet energy scale	0.02	0.03	0.02	0.03
Jet energy resolution	0.06	0.11	0.06	0.07
Large- R -jet related	0.03	-	-	-
E_T^{miss} (non-associated energy and pileup)	0.01	0.06	0.01	0.03
Pileup	< 0.01	0.03	0.01	0.02
b -tagging	0.03	0.01	0.04	0.01
$t\bar{t}$ modelling	0.01	0.15	0.04	0.08
$W+\text{jets}$ modelling	< 0.01	0.01	0.02	0.03
Other backgrounds modelling	0.04	0.03	0.02	0.02
Signal acceptance modelling	0.02	0.01	0.02	0.01

Table 10. Breakdown of the size of uncertainties on the signal strength parameter of the likelihood fit. The central values of the signal strength parameters (not shown) are close to zero because the data are compatible with the predicted backgrounds. The uncertainty components are obtained from the difference in quadrature between the signal strength uncertainty of the nominal fit and a fit where the systematic uncertainty in question is disabled by fixing the corresponding nuisance parameter(s) to the value(s) from the nominal fit. Some systematic uncertainty components, such as the jet energy scale or the modelling of backgrounds, are displayed as single entries while the likelihood fit employs a more detailed description. The sum in quadrature of the systematic uncertainty components may not add up to the total systematic uncertainty due to correlations. The following benchmark signal models are used: $m_{\tilde{t}_1} = 700 \text{ GeV}$ and $m_{\tilde{\chi}_1^0} = 1 \text{ GeV}$ for `tN_boost`, $m_{\tilde{t}_1} = 350 \text{ GeV}$ and $m_{\tilde{\chi}_1^0} = 150 \text{ GeV}$ for `tN_diag` $m_{\tilde{t}_1} = 180 \text{ GeV}$, $m_{\tilde{\chi}_1^\pm} = 174 \text{ GeV}$ and $m_{\tilde{\chi}_1^0} = 87 \text{ GeV}$ for `bCc_diag` $m_{\tilde{t}_1} = 300 \text{ GeV}$, $m_{\tilde{\chi}_1^\pm} = 200 \text{ GeV}$ and $m_{\tilde{\chi}_1^0} = 100 \text{ GeV}$ for `bCd_bulk`.

10 Results

Figures 13 and 14 show comparisons between the observed data and the SM background prediction from the background-only fit with all selections applied except the requirement on the plotted variable. In all SRs, the plots indicate good compatibility between the data and the SM background. The expected distributions from representative signal benchmark models are overlaid.

Table 11 shows the number of observed events together with the predicted number of background events in the SRs using the model-independent selection of the 15 analyses. The predicted numbers of background events are obtained using the background-only fits to the number of observed events in the CRs as described in section 8. These fitted background estimates in the CRs are then used to obtain the fitted numbers of background events in the SRs by extrapolations that use transfer factors obtained with simulated events. The observed numbers of events are found to agree well with the fitted numbers of background events in all SRs.

To assess the compatibility of the SM background-only hypothesis with the observa-

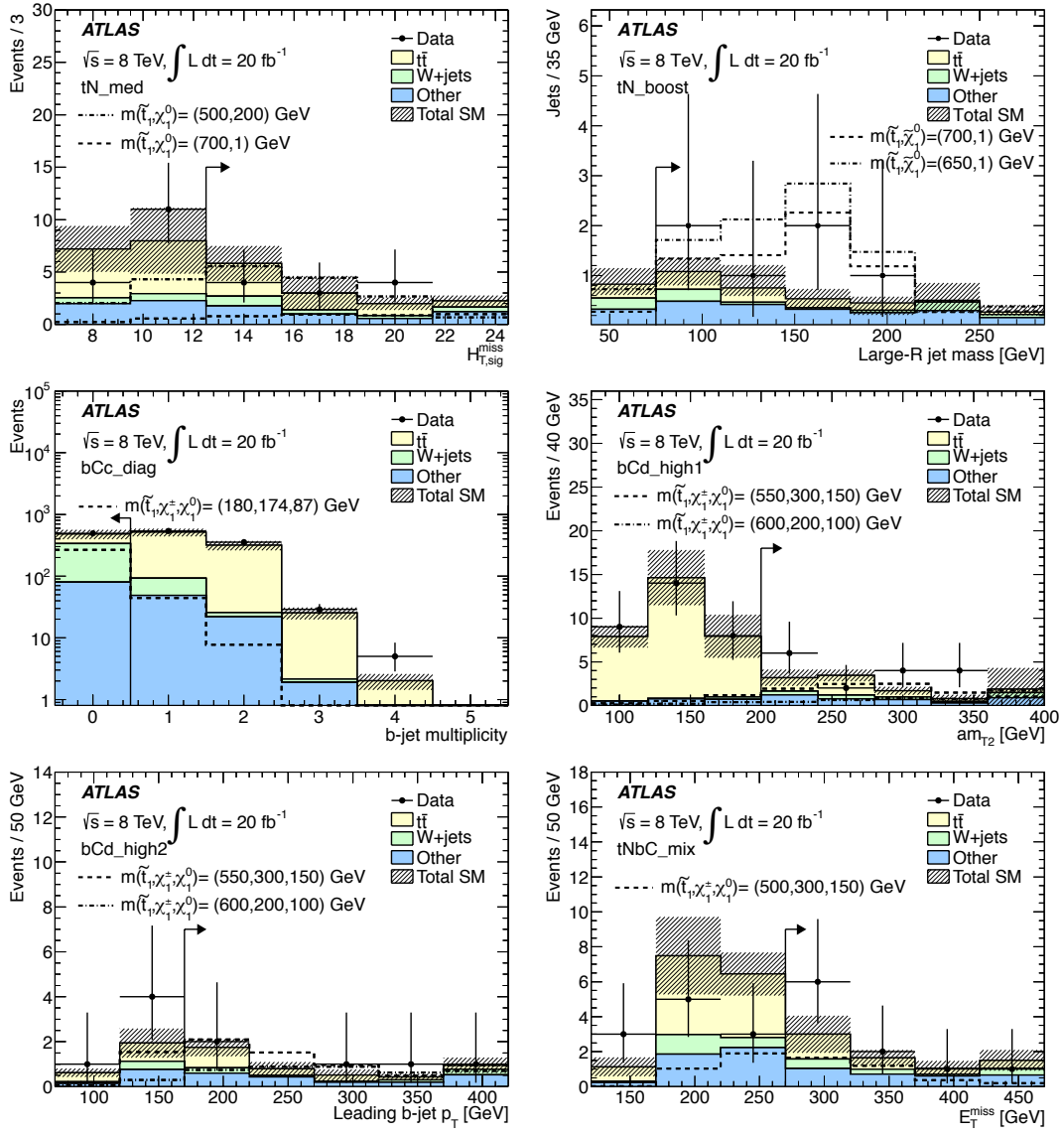


Figure 13. For each signal region one characteristic distribution is shown, with the full event selection of the signal region applied, except for the requirement (indicated by an arrow) on the shown quantity. The uncertainty band includes statistical and all experimental systematic uncertainties. The last bin includes overflows. Benchmark signal models are overlaid for comparison.

tions in the SRs, a profile likelihood ratio test is performed implementing the methodology described in ref. [143]. The model-independent selection is used, and the likelihood for a given test includes one SR and all its associated CRs. Each SR, and each signal-sensitive bin in the two-dimensional shape-fits, is probed separately. Table 11 shows the p_0 values obtained using these fits, indicating that the data in all SRs are compatible with the background-only hypothesis. Good agreement is found when comparing the results ob-

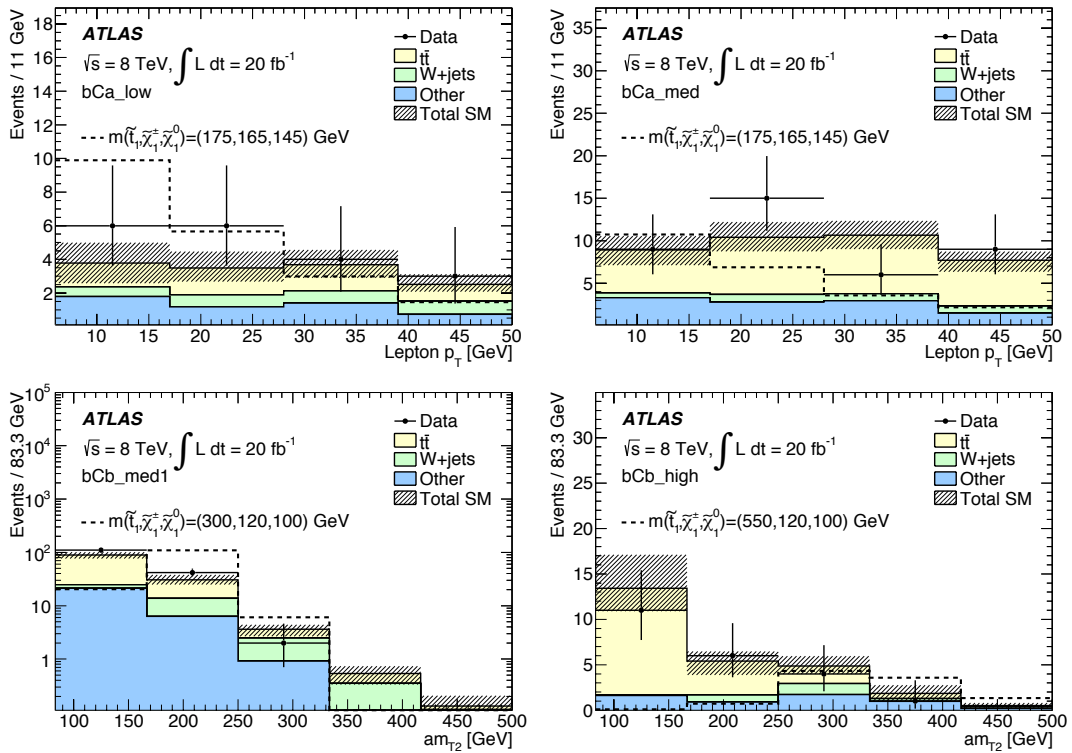


Figure 14. For each signal region one characteristic distribution is shown, with the full event selection of the signal region applied, except for the requirement on the shown quantity. The binning is similar to that used for the one-dimensional shape-fits of the corresponding analyses. The uncertainty band includes statistical and all experimental systematic uncertainties. The last bin includes overflows. Benchmark signal models are overlaid for comparison.

tained using pseudo-experiments to those calculated from asymptotic formulae [142]; the latter is used as the default for all exclusion results presented below.

As no significant excess over the expected background from SM processes is observed, the data are used to derive one-sided limits at 95% CL. The results are obtained from a profile likelihood ratio test following the CL_s prescription [143]. Model-independent upper limits on beyond-SM contributions are derived separately for each analysis, and in case of the two-dimensional shape-fits for each signal-sensitive bin. The model-independent selection is used, and the likelihood of the fit is configured to include one SR or shape-fit bin and all its associated CRs. A generic signal model, which contributes only to the SR, is assumed and no experimental or theoretical signal systematic uncertainties are assigned other than the luminosity uncertainty. The resulting limits on the number of beyond-SM events and on the visible signal cross-section are shown in the rightmost columns of table 11. The visible signal cross-section (σ_{vis}) is defined as the product of acceptance (A), reconstruction efficiency (ϵ) and production cross-section (σ_{prod}); it is obtained by dividing the upper limit on the number of beyond-SM events by the integrated luminosity.

Signal region	Obs.	Exp. bkg.	p_0	$N_{\text{non-SM}}$ Obs.	$N_{\text{non-SM}}$ Exp.	σ_{vis} [fb] Obs.	σ_{vis} [fb] Exp.
tN_med	12	13.0 ± 2.2	≥ 0.5	8.5	9.2	0.4	0.5
tN_high	5	5.0 ± 1.0	≥ 0.5	6.0	6.0	0.3	0.3
tN_boost	5	3.3 ± 0.7	0.17	7.0	5.3	0.3	0.3
bCa_low	11	6.5 ± 1.4	0.08	12.2	7.8	0.61	0.92
bCa_med	20	17 ± 4	0.33	14.4	12.3	0.72	0.68
bCb_med1	41	32 ± 5	0.12	23.5	16.0	1.17	0.88
bCb_high	7	9.8 ± 1.6	≥ 0.5	6.5	7.9	0.32	0.22
bCc_diag	493	470 ± 50	0.27	110.6	95.1	5.4	4.7
bCd_high1	16	11.0 ± 1.5	0.09	13.2	8.5	0.7	0.4
bCd_high2	5	4.4 ± 0.8	0.36	6.3	5.7	0.3	0.3
tNbC_mix	10	7.2 ± 1.0	0.13	9.7	7.0	0.5	0.3
tN_diag							
$125 < E_T^{\text{miss}} < 150 \text{ GeV}, \quad 120 < m_T < 140 \text{ GeV}$	117	136 ± 22	≥ 0.5	42.1	55.7	2.1	2.7
$125 < E_T^{\text{miss}} < 150 \text{ GeV}, \quad m_T > 140 \text{ GeV}$	163	152 ± 20	0.35	55.4	47.8	2.7	2.4
$E_T^{\text{miss}} > 150 \text{ GeV}, \quad 120 < m_T < 140 \text{ GeV}$	101	98 ± 13	0.43	36.1	33.9	1.8	1.7
$E_T^{\text{miss}} > 150 \text{ GeV}, \quad m_T > 140 \text{ GeV}$	217	236 ± 29	≥ 0.5	58.7	71.4	2.9	3.5
bCb_med2							
$175 < am_{T2} < 250 \text{ GeV}, \quad 90 < m_T < 120 \text{ GeV}$	10	12.1 ± 2.0	≥ 0.5	7.3	8.8	0.4	0.4
$175 < am_{T2} < 250 \text{ GeV}, \quad m_T > 120 \text{ GeV}$	10	7.4 ± 1.4	0.10	9.7	7.3	0.5	0.4
$am_{T2} > 250 \text{ GeV}, \quad 90 < m_T < 120 \text{ GeV}$	16	21 ± 4	≥ 0.5	9.3	12.3	0.5	0.6
$am_{T2} > 250 \text{ GeV}, \quad m_T > 120 \text{ GeV}$	9	9.1 ± 1.6	≥ 0.5	7.7	7.8	0.4	0.4
bCd_bulk							
$175 < am_{T2} < 250 \text{ GeV}, \quad 90 < m_T < 120 \text{ GeV}$	144	133 ± 22	0.29	36.1	33.9	1.8	1.7
$175 < am_{T2} < 250 \text{ GeV}, \quad m_T > 120 \text{ GeV}$	78	73 ± 8	0.34	58.7	71.4	2.9	3.5
$am_{T2} > 250 \text{ GeV}, \quad 90 < m_T < 120 \text{ GeV}$	61	66 ± 6	≥ 0.5	17.5	20.9	0.9	1.0
$am_{T2} > 250 \text{ GeV}, \quad m_T > 120 \text{ GeV}$	29	26.5 ± 2.6	0.34	14.8	12.6	0.7	0.6
3body							
$80 < am_{T2} < 90 \text{ GeV}, \quad 90 < m_T < 120 \text{ GeV}$	12	16.9 ± 2.8	≥ 0.5	7.3	9.9	0.4	0.5
$80 < am_{T2} < 90 \text{ GeV}, \quad m_T > 120 \text{ GeV}$	8	8.4 ± 2.2	≥ 0.5	7.9	7.8	0.4	0.4
$90 < am_{T2} < 100 \text{ GeV}, \quad 90 < m_T < 120 \text{ GeV}$	29	35 ± 4	≥ 0.5	11.7	14.7	0.6	0.7
$90 < am_{T2} < 100 \text{ GeV}, \quad m_T > 120 \text{ GeV}$	22	29 ± 5	≥ 0.5	55.4	47.8	2.7	2.4

Table 11. Columns two to four show the numbers of observed events in the SRs (model-independent selection) of the 15 analyses together with the expected numbers of background events (as predicted by the background-only fits) and the probabilities, represented by the p_0 values, that the observed numbers of events are compatible with the background-only hypothesis. The p_0 values are obtained with pseudo-experiments with the exception of the shape-fit bins where only the smallest p_0 is derived with pseudo-experiments while the others are calculated from asymptotic formulae [142]. The p_0 value is set to 0.5 whenever the number of observed events is below the number of expected events. Columns five to eight show the 95% CL upper limits on the number of beyond-SM events ($N_{\text{non-SM}}$) and on the visible signal cross-section ($\sigma_{\text{vis}} = \sigma_{\text{prod}} \times A \times \epsilon$). The observed and (median) expected limits are given for a generic model without uncertainties other than on the luminosity.

Exclusion limits are also derived in various SUSY scenarios. The results are obtained using the same CL_s prescription as used for the model-independent limits, but with the

model-dependent selection. The likelihood for each analysis includes the full set of bins: SR, TCR, WCR for cut-and-count and the full set of SR and CR bins for shape-fit analyses. The signal uncertainties and potential signal contributions to all bins are taken into account. All uncertainties except on the theoretical signal cross-section are included in the fit. Combined exclusion limits are obtained by selecting a priori the signal region with the lowest expected CL_s value for each signal grid point.

The expected and observed exclusion contours for the $\tilde{t}_1 \rightarrow t\tilde{\chi}_1^0$ decay mode are shown in figure 15 overlaying the results for the signal regions targeting two-, three- and four-body decays. The $\pm 1\sigma_{\text{exp}}$ uncertainty band indicates the impact on the expected limit of all uncertainties included in the fit. The $\pm 1\sigma_{\text{theory}}^{\text{SUSY}}$ uncertainty lines around the observed limit illustrate the change in the observed limit as the nominal signal cross-section is scaled up and down by the theoretical cross-section uncertainty. Quoted limits are derived from the $-1\sigma_{\text{theory}}^{\text{SUSY}}$ observed limit contours. In the four-body scenario stop masses are excluded between 100 and 170 GeV, for an LSP mass of about 75 GeV. Stop masses between 100 and nearly 175 GeV in the three-body scenario, and between 210 and 640 GeV in the two-body scenario are excluded for a massless LSP, while for a stop mass around 550 GeV the exclusion reaches up to an LSP mass of 230 GeV. The non-excluded area between the four- and three-body decay regions is due to a reduction in search sensitivity as the kinematic properties of the signal change significantly when transitioning from a four-body to a three-body decay. In particular, approaching this boundary from the three-body side, the momenta of the two b -jets decrease to zero and hence the acceptance of the p_T requirement on the b -tagged jet in the 3body signal region drops quickly. The kinematic properties change again at the other diagonal, between the three-body and on-shell top quark decay modes. When approaching this diagonal from the on-shell top quark side the search sensitivity is limited by the difficulty to disentangle the signal from the $t\bar{t}$ background, as the two processes begin to closely resemble each other in kinematic properties. In the limit of reaching the diagonal from the righthand side, the two LSPs have no phase space, thus carrying away no momentum, leading to a stop signature similar to that of $t\bar{t}$ except for small deviations induced by the difference in spin. This region is also referred to as ‘stealth stop’. The **tN_diag** signal region has the best expected sensitivity for stop masses up to 400 GeV and close to the $m_{\tilde{t}_1} \gtrsim m_t + m_{\tilde{\chi}_1^0}$ kinematic boundary, while the **tN_boost** signal region has the best expected sensitivity for stop masses above 600 GeV. In the intermediate mass region the best expected sensitivity comes from the **tN_med** signal region. The use of large-R jets in the **tN_boost** signal region extends the reach for a heavy stop by about 30 GeV, as obtained from a comparison with the **tN_high** signal region.

Figures 16 to 21 show the expected and observed exclusion contours for the $\tilde{t}_1 \rightarrow b\tilde{\chi}_1^\pm$ decay mode with different $\tilde{\chi}_1^\pm$ mass hypotheses. If the mass of the $\tilde{\chi}_1^\pm$ is twice that of the LSP (figure 16), stop masses up to 500 GeV are excluded for an LSP mass in the range of 100 to 150 GeV. The various regions in the exclusion area can be mapped to the mass hierarchies illustrated in figure 4: Models in the bulk region correspond to mass hierarchy (d), those in the (bottom) region with a low $\tilde{\chi}_1^0$ mass are mass hierarchy (b), and the ones in the (diagonal) region close to the kinematic boundary are mass hierarchy (c). The strongest exclusion sensitivity is provided by the signal regions designed for the given mass

hierarchy, for example `bCd_bulk` (bulk), `bCb_med1` and `bCb_high` (bottom), and `bCc_diag` (diagonal). The small region around $m_{\tilde{t}_1} \sim 175$ GeV and $m_{\tilde{\chi}_1^0} \lesssim 70$ GeV is not excluded because signal events cannot be sufficiently well distinguished from $t\bar{t}$ background events; for larger $m_{\tilde{\chi}_1^0}$ values, the b -tag veto in the `bCc_diag` signal region becomes effective.

If the $\tilde{\chi}_1^\pm$ mass is set to 150 GeV (figure 17), stop masses below 490 GeV are excluded for LSP masses up to 80 GeV. Models in the top, left, and bulk regions within the exclusion contour correspond to the mass hierarchies (a-b), (c), and (d) respectively; the exclusion power is mostly provided by `bCb_med1` and `bCb_high` (top), `bCc_diag` (left), `bCd_bulk` (bulk), and `bCb_med2` (bulk with high $m_{\tilde{t}_1}$). The vertical drop in search sensitivity for $m_{\tilde{t}_1} \lesssim 260$ GeV in the top part of the plane is caused by the b -tagged jet p_T and m_{bb} requirements in the two `bCb_*` signal regions, which effectively imposes a minimum mass splitting between the \tilde{t}_1 and $\tilde{\chi}_1^\pm$ states. The other two signal regions that are based on soft-lepton selections (`bCa_*`) require ISR activity and are hence limited to the low stop mass region where the cross-section is large. The sharp horizontal contour line at $m_{\tilde{\chi}_1^0} = 145$ GeV is an artifact caused by the fact that signal grid points were generated only up to this LSP mass. However, the upper region is excluded by the search described in ref. [37]. If the mass of the $\tilde{\chi}_1^\pm$ is set to 106 GeV (figure 18), stop masses between 240 and 550 GeV, together with a small region around a stop mass of 150 GeV, are excluded for an LSP mass of 70 GeV. The identification of regions with mass hierarchies, and the best signal regions are similar to the previous scenario. The vertical exclusion gap around $m_{\tilde{t}_1} \sim 175$ GeV is due to the same effect seen in figure 16 and described above, while the reduction in exclusion power for a decreasing LSP mass is due to the transition of the $\tilde{\chi}_1^\pm$ decay from a three-body to a two-body process, which happens at an LSP mass of ~ 26 GeV; the two-body decay produces less E_T^{miss} on average, amongst other changes of the kinematic properties.

If the $\tilde{\chi}_1^\pm$ mass is only 5 GeV (20 GeV) above the LSP mass (figures 19 and 20, respectively), stop masses between 265 and 600 GeV (240 and 600 GeV) are excluded for an LSP mass of 100 GeV. The exclusion in these ‘compressed’ scenarios, corresponding to the mass hierarchies (a) and (b), is achieved using the soft-lepton selections of the `bCa_low` and `bCa_med` signal regions. The sensitivity decreases for smaller mass splittings because of the lepton p_T threshold. The diagonal exclusion gap in figure 20 is caused by the effects described above in the discussion of figure 17 together with the impact of the b -veto on the leading jet in the `bCa_*` signal regions. If the $\tilde{\chi}_1^\pm$ mass is only 10 GeV below the stop mass (figure 21), stop masses below 390 GeV are excluded for a massless LSP. The models in this scenario correspond to mass hierarchy (c). The bulk exclusion power comes from the `bCc_diag` signal region with a b -veto, while using soft leptons in the `bCa_low` signal region extends the sensitivity in the top left region.

The complementarity of the signal regions to various mass splittings of $\tilde{\chi}_1^\pm$ and $\tilde{\chi}_1^0$ is illustrated by fixing the stop mass to 300 GeV and presenting the exclusion limit as a function of the $\tilde{\chi}_1^\pm$ and $\tilde{\chi}_1^0$ masses (figure 22). LSP masses up to about 100 GeV are excluded for all possible $\tilde{\chi}_1^\pm$ masses, with one small exception in the bottom left corner. The exclusion power close to the kinematic boundary comes from the signal regions designed for mass hierarchy (a) and (b), while for larger mass splittings the sensitivity is provided by the

selections for mass hierarchy (d), and (c) in case of a large $\tilde{\chi}_1^\pm$ mass. The non-excluded region around a $\tilde{\chi}_1^\pm$ mass of 270 GeV and a $\tilde{\chi}_1^0$ mass of 175 GeV is caused by the signal region transition.

In scenarios where both the $\tilde{t}_1 \rightarrow t\tilde{\chi}_1^0$ and $\tilde{t}_1 \rightarrow b\tilde{\chi}_1^\pm$ decay modes are allowed and where $m_{\tilde{\chi}_1^\pm} = 2m_{\tilde{\chi}_1^0}$ (figure 23), the largest excluded stop mass for an LSP mass of 100 GeV gradually increases from 530 GeV to 660 GeV as the branching ratio for $\tilde{t}_1 \rightarrow t\tilde{\chi}_1^0$ is increased from 0% to 100%. Here, the quoted limits correspond to the central observed limit contour. The signal regions providing the best expected sensitivity for models with mixed decays are mainly `bCd_bulk` and `tNbC_mix`, with some contribution from `tN_diag`, `tN_med` and `tN_boost` for models with a large fraction of $\tilde{t}_1 \rightarrow t\tilde{\chi}_1^0$ decays, as well as some contributions from `bCb_med1` and `bCb_high` for models with a low LSP mass and a small fraction of $\tilde{t}_1 \rightarrow t\tilde{\chi}_1^0$ decays.

The upper limits on the signal cross-section for models where the \tilde{t}_1 is a pure \tilde{t}_L and models where it is predominantly a \tilde{t}_R are compared in figure 24 for the $\tilde{t}_1 \rightarrow t\tilde{\chi}_1^0$ decay mode with two assumptions for the lightest neutralino, $m_{\tilde{\chi}_1^0} = 50$ GeV and $m_{\tilde{\chi}_1^0} = 150$ GeV. The predominantly \tilde{t}_R mixing composition is the default setting used for all simplified-model $\tilde{t}_1 \rightarrow t\tilde{\chi}_1^0$ scenarios. The weaker \tilde{t}_L model exclusion is mainly the result of a reduced lepton and m_T acceptance. The excluded \tilde{t}_1 mass reach of the \tilde{t}_L model is reduced by about 50 GeV for the two considered LSP masses.

The change in sensitivity when varying parameters other than the stop and $\tilde{\chi}_1^0$ masses is studied using 27 pMSSM samples, which can be classified into three groups of similar stop and $\tilde{\chi}_1^0$ masses; a detailed description is given in section 5.2. The expected and observed CL_s significance values for the 27 pMSSM models and two simplified models are shown in figure 25. The strongest impact on the CL_s significance is found to be from the sum of the branching ratios for $\tilde{t}_1 \rightarrow t\tilde{\chi}_1^0$ and $\tilde{t}_1 \rightarrow b\tilde{\chi}_1^\pm$, where the CL_s significance is smaller for models where stop decays other than $\tilde{t}_1 \rightarrow t\tilde{\chi}_1^0$ and $\tilde{t}_1 \rightarrow b\tilde{\chi}_1^\pm$ are kinematically allowed. This is a consequence of the signal selections being optimised using only simplified models. In addition to the branching ratio dependence, the sensitivity also depends on the kinematic properties of the events, which are affected, e.g., by the stop mixing matrix and by the masses and field content of other SUSY particles. These additional dependencies explain the large spread in CL_s significance for the models where the stop decays only to $t\tilde{\chi}_1^0$ and $b\tilde{\chi}_1^\pm$. For $m_{\tilde{t}_1} \sim 400$ GeV and $m_{\tilde{\chi}_1^0} \sim 50$ GeV, 11 of the 14 models are excluded. No models with $m_{\tilde{t}_1} \sim 550$ GeV are excluded.

11 Summary and conclusions

A search for stop pair production in final states with one isolated lepton, jets, and missing transverse momentum is presented. Proton–proton collision data from the full 2012 data-taking period were analysed, corresponding to an integrated luminosity of 20 fb^{-1} collected at $\sqrt{s} = 8$ TeV by the ATLAS detector at the LHC. Five decay modes are considered: (1) each stop decays to a top quark and the LSP; (2) each stop decays to a bottom quark and the lightest chargino ($\tilde{\chi}_1^\pm$), where the $\tilde{\chi}_1^\pm$ decays via an on- or off-shell W boson to the LSP; (3) each stop decays in a three-body process to a bottom quark, a W boson, and the

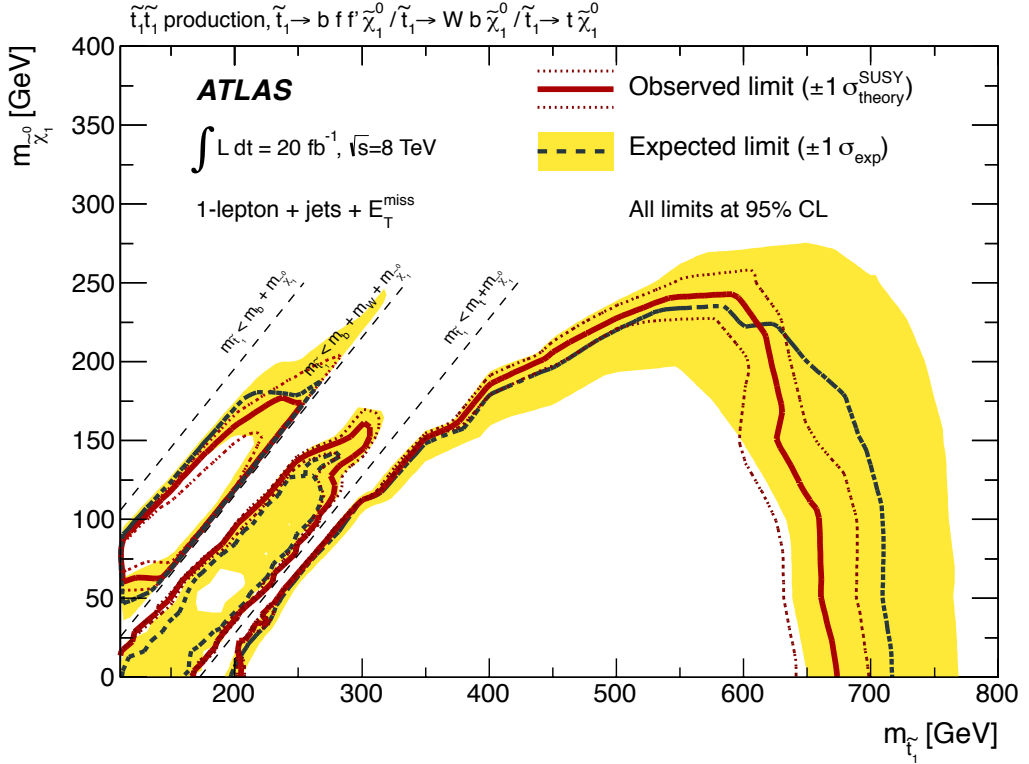


Figure 15. Expected (black dashed) and observed (red solid) 95% CL excluded region in the plane of $m_{\tilde{\chi}_1^0}$ vs. $m_{\tilde{t}_1}$, assuming $\mathcal{BR}(\tilde{t}_1 \rightarrow t\tilde{\chi}_1^0) = 100\%$. In the region $m_b + m_W + m_{\tilde{\chi}_1^0} < m_{\tilde{t}_1} < m_t + m_{\tilde{\chi}_1^0}$ the decay of the \tilde{t}_1 involves a virtual top quark (three-body decay), while in the region $m_{\tilde{t}_1} < m_b + m_W + m_{\tilde{\chi}_1^0}$ it involves both a virtual top quark and a virtual W boson (four-body decay). The $m_{\tilde{t}_1} < 100$ GeV region for the three-body decay mode is excluded by the search described in ref. [38]. Furthermore, the $m_{\tilde{t}_1} < 78$ GeV region in the four-body scenario is excluded by the search in ref. [144].

LSP; (4) each stop decays in a four-body process to a bottom quark, the LSP and two light fermions; (5) the two stops decay independently either as described in (1) or in (2). In all scenarios, R -parity is conserved and the LSP is assumed to be the $\tilde{\chi}_1^0$.

The results are in agreement with predictions from the Standard Model, and are thus translated into 95% CL upper limits on the stop and $\tilde{\chi}_1^0$ masses in various supersymmetric scenarios. For models where the stop decays exclusively into a top quark and a $\tilde{\chi}_1^0$ (scenario (1) above), stop masses between 210 and 640 GeV are excluded for a massless LSP, and stop masses around 550 GeV are excluded for LSP masses below 230 GeV. Limits are also derived in the three- and four-body scenarios. For scenarios where the stop decays exclusively into a bottom quark and a $\tilde{\chi}_1^\pm$ (scenario (2) above), the excluded stop and $\tilde{\chi}_1^0$ masses depend strongly on the mass of the $\tilde{\chi}_1^\pm$. For models where the mass of the $\tilde{\chi}_1^\pm$ is twice that of the LSP, stop masses up to 500 GeV are excluded for an LSP mass in the range of 100 to 150 GeV. For models in which the $\tilde{\chi}_1^\pm$ mass is only 20 GeV above the LSP mass, stop masses

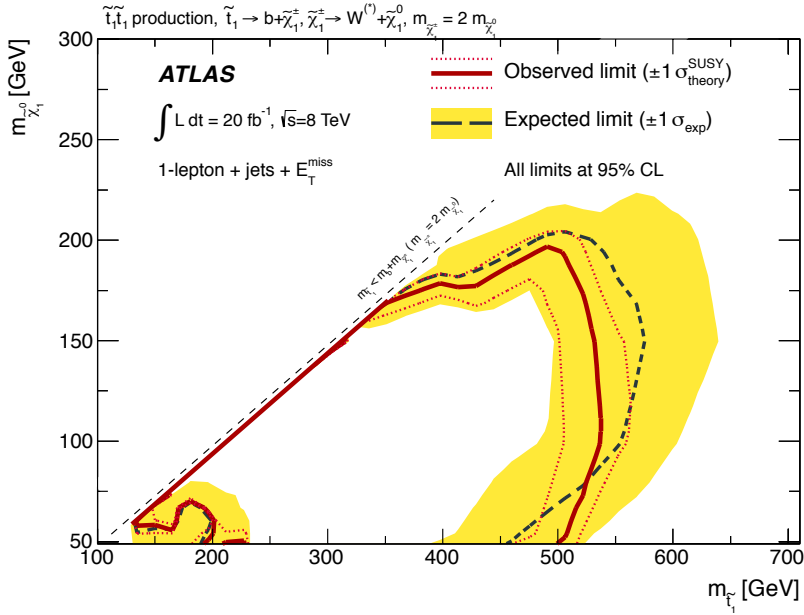


Figure 16. Expected (black dashed) and observed (red solid) 95% CL excluded region in the plane of $m_{\tilde{\chi}_1^0}$ vs. $m_{\tilde{t}_1}$, assuming $\mathcal{BR}(\tilde{t}_1 \rightarrow b\tilde{\chi}_1^\pm) = 100\%$, $\mathcal{BR}(\tilde{\chi}_1^\pm \rightarrow W^{(*)}\tilde{\chi}_1^0) = 100\%$ and $m_{\tilde{\chi}_1^\pm} = 2m_{\tilde{\chi}_1^0}$.

between 240 and 600 GeV are excluded for an LSP mass of 100 GeV. In scenarios where only the $\tilde{t}_1 \rightarrow t\tilde{\chi}_1^0$ and $\tilde{t}_1 \rightarrow b\tilde{\chi}_1^\pm$ decay modes are allowed, the largest excluded stop mass for an LSP mass of 100 GeV gradually increases from 530 GeV to 660 GeV as the branching ratio for $\tilde{t}_1 \rightarrow t\tilde{\chi}_1^0$ is increased from 0% to 100%. Using a limited set of pMSSM models, the exclusion power is found to decrease with an increased branching ratio to decays other than $\tilde{t}_1 \rightarrow t\tilde{\chi}_1^0$ and $\tilde{t}_1 \rightarrow b\tilde{\chi}_1^\pm$. These results supersede and significantly extend previous ATLAS limits.

12 Acknowledgements

We thank CERN for the very successful operation of the LHC, as well as the support staff from our institutions without whom ATLAS could not be operated efficiently.

We acknowledge the support of ANPCyT, Argentina; YerPhI, Armenia; ARC, Australia; BMWFW and FWF, Austria; ANAS, Azerbaijan; SSTC, Belarus; CNPq and FAPESP, Brazil; NSERC, NRC and CFI, Canada; CERN; CONICYT, Chile; CAS, MOST and NSFC, China; COLCIENCIAS, Colombia; MSMT CR, MPO CR and VSC CR, Czech Republic; DNRF, DNSRC and Lundbeck Foundation, Denmark; EPLANET, ERC and NSRF, European Union; IN2P3-CNRS, CEA-DSM/IRFU, France; GNSF, Georgia; BMBF, DFG, HGF, MPG and AvH Foundation, Germany; GSRT and NSRF, Greece; ISF, MINERVA, GIF, I-CORE and Benoziyo Center, Israel; INFN, Italy; MEXT and JSPS, Japan; CNRST, Morocco; FOM and NWO, Netherlands; BRF and RCN, Norway; MNiSW and NCN, Poland; GRICES and FCT, Portugal; MNE/IFA, Romania; MES

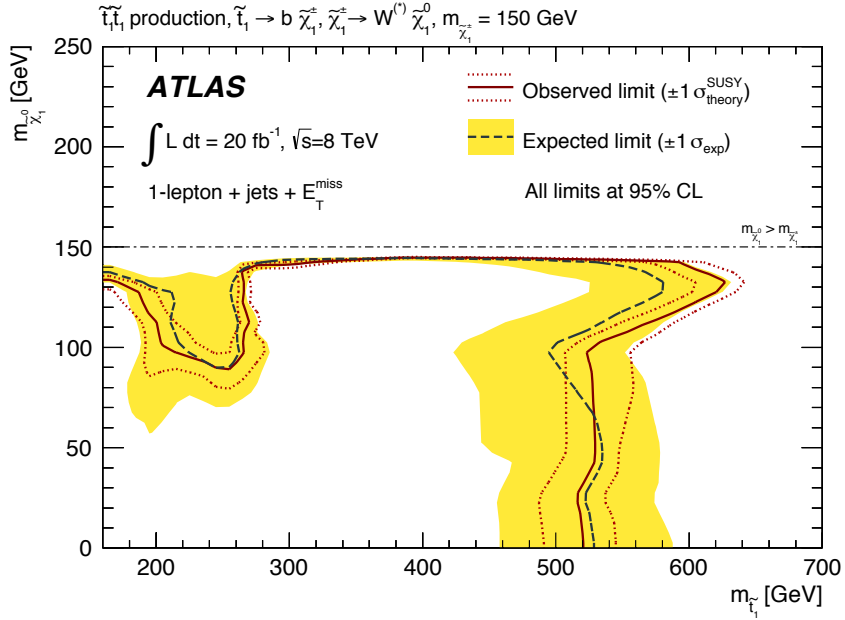


Figure 17. Expected (black dashed) and observed (red solid) 95% CL excluded region in the plane of $m_{\tilde{\chi}_1^0}$ vs. $m_{\tilde{t}_1}$, assuming $\mathcal{BR}(\tilde{t}_1 \rightarrow b\tilde{\chi}_1^\pm) = 100\%$, $\mathcal{BR}(\tilde{\chi}_1^\pm \rightarrow W^{(*)}\tilde{\chi}_1^0) = 100\%$ and $m_{\tilde{\chi}_1^\pm} = 150\text{ GeV}$.

of Russia and ROSATOM, Russian Federation; JINR; MSTD, Serbia; MSSR, Slovakia; ARRS and MIZŠ, Slovenia; DST/NRF, South Africa; MINECO, Spain; SRC and Wallenberg Foundation, Sweden; SER, SNSF and Cantons of Bern and Geneva, Switzerland; NSC, Taiwan; TAEK, Turkey; STFC, the Royal Society and Leverhulme Trust, United Kingdom; DOE and NSF, United States of America.

The crucial computing support from all WLCG partners is acknowledged gratefully, in particular from CERN and the ATLAS Tier-1 facilities at TRIUMF (Canada), NDGF (Denmark, Norway, Sweden), CC-IN2P3 (France), KIT/GridKA (Germany), INFN-CNAF (Italy), NL-T1 (Netherlands), PIC (Spain), ASGC (Taiwan), RAL (UK) and BNL (USA) and in the Tier-2 facilities worldwide.

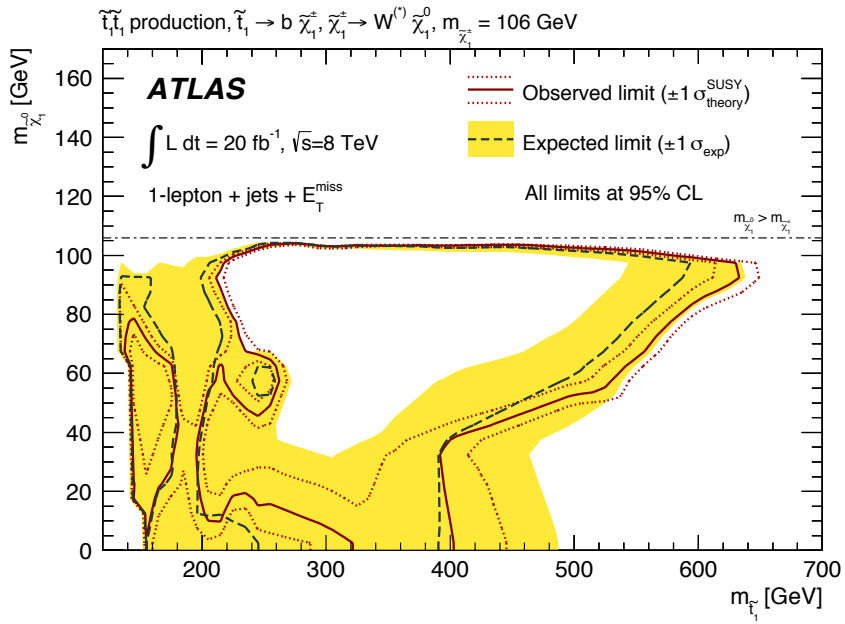


Figure 18. Expected (black dashed) and observed (red solid) 95% CL excluded region in the plane of $m_{\tilde{\chi}_1^0}$ vs. $m_{\tilde{t}_1}$, assuming $\mathcal{BR}(\tilde{t}_1 \rightarrow b\tilde{\chi}_1^\pm) = 100\%$, $\mathcal{BR}(\tilde{\chi}_1^\pm \rightarrow W^{(*)}\tilde{\chi}_1^0) = 100\%$ and $m_{\tilde{\chi}_1^\pm} = 106$ GeV.

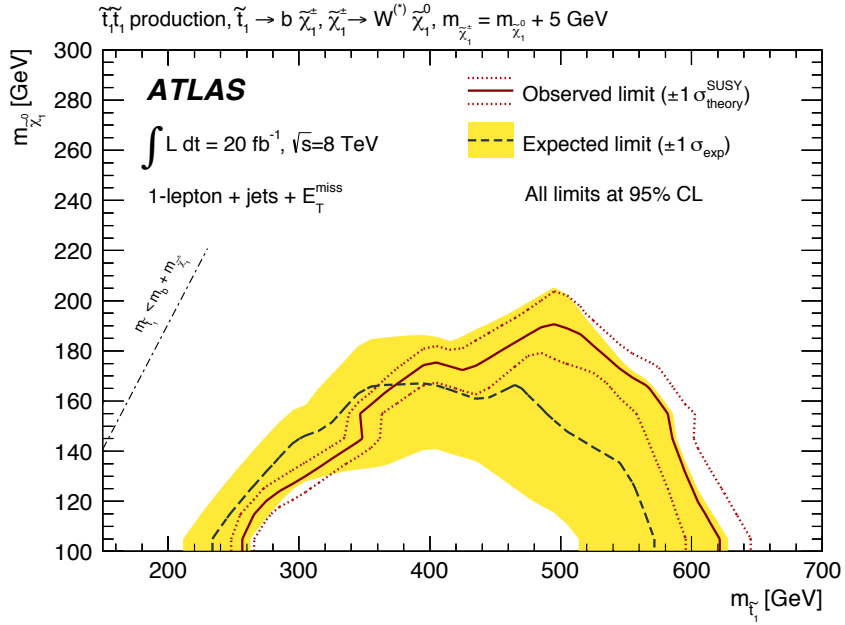


Figure 19. Expected (black dashed) and observed (red solid) 95% CL excluded region in the plane of $m_{\tilde{\chi}_1^0}$ vs. $m_{\tilde{t}_1}$, assuming $\mathcal{BR}(\tilde{t}_1 \rightarrow b\tilde{\chi}_1^\pm) = 100\%$, $\mathcal{BR}(\tilde{\chi}_1^\pm \rightarrow W^*\tilde{\chi}_1^0) = 100\%$ and $m_{\tilde{\chi}_1^\pm} = m_{\tilde{\chi}_1^0} + 5$ GeV.

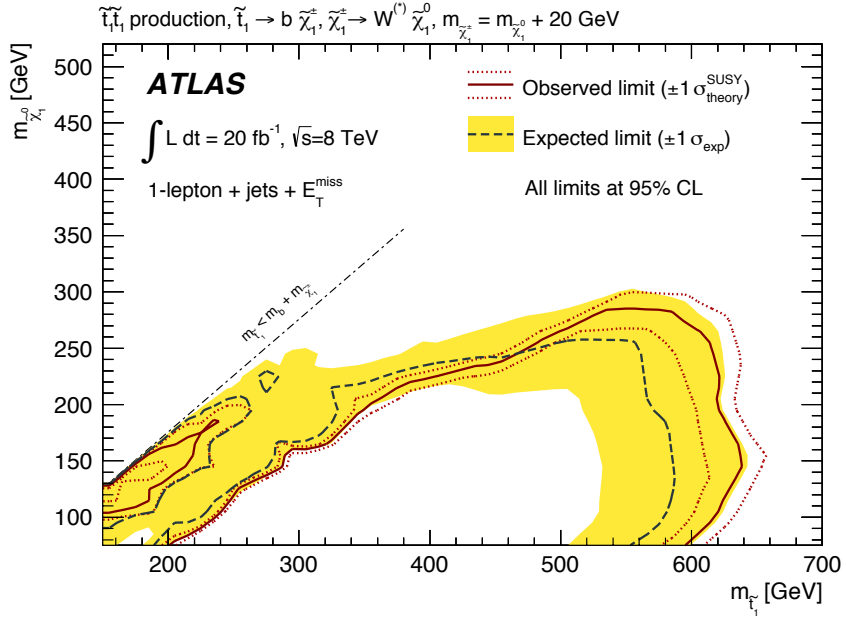


Figure 20. Expected (black dashed) and observed (red solid) 95% CL excluded region in the plane of $m_{\tilde{\chi}_1^0}$ vs. $m_{\tilde{t}_1}$, assuming $\mathcal{BR}(\tilde{t}_1 \rightarrow b\tilde{\chi}_1^\pm) = 100\%$, $\mathcal{BR}(\tilde{\chi}_1^\pm \rightarrow W^*\tilde{\chi}_1^0) = 100\%$ and $m_{\tilde{\chi}_1^\pm} = m_{\tilde{\chi}_1^0} + 20 \text{ GeV}$.

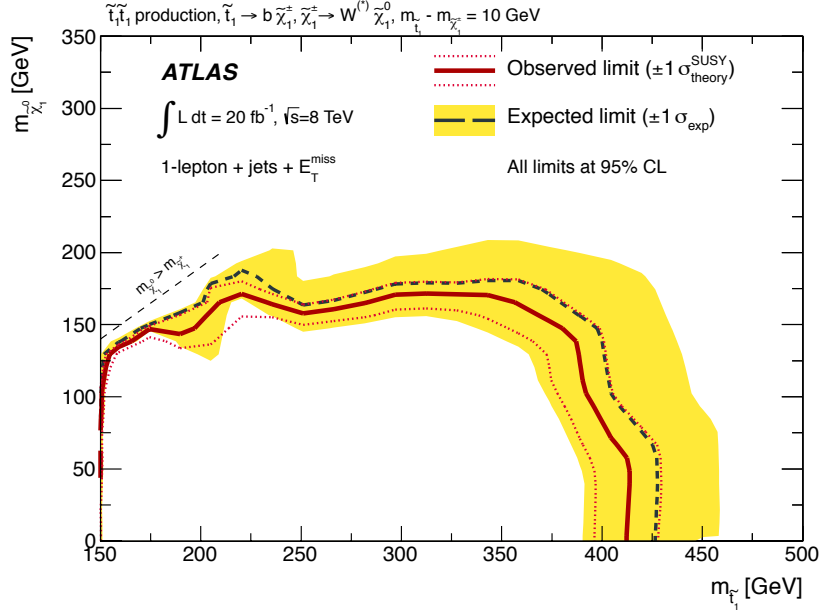


Figure 21. Expected (black dashed) and observed (red solid) 95% CL excluded region in the plane of $m_{\tilde{\chi}_1^0}$ vs. $m_{\tilde{t}_1}$, assuming $\mathcal{BR}(\tilde{t}_1 \rightarrow b\tilde{\chi}_1^\pm) = 100\%$, $\mathcal{BR}(\tilde{\chi}_1^\pm \rightarrow W^{(*)}\tilde{\chi}_1^0) = 100\%$ and $m_{\tilde{\chi}_1^\pm} = m_{\tilde{t}_1} - 10 \text{ GeV}$.

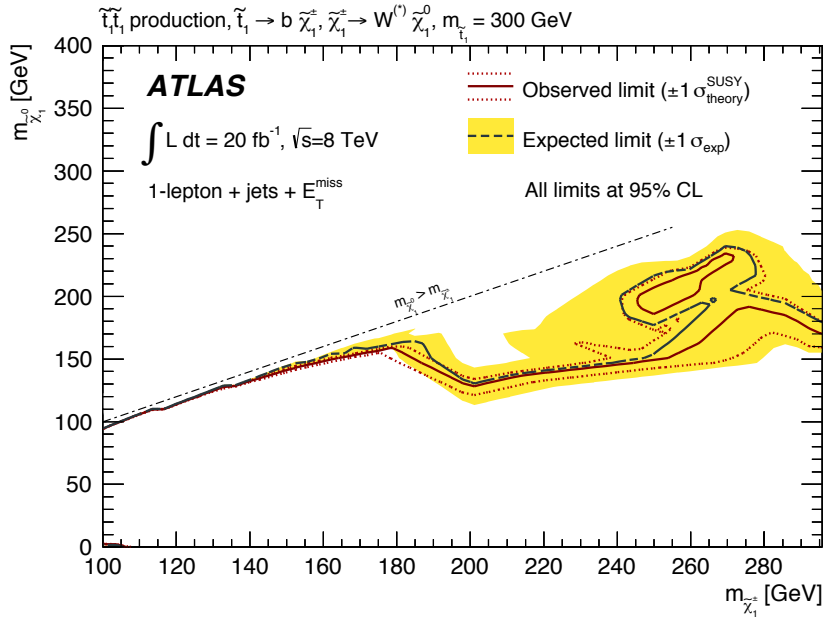


Figure 22. Expected (black dashed) and observed (red solid) 95% CL excluded region in the plane of $m_{\tilde{\chi}_1^0}$ vs. $m_{\tilde{\chi}_1^\pm}$, assuming $\mathcal{BR}(\tilde{t}_1 \rightarrow b\tilde{\chi}_1^\pm) = 100\%$, $\mathcal{BR}(\tilde{\chi}_1^\pm \rightarrow W^{(*)}\tilde{\chi}_1^0) = 100\%$ and $m_{\tilde{t}_1} = 300$ GeV.

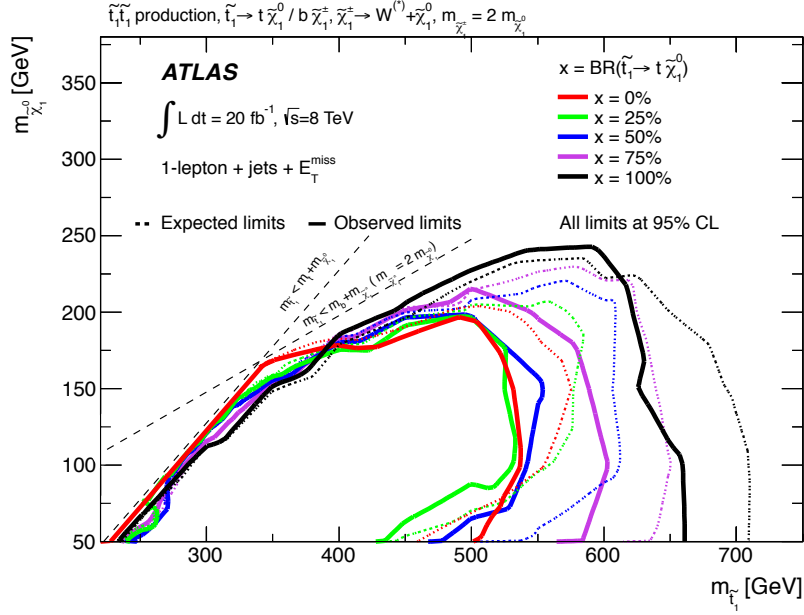


Figure 23. Expected (dashed) and observed (solid) 95% CL excluded region in the plane of $m_{\tilde{\chi}_1^0}$ vs. $m_{\tilde{t}_1}$, assuming $x = \mathcal{BR}(\tilde{t}_1 \rightarrow t\tilde{\chi}_1^0) = 1 - \mathcal{BR}(\tilde{t}_1 \rightarrow b\tilde{\chi}_1^\pm)$, and x varying from 0% to 100%.

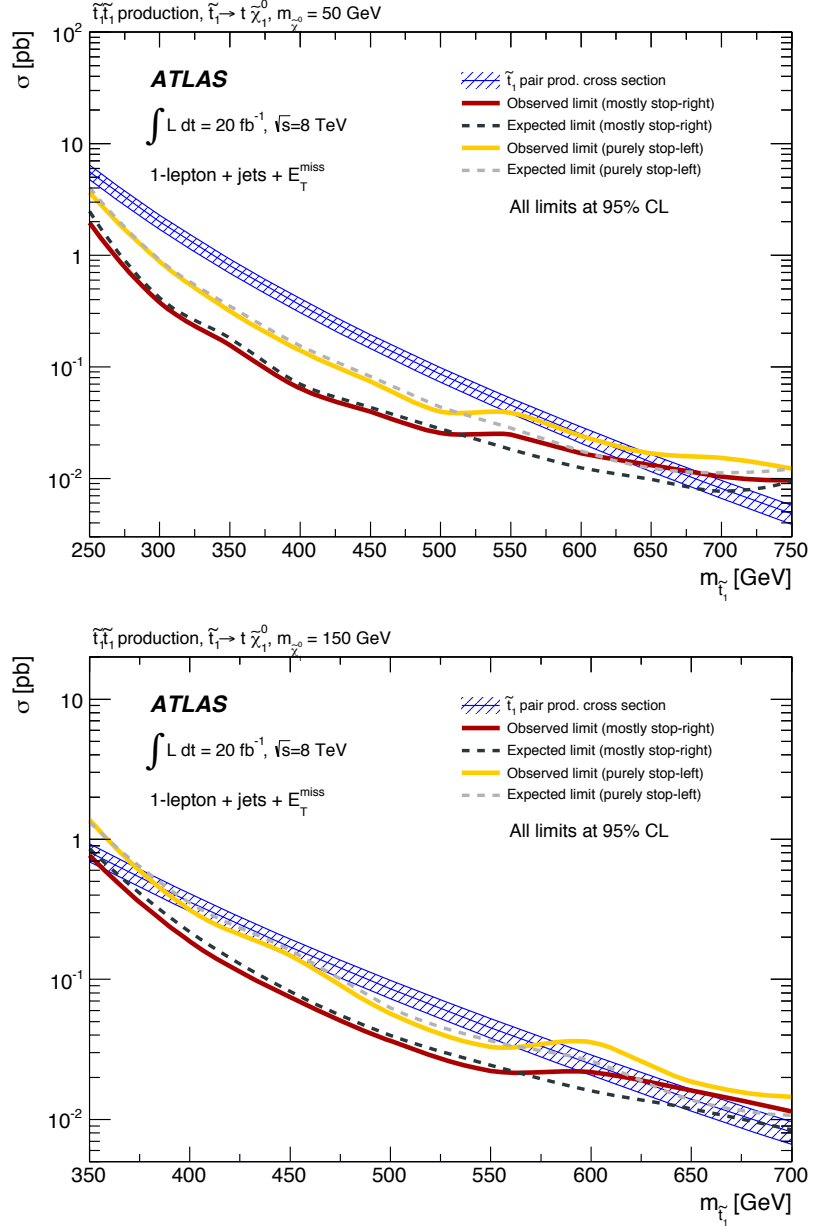


Figure 24. Expected and observed cross-section upper limits at 95% CL in the $\tilde{t}_1 \rightarrow t \tilde{\chi}_1^0$ decay mode with the LSP mass fixed to 50 GeV (top) or 150 GeV (bottom) for models with the \tilde{t}_1 being a pure stop-left (\tilde{t}_L) or mostly a stop-right (\tilde{t}_R). The upper and lower blue lines correspond to the nominal signal cross-section scaled up and down by the theoretical uncertainty.

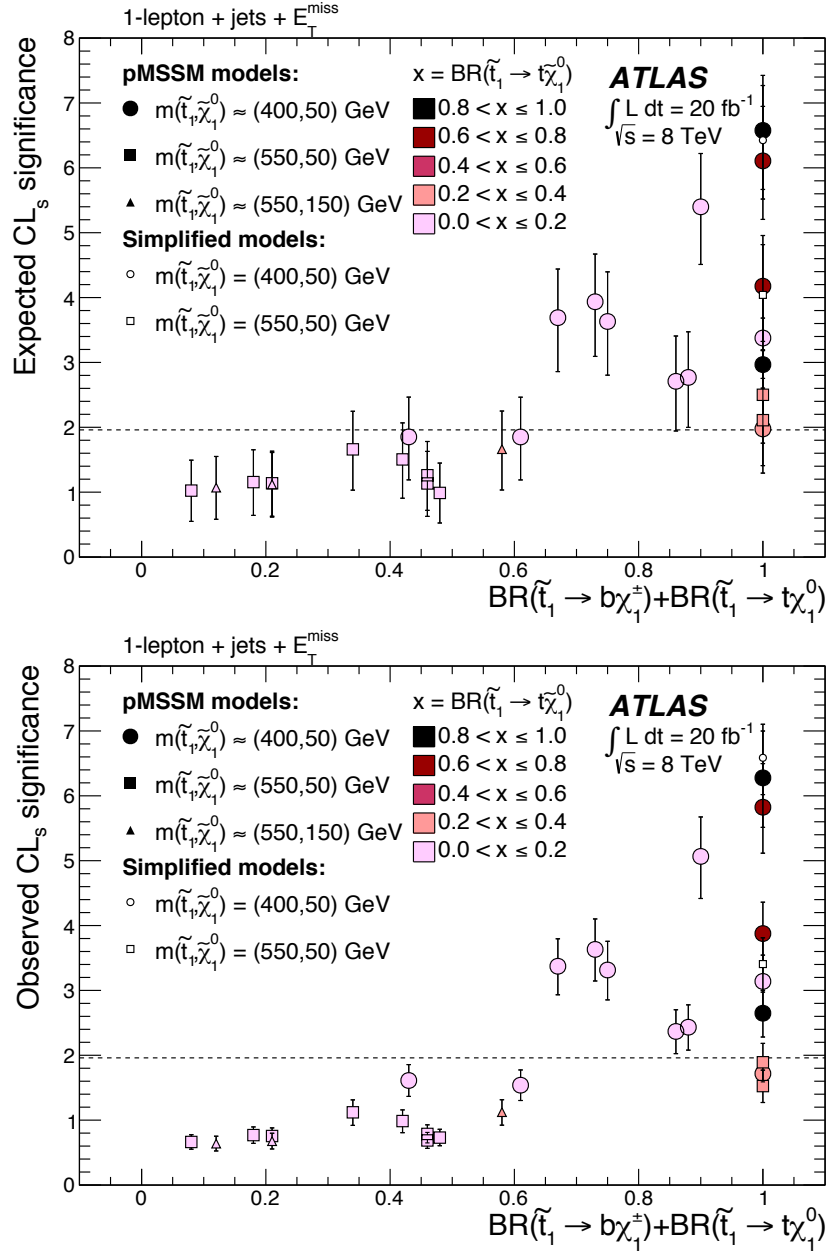


Figure 25. The expected (top) and observed (bottom) CL_s significance values for the 27 pMSSM models described in section 5.2 and for two simplified models. Models above the dashed line, indicating the CL_s significance corresponding to 95% CL, are excluded. The results of the pMSSM models are displayed using filled markers where the marker symbol corresponds to the $m_{\tilde{t}_1}$, $m_{\tilde{\chi}_1^0}$ range and the colour represents the branching ratio for the $\tilde{t}_1 \rightarrow t\tilde{\chi}_1^0$ decay, while the simplified models are shown using open markers. The uncertainty on the expected CL_s significance includes all sources except the theoretical cross-section uncertainty, while the uncertainty on the observed CL_s significance includes only the effect of scaling the nominal signal cross-section up and down by the theoretical cross-section uncertainty.

References

- [1] S. Weinberg, *Implications of Dynamical Symmetry Breaking*, *Phys. Rev.* **D 13** (1976) 974.
- [2] E. Gildener, *Gauge Symmetry Hierarchies*, *Phys. Rev.* **D 14** (1976) 1667.
- [3] S. Weinberg, *Implications of Dynamical Symmetry Breaking: An Addendum*, *Phys. Rev.* **D 19** (1979) 1277.
- [4] L. Susskind, *Dynamics of Spontaneous Symmetry Breaking in the Weinberg-Salam Theory*, *Phys. Rev.* **D 20** (1979) 2619.
- [5] ATLAS Collaboration, *Observation of a new particle in the search for the Standard Model Higgs boson with the ATLAS detector at the LHC*, *Phys. Lett.* **B 716** (2012) 1, [[arXiv:1207.7214](#)].
- [6] CMS Collaboration, *Observation of a new boson at a mass of 125 GeV with the CMS experiment at the LHC*, *Phys. Lett.* **B 716** (2012) 30, [[arXiv:1207.7235](#)].
- [7] L. Evans and P. Bryant, *LHC Machine*, *JINST* **3** (2008) S08001.
- [8] H. Miyazawa, *Baryon Number Changing Currents*, *Prog. Theor. Phys.* **36 (6)** (1966) 1266.
- [9] R. Ramond, *Dual Theory for Free Fermions*, *Phys. Rev.* **D 3** (1971) 2415.
- [10] Y. Golfand and E. Likhtman, *Extension of the Algebra of Poincare Group Generators and Violation of p Invariance*, *JETP Lett.* **13** (1971) 323.
- [11] A. Neveu and J. Schwarz, *Factorizable dual model of pions*, *Nucl. Phys.* **B 31** (1971) 86.
- [12] A. Neveu and J. Schwarz, *Quark Model of Dual Pions*, *Phys. Rev.* **D 4** (1971) 1109.
- [13] J. Gervais and B. Sakita, *Field theory interpretation of supergauges in dual models*, *Nucl. Phys.* **B 34** (1971) 632.
- [14] D. Volkov and V. Akulov, *Is the Neutrino a Goldstone Particle?*, *Phys. Lett.* **B 46** (1973) 109.
- [15] J. Wess and B. Zumino, *A Lagrangian Model Invariant Under Supergauge Transformations*, *Phys. Lett.* **B 49** (1974) 52.
- [16] J. Wess and B. Zumino, *Supergauge Transformations in Four-Dimensions*, *Nucl. Phys.* **B 70** (1974) 39.
- [17] S. Dimopoulos and H. Georgi, *Softly Broken Supersymmetry and SU(5)*, *Nucl. Phys.* **B 193** (1981) 150.
- [18] E. Witten, *Dynamical Breaking of Supersymmetry*, *Nucl. Phys.* **B188** (1981) 513.
- [19] M. Dine, W. Fischler, and M. Srednicki, *Supersymmetric Technicolor*, *Nucl. Phys.* **B189** (1981) 575–593.
- [20] S. Dimopoulos and S. Raby, *Supercolor*, *Nucl. Phys.* **B192** (1981) 353.
- [21] N. Sakai, *Naturalness in Supersymmetric Guts*, *Zeit. Phys.* **C11** (1981) 153.
- [22] R. Kaul and P. Majumdar, *Cancellation of Quadratically Divergent Mass Corrections in Globally Supersymmetric Spontaneously Broken Gauge Theories*, *Nucl. Phys.* **B199** (1982) 36.
- [23] R. Barbieri and G. Giudice, *Upper Bounds on Supersymmetric Particle Masses*, *Nucl.Phys.* **B 306** (1988) 63.

- [24] B. de Carlos and J. Casas, *One loop analysis of the electroweak breaking in supersymmetric models and the fine tuning problem*, *Phys. Lett. B* **309** (1993) 320.
- [25] **Super-Kamiokande** Collaboration, C. Regis et al., *Search for Proton Decay via $p \rightarrow \mu^+ K^0$ in Super-Kamiokande I, II, and III*, *Phys. Rev. D* **86** (2012) 012006, [[arXiv:1205.6538](#)].
- [26] P. Fayet, *Supersymmetry and Weak, Electromagnetic and Strong Interactions*, *Phys. Lett. B* **64** (1976) 159.
- [27] P. Fayet, *Spontaneously Broken Supersymmetric Theories of Weak, Electromagnetic and Strong Interactions*, *Phys. Lett. B* **69** (1977) 489.
- [28] G. R. Farrar and P. Fayet, *Phenomenology of the Production, Decay, and Detection of New Hadronic States Associated with Supersymmetry*, *Phys. Lett. B* **76** (1978) 575.
- [29] P. Fayet, *Relations Between the Masses of the Superpartners of Leptons and Quarks, the Goldstino Couplings and the Neutral Currents*, *Phys. Lett. B* **84** (1979) 416.
- [30] LEP SUSY Working Group, ALEPH, DELPHI, L3 and OPAL experiments. [LEPSUSYWG/01-03.1](#).
- [31] **MSSM Working Group** Collaboration, A. Djouadi et al., *The Minimal supersymmetric standard model: Group summary report*, [hep-ph/9901246](#).
- [32] **ATLAS** Collaboration, *Search for a supersymmetric partner to the top quark in final states with jets and missing transverse momentum at $\sqrt{s} = 7$ TeV with the ATLAS detector*, *Phys. Rev. Lett.* **109** (2012) 211802, [[arXiv:1208.1447](#)].
- [33] **ATLAS** Collaboration, *Search for direct top squark pair production in final states with one isolated lepton, jets, and missing transverse momentum in $\sqrt{s} = 7$ TeV pp collisions using 4.7 fb^{-1} of ATLAS data*, *Phys. Rev. Lett.* **109** (2012) 211803, [[arXiv:1208.2590](#)].
- [34] **ATLAS** Collaboration, *Search for light scalar top quark pair production in final states with two leptons with the ATLAS detector in $\sqrt{s} = 7$ TeV proton-proton collisions*, *Eur. Phys. J. C* **72** (2012) 2237, [[arXiv:1208.4305](#)].
- [35] **ATLAS** Collaboration, *Search for light top squark pair production in final states with leptons and b-jets with the ATLAS detector in $\sqrt{s} = 7$ TeV proton-proton collisions*, *Phys. Lett. B* **720** (2013) 13, [[arXiv:1209.2102](#)].
- [36] **ATLAS** Collaboration, *Search for a heavy top-quark partner in final states with two leptons with the ATLAS detector at the LHC*, *JHEP* **11** (2012) 094, [[arXiv:1209.4186](#)].
- [37] **ATLAS** Collaboration, *Search for direct third-generation squark pair production in final states with missing transverse momentum and two b-jets in $\sqrt{s} = 8$ TeV pp collisions with the ATLAS detector*, *JHEP* **10** (2013) 189, [[arXiv:1308.2631](#)].
- [38] **ATLAS** Collaboration, *Search for direct top-squark pair production in final states with two leptons in pp collisions at $\sqrt{s}=8$ TeV with the ATLAS detector*, [arXiv:1403.4853](#).
- [39] **CMS** Collaboration, *Inclusive search for supersymmetry using the razor variables in pp collisions at $\sqrt{s} = 7$ TeV*, *Phys. Rev. Lett.* **111** (2013) 081802, [[arXiv:1212.6961](#)].
- [40] **CMS** Collaboration, *Search for supersymmetry in hadronic final states with missing transverse energy using the variables α_T and b-quark multiplicity in pp collisions at 8 TeV*, *Eur. Phys. J. C* **73** (2013) 2568, [[arXiv:1303.2985](#)].

- [41] CMS Collaboration, *Search for top-squark pair production in the single-lepton final state in pp collisions at $\sqrt{s} = 8$ TeV*, *Eur. Phys. J. C* **73** (2013) 2677, [[arXiv:1308.1586](#)].
- [42] CMS Collaboration, *Search for top squark and higgsino production using diphoton Higgs boson decays*, *Phys.Rev.Lett.* **112** (2014) 161802, [[arXiv:1312.3310](#)].
- [43] CMS Collaboration, *Search for top-squark pairs decaying into Higgs or Z bosons in pp collisions at $\sqrt{s} = 8$ TeV*, [arXiv:1405.3886](#).
- [44] CDF Collaboration, T. Aaltonen et al., *Search for Pair Production of Supersymmetric Top Quarks in Dilepton Events from p anti-p Collisions at $\sqrt{s} = 1.96$ TeV*, *Phys.Rev.Lett.* **104** (2010) 251801, [[arXiv:0912.1308](#)].
- [45] D0 Collaboration, V. Abazov et al., *Search for the lightest scalar top quark in events with two leptons in $p\bar{p}$ collisions at $\sqrt{s} = 1.96$ TeV*, *Phys.Lett.* **B675** (2009) 289–296, [[arXiv:0811.0459](#)].
- [46] LEP SUSY Working Group, ALEPH, DELPHI, L3 and OPAL experiments. [LEPSUSYWG/04-02.1](#).
- [47] ATLAS Collaboration, *Search for supersymmetry in pp collisions at $\sqrt{s} = 7$ TeV in final states with missing transverse momentum and b-jets with the ATLAS detector*, *Phys. Rev. D* **85** (2012) 112006, [[arXiv:1203.6193](#)].
- [48] ATLAS Collaboration, *Search for top and bottom squarks from gluino pair production in final states with missing transverse energy and at least three b-jets with the ATLAS detector*, *Eur. Phys. J. C* **72** (2012) 2174, [[arXiv:1207.4686](#)].
- [49] ATLAS Collaboration, *Search for new phenomena in final states with large jet multiplicities and missing transverse momentum at $\sqrt{s} = 8$ TeV proton-proton collisions using the ATLAS experiment*, *JHEP* **10** (2013) 130, [[arXiv:1308.1841](#)].
- [50] ATLAS Collaboration, *Search for supersymmetry at $\sqrt{s}=8$ TeV in final states with jets and two same-sign leptons or three leptons with the ATLAS detector*, *JHEP* **1406** (2014) 035, [[arXiv:1404.2500](#)].
- [51] CMS Collaboration, *Search for supersymmetry in hadronic final states using MT2 in pp collisions at $\sqrt{s} = 7$ TeV*, [arXiv:1207.1798](#).
- [52] CMS Collaboration, *Search for gluino mediated bottom- and top-squark production in multijet final states in pp collisions at 8 TeV*, *Phys. Lett. B* **725** (2013) 243, [[arXiv:1305.2390](#)].
- [53] CMS Collaboration, *Search for supersymmetry in pp collisions at $\sqrt{s} = 8$ TeV in events with a single lepton, large jet multiplicity, and multiple b jets*, [arXiv:1311.4937](#).
- [54] CMS Collaboration, *Search for new physics in events with same-sign dileptons and jets in pp collisions at $\sqrt{s} = 8$ TeV*, *JHEP* **01** (2014) 163, [[arXiv:1311.6736](#)].
- [55] CMS Collaboration, *Search for new physics in the multijet and missing transverse momentum final state in proton-proton collisions at $\sqrt{s} = 8$ TeV*, [arXiv:1402.4770](#).
- [56] ATLAS Collaboration, *The ATLAS Experiment at the CERN Large Hadron Collider*, *JINST* **3** (2008) S08003.
- [57] ATLAS Collaboration, *Performance of the ATLAS Trigger System in 2010*, *Eur. Phys. J. C* **72** (2012) 1849, [[arXiv:1110.1530](#)].

- [58] ATLAS Collaboration, *Improved luminosity determination in pp collisions at $\sqrt{s} = 7$ TeV using the ATLAS detector at the LHC*, *Eur. Phys. J. C* **73** (2013) 2518, [[arXiv:1302.4393](#)].
- [59] S. Frixione, P. Nason, and C. Oleari, *Matching NLO QCD computations with parton shower simulations: the POWHEG method*, *JHEP* **11** (2007) 070, [[arXiv:0709.2092](#)].
- [60] B. P. Kersevan and E. Richter-Was, *The Monte Carlo event generator AcerMC versions 2.0 to 3.8 with interfaces to PYTHIA 6.4, HERWIG 6.5 and ARIADNE 4.1*, *Comput.Phys.Commun.* **184** (2013) 919, [[hep-ph/0405247](#)].
- [61] J. Alwall et al., *MadGraph 5 : Going Beyond*, *JHEP* **06** (2011) 128, [[arXiv:1106.0522](#)].
- [62] T. Gleisberg et al., *Event generation with SHERPA 1.1*, *JHEP* **02** (2009) 007, [[arXiv:0811.4622](#)].
- [63] M. Bahr et al., *Herwig++ Physics and Manual*, *Eur. Phys. J. C* **58** (2008) 639, [[arXiv:0803.0883](#)].
- [64] H.-L. Lai et al., *New parton distributions for collider physics*, *Phys. Rev. D* **82** (2010) 074024, [[arXiv:1007.2241](#)].
- [65] J. Pumplin et al., *New generation of parton distributions with uncertainties from global QCD analysis*, *JHEP* **07** (2002) 012, [[hep-ph/0201195](#)].
- [66] ATLAS Collaboration, *New ATLAS event generator tunes to 2010 data*, *ATL-PHYS-PUB-2011-008*, (2011).
- [67] P. Z. Skands, *Tuning Monte Carlo Generators: The Perugia Tunes*, *Phys. Rev. D* **82** (2010) 074018, [[arXiv:1005.3457](#)].
- [68] S. Gieseke, C. Rohr, and A. Siodmok, *Colour reconnections in Herwig++*, *Eur. Phys. J. C* **72** (2012) 2225, [[arXiv:1206.0041](#)].
- [69] T. Sjostrand, S. Mrenna, and P. Z. Skands, *PYTHIA 6.4 Physics and Manual*, *JHEP* **05** (2006) 026, [[hep-ph/0603175](#)].
- [70] ATLAS Collaboration, *The ATLAS Simulation Infrastructure*, *Eur. Phys. J. C* **70** (2010) 823, [[arXiv:1005.4568](#)].
- [71] GEANT4 Collaboration, S. Agostinelli et al., *GEANT4: A simulation toolkit*, *Nucl. Instrum. Meth. A* **506** (2003) 250.
- [72] ATLAS Collaboration, *The simulation principle and performance of the ATLAS fast calorimeter simulation FastCaloSim*, *ATL-PHYS-PUB-2010-013*, (2010).
- [73] T. Sjostrand, S. Mrenna, and P. Z. Skands, *A Brief Introduction to PYTHIA 8.1*, *Comput. Phys. Commun.* **178** (2008) 852, [[arXiv:0710.3820](#)].
- [74] ATLAS Collaboration, *Measurement of top quark pair differential cross-sections in the $t+jets$ channel in pp collisions at $\sqrt{s} = 7$ TeV using the ATLAS detector*, *ATLAS-CONF-2013-099*, (2013).
- [75] S. Frixione et al., *Single-top hadroproduction in association with a W boson*, *JHEP* **07** (2008) 029, [[arXiv:0805.3067](#)].
- [76] M. Czakon, P. Fiedler, and A. Mitov, *The total top quark pair production cross-section at hadron colliders through $O(\alpha_S^4)$* , [arXiv:1303.6254](#).
- [77] M. Czakon and A. Mitov, *NNLO corrections to top pair production at hadron colliders: the quark-gluon reaction*, *JHEP* **01** (2013) 080, [[arXiv:1210.6832](#)].

- [78] M. Czakon and A. Mitov, *NNLO corrections to top-pair production at hadron colliders: the all-fermionic scattering channels*, *JHEP* **12** (2012) 054, [[arXiv:1207.0236](#)].
- [79] P. Baernreuther, M. Czakon, and A. Mitov, *Percent Level Precision Physics at the Tevatron: First Genuine NNLO QCD Corrections to $q\bar{q} \rightarrow t\bar{t} + X$* , *Phys. Rev. Lett.* **109** (2012) 132001, [[arXiv:1204.5201](#)].
- [80] M. Cacciari et al., *Top-pair production at hadron colliders with next-to-next-to-leading logarithmic soft-gluon resummation*, *Phys. Lett. B* **710** (2012) 612, [[arXiv:1111.5869](#)].
- [81] M. Czakon and A. Mitov, *Top++: A Program for the Calculation of the Top-Pair Cross-Section at Hadron Colliders*, [arXiv:1112.5675](#).
- [82] N. Kidonakis, *Next-to-next-to-leading-order collinear and soft gluon corrections for t-channel single top quark production*, *Phys. Rev. D* **83** (2011) 091503, [[arXiv:1103.2792](#)].
- [83] N. Kidonakis, *Two-loop soft anomalous dimensions for single top quark associated production with a W- or H-*, *Phys. Rev. D* **82** (2010) 054018, [[arXiv:1005.4451](#)].
- [84] N. Kidonakis, *NNLL resummation for s-channel single top quark production*, *Phys. Rev. D* **81** (2010) 054028, [[arXiv:1001.5034](#)].
- [85] J. M. Campbell and R. K. Ellis, *$t\bar{t}W^\pm$ production and decay at NLO*, *JHEP* **07** (2012) 052, [[arXiv:1204.5678](#)].
- [86] M. Garzelli et al., *$t\bar{t}W^\pm$ and $t\bar{t}Z$ Hadroproduction at NLO accuracy in QCD with Parton Shower and Hadronization effects*, *JHEP* **11** (2012) 056, [[arXiv:1208.2665](#)].
- [87] J. Campbell, R. K. Ellis, and R. Rontsch, *Single top production in association with a Z boson at the LHC*, *Phys. Rev. D* **87** (2013) 114006, [[arXiv:1302.3856](#)].
- [88] S. Catani et al., *Vector boson production at hadron colliders: a fully exclusive QCD calculation at NNLO*, *Phys. Rev. Lett.* **103** (2009) 082001, [[arXiv:0903.2120](#)].
- [89] J. M. Campbell and R. K. Ellis, *An Update on vector boson pair production at hadron colliders*, *Phys. Rev. D* **60** (1999) 113006, [[hep-ph/9905386](#)].
- [90] J. M. Campbell, R. K. Ellis, and C. Williams, *Vector boson pair production at the LHC*, *JHEP* **07** (2011) 018, [[arXiv:1105.0020](#)].
- [91] A. D. Martin et al., *Parton distributions for the LHC*, *Eur. Phys. J. C* **63** (2009) 189, [[arXiv:0901.0002](#)].
- [92] P. M. Nadolsky et al., *Implications of CTEQ global analysis for collider observables*, *Phys. Rev. D* **78** (2008) 013004, [[arXiv:0802.0007](#)].
- [93] W. Beenakker et al., *Stop production at hadron colliders*, *Nucl. Phys. B* **515** (1998) 3, [[hep-ph/9710451](#)].
- [94] W. Beenakker et al., *Supersymmetric top and bottom squark production at hadron colliders*, *JHEP* **08** (2010) 098, [[arXiv:1006.4771](#)].
- [95] W. Beenakker et al., *Squark and gluino hadroproduction*, *Int. J. Mod. Phys. A* **26** (2011) 2637, [[arXiv:1105.1110](#)].
- [96] M. Kramer et al., *Supersymmetry production cross sections in pp collisions at $\sqrt{s} = 7$ TeV*, [arXiv:1206.2892](#).
- [97] M. Cahill-Rowley et al., *pMSSM Studies at the 7, 8 and 14 TeV LHC*, [arXiv:1307.8444](#).

- [98] **WMAP** Collaboration, G. Hinshaw et al., *Nine-Year Wilkinson Microwave Anisotropy Probe (WMAP) Observations: Cosmological Parameter Results*, *Astrophys.J.Suppl.* **208** (2013) 19, [[arXiv:1212.5226](#)].
- [99] J. R. Ellis et al., *Observables in Low-Energy Superstring Models*, *Mod.Phys. Lett. A* **1** (1986) 57.
- [100] **ATLAS** Collaboration, *Performance of primary vertex reconstruction in proton-proton collisions at $\sqrt{s} = 7$ TeV in the ATLAS experiment*, [ATLAS-CONF-2010-069](#), (2010).
- [101] W. Lampl et al., *Calorimeter Clustering Algorithms: Description and Performance*, [ATL-LARG-PUB-2008-002](#), (2008).
- [102] M. Cacciari, G. P. Salam, and G. Soyez, *The anti- k_t jet clustering algorithm*, *JHEP* **04** (2008) 063, [[arXiv:0802.1189](#)].
- [103] M. Cacciari and G. P. Salam, *Dispelling the N^3 myth for the k_t jet-finder*, *Phys. Lett. B* **641** (2006) 57, [[hep-ph/0512210](#)].
- [104] M. Cacciari, G. P. Salam, and G. Soyez, *The Catchment Area of Jets*, *JHEP* **04** (2008) 005, [[arXiv:0802.1188](#)].
- [105] **ATLAS** Collaboration, *Jet energy measurement with the ATLAS detector in proton-proton collisions at $\sqrt{s} = 7$ TeV*, *Eur. Phys. J. C* **73** (2013) 2304, [[arXiv:1112.6426](#)].
- [106] **ATLAS** Collaboration, *Jet energy measurement and its systematic uncertainty in proton-proton collisions at $\sqrt{s} = 7$ TeV with the ATLAS detector*, [arXiv:1406.0076](#).
- [107] **ATLAS** Collaboration, *Performance of jet substructure techniques for large- R jets in proton-proton collisions at $\sqrt{s} = 7$ TeV using the ATLAS detector*, *JHEP* **1309** (2013) 076, [[arXiv:1306.4945](#)].
- [108] D. Krohn, J. Thaler, and L.-T. Wang, *Jet Trimming*, *JHEP* **02** (2010) 084, [[arXiv:0912.1342](#)].
- [109] **ATLAS** Collaboration, *Commissioning of the ATLAS high-performance b-tagging algorithms in the 7 TeV collision data*, [ATLAS-CONF-2011-102](#), (2011).
- [110] **ATLAS** Collaboration, *Calibrating the b-Tag Efficiency and Mistag Rate in 35 pb^{-1} of Data with the ATLAS Detector*, [ATLAS-CONF-2011-089](#), (2011).
- [111] **ATLAS** Collaboration, *Measurement of the Mistag Rate with 5 fb^{-1} of Data Collected by the ATLAS Detector*, [ATLAS-CONF-2012-040](#), (2012).
- [112] **ATLAS** Collaboration, *Electron performance measurements with the ATLAS detector using the 2010 LHC proton-proton collision data*, *Eur. Phys. J. C* **72** (2012) 1909, [[arXiv:1110.3174](#)].
- [113] **ATLAS** Collaboration, *Electron reconstruction and identification efficiency measurements with the ATLAS detector using the 2011 LHC proton-proton collision data*, *Eur. Phys. J. C* **74** (2014) 2941, [[arXiv:1404.2240](#)].
- [114] **ATLAS** Collaboration, *Electron efficiency measurements with the ATLAS detector using the 2012 LHC proton-proton collision data*, [ATLAS-CONF-2014-032](#), (2014).
- [115] **ATLAS** Collaboration, *Muon reconstruction efficiency in reprocessed 2010 LHC proton-proton collision data recorded with the ATLAS detector*, [ATLAS-CONF-2011-063](#), (2011).

- [116] **ATLAS** Collaboration, *Preliminary results on the muon reconstruction efficiency, momentum resolution, and momentum scale in ATLAS 2012 pp collision data*, [ATLAS-CONF-2013-088](#), (2013).
- [117] **ATLAS** Collaboration, *Muon reconstruction efficiency and momentum resolution of the ATLAS experiment in proton-proton collisions at $\sqrt{s}=7$ TeV in 2010*, [arXiv:1404.4562](#).
- [118] **ATLAS** Collaboration, *Measurements of the photon identification efficiency with the ATLAS detector using 4.9 fb^{-1} of pp collision data collected in 2011*, [ATLAS-CONF-2012-123](#), (2012).
- [119] **ATLAS** Collaboration, *Measurement of the inclusive isolated prompt photon cross section in pp collisions at $\sqrt{s} = 7$ TeV with the ATLAS detector*, *Phys. Rev. D* **83** (2011) 052005, [[arXiv:1012.4389](#)].
- [120] **ATLAS** Collaboration, *Performance of the reconstruction and identification of hadronic tau decays with ATLAS*, [ATLAS-CONF-2011-152](#), (2011).
- [121] **ATLAS** Collaboration, *Performance of the reconstruction and identification of hadronic tau decays in ATLAS with 2011 data*, [ATLAS-CONF-2012-142](#), (2012).
- [122] **ATLAS** Collaboration, *Performance of Missing Transverse Momentum Reconstruction in Proton-Proton Collisions at 7 TeV with ATLAS*, *Eur. Phys. J. C* **72** (2012) 1844, [[arXiv:1108.5602](#)].
- [123] **ATLAS** Collaboration, *Performance of Missing Transverse Momentum Reconstruction in ATLAS studied in Proton-Proton Collisions recorded in 2012 at 8 TeV*, [ATLAS-CONF-2013-082](#), (2013).
- [124] C. Lester and D. Summers, *Measuring masses of semi-invisibly decaying particles pair produced at hadron colliders*, *Phys. Lett. B* **463** (1999) 99, [[hep-ph/9906349](#)].
- [125] Y. Bai et al., *Stop the Top Background of the Stop Search*, *JHEP* **07** (2012) 110, [[arXiv:1203.4813](#)].
- [126] A. J. Barr, B. Gripaios, and C. G. Lester, *Transverse masses and kinematic constraints: from the boundary to the crease*, *JHEP* **11** (2009) 096, [[arXiv:0908.3779](#)].
- [127] P. Konar et al., *Dark Matter Particle Spectroscopy at the LHC: Generalizing MT2 to Asymmetric Event Topologies*, *JHEP* **04** (2010) 086, [[arXiv:0911.4126](#)].
- [128] M. L. Graesser and J. Shelton, *Hunting Asymmetric Stops*, *Phys. Rev. Lett.* **111** (2013) 121802, [[arXiv:1212.4495](#)].
- [129] **ATLAS** Collaboration, *Jet energy resolution in proton-proton collisions at $\sqrt{s} = 7$ TeV recorded in 2010 with the ATLAS detector*, *Eur. Phys. J. C* **73** (2013) 2306, [[arXiv:1210.6210](#)].
- [130] **ATLAS** Collaboration, *Further search for supersymmetry at $\sqrt{s} = 7$ TeV in final states with jets, missing transverse momentum and isolated leptons with the ATLAS detector*, *Phys. Rev. D* **86** (2012) 092002, [[arXiv:1208.4688](#)].
- [131] **ATLAS** Collaboration, *Search for supersymmetry in final states with jets, missing transverse momentum and one isolated lepton in $\sqrt{s} = 7$ TeV pp collisions using 1 fb^{-1} of ATLAS data*, *Phys. Rev. D* **85** (2012) 012006, [[arXiv:1109.6606](#)].
- [132] K. Melnikov, M. Schulze, and A. Scharf, *QCD corrections to top quark pair production in*

- association with a photon at hadron colliders, Phys. Rev. **D** **83** (2011) 074013, [[arXiv:1102.1967](#)].*
- [133] **ATLAS** Collaboration, *Jet mass and substructure of inclusive jets in $\sqrt{s} = 7$ TeV pp collisions with the ATLAS experiment, JHEP **05** (2012) 128, [[arXiv:1203.4606](#)].*
- [134] **ATLAS** Collaboration, *Calibration of b-tagging using dileptonic top pair events in a combinatorial likelihood approach with the ATLAS experiment, ATLAS-CONF-2014-004*, (2014).
- [135] **ATLAS** Collaboration, *Measurement of the b-tag Efficiency in a Sample of Jets Containing Muons with 5 fb^{-1} of Data from the ATLAS Detector, ATLAS-CONF-2012-043*, (2012).
- [136] **ATLAS** Collaboration, *b-jet tagging calibration on c-jets containing D^{*+} mesons, ATLAS-CONF-2012-039*, (2012).
- [137] M. Botje et al., *The PDF4LHC Working Group Interim Recommendations*, [arXiv:1101.0538](#).
- [138] R. D. Ball et al., *Parton distributions with LHC data, Nucl.Phys. **B867** (2013) 244–289, [[arXiv:1207.1303](#)].*
- [139] J. M. Butterworth, J. R. Forshaw, and M. H. Seymour, *Multiparton interactions in photoproduction at HERA, Z. Phys. **C** **72** (1996) 637*, [[hep-ph/9601371](#)].
- [140] **ATLAS** Collaboration, *Measurement of $t\bar{t}$ production with a veto on additional central jet activity in pp collisions at $\sqrt{s} = 7$ TeV using the ATLAS detector, Eur. Phys. J. **C** **72** (2012) 2043, [[arXiv:1203.5015](#)].*
- [141] **ATLAS** Collaboration, *Measurement of the cross-section for W boson production in association with b-jets in pp collisions at $\sqrt{s} = 7$ TeV with the ATLAS detector, JHEP **06** (2013) 084, [[arXiv:1302.2929](#)].*
- [142] G. Cowan et al., *Asymptotic formulae for likelihood-based tests of new physics, Eur. Phys. J. **C71** (2011) 1554*, [[arXiv:1007.1727](#)].
- [143] A. L. Read, *Presentation of search results: The $CL(s)$ technique, J. Phys. **G** **28** (2002) 2693.*
- [144] **ALEPH** Collaboration, A. Heister et al., *Search for scalar quarks in e^+e^- collisions at \sqrt{s} up to 209 GeV, Phys. Lett. **B537** (2002) 5–20, [[hep-ex/0204036](#)].*
- [145] B. Nachman and C. G. Lester, *Significance Variables, Phys. Rev. **D** **88** (2013) 075013, [[arXiv:1303.7009](#)].*

A Detailed description of the discriminating variables

This section provides more detailed descriptions of the discriminating variables that are introduced in section 6.

- Transverse Mass, $m_{\text{T}2}$

This variable targets decay topologies with two branches, referred to here as a and b . In each branch, there are some particles with fully measured momenta and some particles with momenta that are not measured directly. The sum of the four vectors of the measured momenta in branch $i \in \{a, b\}$ are denoted $p_i = (E_i, \vec{p}_{\text{T}i}, p_{zi})$ and the sum of the four vectors of the unmeasured momenta are denoted $q_i = (F_i, \vec{q}_{\text{T}i}, q_{zi})$. With $m_{p_i}^2 = E_i^2 - \vec{p}_i^2$ and $m_{q_i}^2 = F_i^2 - \vec{q}_i^2$, the m_{T} of the particles in branch i is given in general by

$$m_{\text{T}i}^2 = \left(\sqrt{p_{\text{T}i}^2 + m_{p_i}^2} + \sqrt{q_{\text{T}i}^2 + m_{q_i}^2} \right)^2 - (\vec{p}_{\text{T}i} + \vec{q}_{\text{T}i})^2$$

which in the case that $m_{q_i} = m_{p_i} = 0$ is the same as the one given in section 6.2. A generalisation of m_{T} , $m_{\text{T}2}$, is defined as a minimisation over the allocation of $\vec{p}_{\text{T}}^{\text{miss}}$ between $\vec{q}_{\text{T}a}$ and $\vec{q}_{\text{T}b}$ of the maximum of the corresponding $m_{\text{T}a}$ or $m_{\text{T}b}$:

$$m_{\text{T}2} \equiv \min_{\vec{q}_{\text{T}a} + \vec{q}_{\text{T}b} = \vec{p}_{\text{T}}^{\text{miss}}} \{ \max(m_{\text{T}a}, m_{\text{T}b}) \},$$

where one must make an assumption of m_{q_a} and m_{q_b} in the computation of $m_{\text{T}a}$ and $m_{\text{T}b}$. The result of the above minimisation is the minimum parent mass consistent with the observed kinematic distributions under the inputs m_{q_a} and m_{q_b} . The variants of $m_{\text{T}2}$ described below only differ in the measured particles, (assumed) unmeasured particles, and choices for the input masses, m_{q_a} and m_{q_b} .

- Asymmetric $m_{\text{T}2}$, $am_{\text{T}2}$

- Measured particles: For branch a , this is one of the b -jets and for branch b this is the second b -jet and the charged lepton. The b -jets are identified based on the highest b -tagging weights. Since there are two ways of assigning the b -tagged jets to branches a and b , both $m_{\text{T}2}$ values are computed and the minimum kept for the final discriminant.
- Unmeasured particles: For branch a , this is a W boson that decays leptonically, with the charged lepton unidentified as such. The unmeasured particle for branch b is the neutrino associated with the measured charged lepton.
- Input masses: $m_{q_a} = m_W = 80 \text{ GeV}$ and $m_{q_b} = m_\nu = 0 \text{ GeV}$.
- In cases in which the lost lepton is an electron and the corresponding energy deposit enters the $E_{\text{T}}^{\text{miss}}$ calculation, for instance as a soft calorimeter cluster, $am_{\text{T}2}$ can exceed the top mass boundary in $t\bar{t}$ events, but the variable remains powerful at discriminating signal from background.

- τ -based m_{T2} , m_{T2}^τ
 - Measured particles: For branch a , this is the τ -jet, identified as the highest- p_T jet excluding the selected two b -tagged jets. The measured particle for branch b is the charged lepton.
 - Unmeasured particles: For branch a , this includes the two neutrinos associated with the τ production and hadronic decay. The unmeasured particle for branch b is the neutrino associated with the charged lepton.
 - Input masses: $m_{q_a} = 0 \text{ GeV}$ and $m_{q_b} = m_\nu = 0 \text{ GeV}$.

- Topness

The *topness* event value is defined as $\ln(\min \hat{S})$, where \hat{S} is the minimum of the χ^2 -type function S :

$$S(p_{W,x}, p_{W,y}, p_{W,z}, p_{\nu,z}) = \frac{\left(m_W^2 - (p_\ell + p_\nu)^2\right)^2}{a_W^4} + \frac{\left(m_t^2 - (p_{b_1} + p_\ell + p_\nu)^2\right)^2}{a_t^4} + \frac{\left(m_t^2 - (p_{b_2} + p_W)^2\right)^2}{a_t^4} + \frac{\left(4m_t^2 - (\Sigma p)^2\right)^2}{a_{\text{CM}}^4}.$$

The first three arguments of S are the components of the non-reconstructed W boson 3-momentum ($p_{W,x}$, $p_{W,y}$, $p_{W,z}$). This W is assumed to decay leptonically, but the lepton is not reconstructed and is thus only noticeable in the missing transverse momentum. The variable $p_{\nu,z}$ is the longitudinal momentum of the neutrino from the other W boson decay, for which the lepton was successfully reconstructed. These four numbers are varied to find the minimum of S .

The momenta appearing on the right-hand side of the equation above are either 4-momenta of the reconstructed objects (one lepton, p_ℓ , and two b -jets, p_{b_1} and p_{b_2}) or 4-momenta assigned by the minimisation procedure (p_W and p_ν). To find all four components, the neutrinos and the W boson without reconstructed decay products are assumed to be on-shell. Both combinations for b_1 and b_2 are evaluated during the minimisation; if only one b -tagged jet is present, it is used together with the leading or subleading jet (that means, a total of four possible jet assignments is evaluated in this case).

The minimisation is constrained such that the observed missing transverse momentum is attributed to the unobserved W boson (decaying into a not-reconstructed lepton and a neutrino) and a neutrino from the other top decay branch.

The constants a_W , a_t and a_{CM} are set to the values suggested by the authors of S : $a_W = 5 \text{ GeV}$, $a_t = 15 \text{ GeV}$, $a_{\text{CM}} = 1 \text{ TeV}$.

- Hadronic top mass, $m_{\text{had-top}}$:

This reconstructed top mass is constructed as m_{j_1,j_2,b_i} by minimising

$$\chi^2 = \frac{(m_{j_1,j_2,b_i} - m_{top})^2}{\sigma_{m_{j_1,j_2,b_i}}^2} + \frac{(m_{j_1,j_2} - m_W)^2}{\sigma_{m_{j_1,j_2}}^2},$$

where $i = 1$ or 2 ; b_1 and b_2 are the two jets with the highest b -tagging weights; j_1 , j_2 are the highest p_T jets from the selected jets in the event excluding b_1 and b_2 and

$$\begin{aligned}\sigma_{m_{j_1,j_2,b_i}}^2 &= m_{j_1,j_2,b_i}^2(r_{j_1}^2 + r_{j_2}^2 + r_{b_i}^2) \\ \sigma_{m_{j_1,j_2}}^2 &= m_{j_1,j_2}^2(r_{j_1}^2 + r_{j_2}^2),\end{aligned}$$

where r_i is the fractional jet energy uncertainty of the p_T for jet i determined by dedicated studies [105, 129].

- τ -veto:

For the construction of the τ -veto, the reconstructed τ_{had} candidates are subject to further selection requirements. Candidates are required to have either one associated track (classified as one-prong τ decay), or two to three tracks (classified as three-prong τ decay, where one track can be missed). The τ_{had} charge for candidates with one or three tracks is required to be ± 1 and to be opposite to the charge of the selected electron or muon in the event. For candidates with two tracks, the sign of the τ_{had} charge is required to be opposite to that of the selected lepton only if the τ_{had} charge is ± 2 . Finally, three different BDT requirements are imposed on the candidates to define three τ -veto working points: loose, tight, and extra-tight. In simulated $t\bar{t}$ events with one $W \rightarrow \ell\nu$ decay, signal- and background-like events are defined by requiring the other W boson to either decay into quarks (signal) or into a τ_{had} (background). In these samples, the loose (tight) τ -veto retains 99% (97%) of signal events, while for background events 81% (69%) with a one-prong and 75% (63%) with a three-prong τ_{had} decay survive the veto.

- Track-veto

Tracks are required to satisfy the following criteria: $p_T > 10$ GeV and $|\eta| < 2.5$, transverse and longitudinal impact parameters $|d_0| < 1$ mm and $|z_0| < 2$ mm. The track isolation requires that there are no additional tracks associated with the primary vertex with $p_T > 3$ GeV in a cone of $\Delta R = 0.4$ around the track. Events with at least one isolated track of opposite charge compared to that of the selected electron or muon in the event are rejected by the track-veto.

- $H_{T,\text{sig}}^{\text{miss}}$ is an object-based missing transverse momentum, divided by the per-event resolution of the jets. It is defined by

$$H_{T,\text{sig}}^{\text{miss}} = \frac{|\vec{H}_T^{\text{miss}}| - M}{\sigma_{|\vec{H}_T^{\text{miss}}|}},$$

where \vec{H}_T^{miss} is the negative sum of the jets and lepton vectors. The denominator is computed from the per-event jet energy uncertainties, while the lepton is assumed to be well-measured. The parameter M is chosen to be a characteristic ‘scale’ of the background [145], and is fixed at 100 GeV in this analysis based on optimisation studies.

B Background fit results

This section contains the background fit results for all analyses. The model-dependent selection is used. The CR and SR bins (cut-and-count and one-dimensional shape-fits) or the full set of bins (two-dimensional shape-fits) are included in the likelihood. However, a potential signal contribution is neglected everywhere (the signal strength is fixed to zero). All background uncertainties are taken into account. This fit configuration is different from the background-only fit, which is used for the validation results in section 8, in that it includes more bins to constrain the likelihood. The results of the cut-and-count analyses are given in table 12, and the results for the shape-fits are shown in tables 13–20.

Region	Obs.	Fitted (estimated) background			
		Total	$t\bar{t}$	$W + \text{jets}$	Other
tN_med					
TCR	159	159 ± 12 (155)	124 ± 14 (108)	19 ± 4 (32)	15.8 ± 2.6 (16)
WCR	161	161 ± 13 (232)	36 ± 9 (31)	109 ± 17 (185)	16 ± 5 (15)
TVR	16	26 ± 6 (26)	20 ± 5 (17)	3.4 ± 1.0 (6)	3.1 ± 0.7 (3)
WVR	25	24 ± 7 (34)	6.7 ± 2.5 (6)	15 ± 5 (26)	2.0 ± 1.0 (2)
SR	12	12.7 ± 1.8 (14)	6.3 ± 1.5 (6)	2.0 ± 0.5 (3)	4.4 ± 0.9 (4)
tN_high					
TCR	359	359 ± 19 (361)	287 ± 22 (274)	39 ± 7 (55)	32 ± 6 (32)
WCR	483	483 ± 22 (615)	100 ± 24 (95)	340 ± 40 (475)	44 ± 12 (42)
TVR	59	79 ± 18 (79)	64 ± 15 (61)	6.8 ± 2.1 (10)	8.3 ± 1.2 (8)
WVR	74	84 ± 24 (104)	22 ± 7 (21)	52 ± 16 (73)	9.7 ± 2.1 (9)
SR	5	5.0 ± 0.9 (5)	2.0 ± 0.6 (2)	0.87 ± 0.26 (1)	2.2 ± 0.4 (2)
tN_boost					
TCR	117	118 ± 11 (111)	96 ± 11 (80)	10.8 ± 2.2 (20)	11.2 ± 1.9 (11)
WCR	210	210 ± 14 (332)	35 ± 10 (29)	149 ± 20 (278)	26 ± 7 (24)
TVR	20	23 ± 5 (21)	19 ± 5 (15)	1.9 ± 0.4 (3)	2.5 ± 0.6 (2)
WVR	29	35 ± 7 (51)	7.7 ± 2.3 (6)	21 ± 5 (38)	6.3 ± 1.2 (6)
SR	5	3.5 ± 0.7 (3)	1.2 ± 0.4 (0.9)	0.31 ± 0.14 (0.5)	2.1 ± 0.4 (2)
bCc_diag					
TCR	1650	1650 ± 40 (1689)	1240 ± 60 (1246)	244 ± 34 (278)	164 ± 24 (162)
WCR	2162	2160 ± 50 (2361)	350 ± 60 (334)	1670 ± 90 (1890)	141 ± 25 (127)
TVR	925	890 ± 100 (876)	770 ± 90 (752)	46 ± 7 (51)	73 ± 7 (71)
WVR	693	740 ± 160 (781)	163 ± 35 (155)	520 ± 130 (567)	60 ± 6 (52)
SR	493	489 ± 21 (501)	158 ± 34 (145)	250 ± 27 (276)	82 ± 17 (74)
bCd_high1					
TCR	218	220 ± 15 (228)	171 ± 17 (172)	22 ± 5 (29)	28 ± 5 (27)
WCR	757	758 ± 28 (1002)	87 ± 25 (86)	610 ± 40 (860)	57 ± 16 (55)
TVR	42	53 ± 13 (53)	43 ± 11 (41)	4.5 ± 1.3 (6)	6.3 ± 1.2 (6)
WVR	166	148 ± 35 (191)	23 ± 8 (23)	111 ± 29 (153)	14.4 ± 3.4 (14)
SR	16	11.8 ± 1.4 (12)	5.6 ± 1.0 (5)	2.1 ± 0.6 (3)	4.2 ± 1.0 (4)
bCd_high2					
TCR	129	129 ± 11 (154)	92 ± 13 (110)	16 ± 4 (23)	22 ± 4 (22)
WCR	654	654 ± 26 (911)	56 ± 19 (67)	550 ± 40 (792)	53 ± 16 (52)
TVR	28	32 ± 6 (38)	23 ± 5 (28)	3.6 ± 0.9 (5)	5.7 ± 1.3 (6)
WVR	157	135 ± 29 (185)	16 ± 6 (19)	106 ± 25 (152)	13.7 ± 2.9 (13)
SR	5	4.5 ± 0.8 (5)	1.8 ± 0.4 (2)	0.73 ± 0.32 (1)	2.0 ± 0.5 (2)
tNbC_mix					
TCR	177	178 ± 13 (168)	139 ± 15 (125)	20 ± 4 (25)	18.5 ± 3.5 (18)
WCR	387	387 ± 20 (446)	80 ± 21 (71)	281 ± 31 (349)	27 ± 7 (25)
TVR	64	77 ± 19 (70)	63 ± 16 (54)	7.4 ± 1.8 (9)	7.4 ± 1.8 (7)
WVR	118	130 ± 40 (139)	33 ± 13 (29)	84 ± 28 (101)	9.4 ± 2.0 (8)
SR	10	7.6 ± 1.0 (7)	3.0 ± 0.6 (3)	1.32 ± 0.35 (2)	3.2 ± 0.7 (3)

Table 12. Results of the all-bins background fit for the cut-and-count analyses. The numbers in parenthesis are the pre-fit background estimates using the most accurate theoretical cross-sections available (cf. section 5).

tN_diag		Obs.	Fitted (estimated) background			
			Total	$t\bar{t}$	$W+\text{jets}$	Other
$E_T^{\text{miss}} < 125 \text{ GeV}$	$60 < m_T < 90 \text{ GeV} + b\text{-veto}$	1647	$1650 \pm 40 (1896)$	$550 \pm 130 (619)$	$990 \pm 150 (1159)$	$108 \pm 24 (103)$
	$60 < m_T < 90 \text{ GeV}$	3462	$3450 \pm 60 (3402)$	$3090 \pm 90 (3005)$	$180 \pm 40 (212)$	$180 \pm 50 (184)$
	$90 < m_T < 120 \text{ GeV}$	1712	$1720 \pm 40 (1693)$	$1540 \pm 50 (1487)$	$96 \pm 23 (115)$	$84 \pm 27 (89)$
	$120 < m_T < 140 \text{ GeV}$	313	$293 \pm 12 (290)$	$263 \pm 12 (256)$	$16 \pm 4 (20)$	$14 \pm 4 (14)$
	$m_T > 140 \text{ GeV}$	201	$222 \pm 11 (229)$	$202 \pm 12 (206)$	$7 \pm 4 (10)$	$12.8 \pm 3.1 (13)$
$E_T^{\text{miss}} < 150 \text{ GeV}$	$60 < m_T < 90 \text{ GeV} + b\text{-veto}$	1081	$1081 \pm 33 (1284)$	$390 \pm 80 (392)$	$620 \pm 90 (817)$	$71 \pm 15 (67)$
	$60 < m_T < 90 \text{ GeV}$	2018	$2020 \pm 40 (1984)$	$1800 \pm 60 (1718)$	$111 \pm 25 (147)$	$114 \pm 34 (118)$
	$90 < m_T < 120 \text{ GeV}$	768	$764 \pm 24 (751)$	$690 \pm 26 (664)$	$32 \pm 10 (42)$	$42 \pm 13 (44)$
	$120 < m_T < 140 \text{ GeV}$	117	$130 \pm 8 (134)$	$117 \pm 8 (118)$	$6.0 \pm 2.5 (9)$	$6.7 \pm 1.9 (7)$
	$m_T > 140 \text{ GeV}$	163	$151 \pm 7 (149)$	$136 \pm 8 (131)$	$6.2 \pm 2.6 (8)$	$9.3 \pm 2.1 (9)$
$E_T^{\text{miss}} > 150$	$60 < m_T < 90 \text{ GeV} + b\text{-veto}$	1742	$1740 \pm 40 (2172)$	$540 \pm 110 (527)$	$1080 \pm 130 (1508)$	$127 \pm 28 (130)$
	$60 < m_T < 90 \text{ GeV}$	2543	$2540 \pm 50 (2554)$	$2170 \pm 80 (2099)$	$200 \pm 40 (271)$	$170 \pm 50 (182)$
	$90 < m_T < 120 \text{ GeV}$	647	$651 \pm 24 (683)$	$565 \pm 25 (574)$	$41 \pm 9 (59)$	$45 \pm 13 (49)$
	$120 < m_T < 140 \text{ GeV}$	101	$95 \pm 6 (97)$	$82 \pm 6 (82)$	$4.5 \pm 1.4 (6)$	$8.3 \pm 2.0 (9)$
	$m_T > 140 \text{ GeV}$	217	$223 \pm 12 (234)$	$192 \pm 13 (195)$	$8.8 \pm 2.8 (14)$	$23 \pm 5 (24)$

Table 13. Results of the all-bins background fit for the tN_diag analysis. The numbers in parenthesis are the pre-fit background estimates using the most accurate theoretical cross-sections available (cf. section 5).

bCa_low	Obs.	Fitted (estimated) background			
		Total	$t\bar{t}$	$W+\text{jets}$	Other
TCR	336	$338 \pm 18 (409)$	$192 \pm 35 (250)$	$74 \pm 21 (87)$	$72 \pm 18 (72)$
WCR	1149	$1149 \pm 34 (1333)$	$62 \pm 17 (78)$	$940 \pm 50 (1115)$	$145_{-29}^{+34} (140)$
VR	74	$75 \pm 12 (90)$	$44 \pm 10 (56)$	$12.3 \pm 2.1 (14)$	$19_{-7}^{+7} (19)$
$6 < p_T^\ell < 17 \text{ GeV}$	6	$4.1 \pm 1.1 (4)$	$1.6 \pm 0.6 (2)$	$0.6 \pm 0.4 (0.7)$	$1.8_{-0.7}^{+0.8} (2)$
$17 < p_T^\ell < 28 \text{ GeV}$	6	$3.7 \pm 0.9 (4)$	$1.7 \pm 0.7 (2)$	$0.76 \pm 0.24 (0.9)$	$1.2_{-0.4}^{+0.5} (1)$
$28 < p_T^\ell < 39 \text{ GeV}$	4	$4.0 \pm 0.9 (5)$	$1.7 \pm 0.6 (2)$	$0.77 \pm 0.26 (0.9)$	$1.6_{-0.6}^{+0.6} (2)$
$39 < p_T^\ell < 50 \text{ GeV}$	3	$2.8 \pm 0.7 (3)$	$1.2 \pm 0.7 (1)$	$0.82 \pm 0.34 (0.9)$	$0.80 \pm 0.29 (0.8)$

Table 14. Results of the all-bins background fit for the bCa_low analysis. The numbers in parenthesis are the pre-fit background estimates using the most accurate theoretical cross-sections available (cf. section 5).

bCa_med	Obs.	Fitted (estimated) background			
		Total	$t\bar{t}$	$W+\text{jets}$	Other
TCR	136	136 ± 11 (157)	98 ± 16 (111)	15 ± 5 (23)	23^{+10}_{-9} (23)
WCR	189	189 ± 14 (259)	26 ± 7 (29)	121 ± 19 (188)	42^{+11}_{-11} (42)
VR	29	28 ± 5 (31)	19 ± 4 (22)	1.7 ± 0.5 (3)	$6.7^{+2.4}_{-2.2}$ (7)
$6 < p_T^\ell < 17$ GeV	9	9.2 ± 2.0 (10)	5.3 ± 1.3 (6)	0.61 ± 0.21 (0.9)	3.3 ± 1.5 (3)
$17 < p_T^\ell < 28$ GeV	15	10.9 ± 1.7 (12)	7.1 ± 1.5 (8)	1.00 ± 0.32 (1)	$2.8^{+1.1}_{-1.0}$ (3)
$28 < p_T^\ell < 39$ GeV	6	10.9 ± 1.7 (12)	7.1 ± 1.4 (8)	0.87 ± 0.31 (1)	2.9 ± 1.0 (3)
$39 < p_T^\ell < 50$ GeV	9	8.2 ± 1.4 (9)	5.7 ± 1.3 (6)	0.90 ± 0.35 (1)	$1.6^{+0.5}_{-0.5}$ (2)

Table 15. Results of the all-bins background fit for the bCa_med analysis. The numbers in parenthesis are the pre-fit background estimates using the most accurate theoretical cross-sections available (cf. section 5).

bCb_med1	Obs.	Fitted (estimated) background			
		Total	$t\bar{t}$	$W+\text{jets}$	Other
TCR	390	397 ± 20 (405)	287 ± 28 (289)	45 ± 12 (50)	65^{+11}_{-10} (65)
WCR	13724	13720 ± 130 (14480)	880 ± 200 (868)	11740 ± 330 (12507)	1100^{+190}_{-150} (1104)
VR	76	82 ± 11 (79)	50 ± 10 (47)	22.0 ± 3.3 (23)	10 ± 4 (9)
$83.3 < am_{T2} < 166.7$ GeV	111	97 ± 11 (95)	73 ± 9 (70)	3.4 ± 0.7 (4)	21^{+8}_{-5} (21)
$166.7 < am_{T2} < 250.0$ GeV	42	35 ± 4 (33)	20 ± 4 (18)	7.8 ± 1.2 (8)	$6.8^{+2.3}_{-1.2}$ (7)
$250.0 < am_{T2} < 333.3$ GeV	2	3.5 ± 0.8 (4)	1.2 ± 0.4 (1)	1.5 ± 0.4 (2)	$0.82^{+0.28}_{-0.22}$ (0.8)
$333.3 < am_{T2} < 416.7$ GeV	0	0.58 ± 0.28 (0.6)	$0.21^{+0.22}_{-0.21}$ (0.2)	0.31 ± 0.12 (0.3)	$0.064^{+0.028}_{-0.028}$ (0.1)
$416.7 < am_{T2} < 500.0$ GeV	0	0.15 ± 0.10 (0.1)	$0.025^{+0.050}_{-0.025}$ (0.0)	0.06 ± 0.06 (0.1)	0.06 ± 0.04 (0.1)

Table 16. Results of the all-bins background fit for the bCb_med1 analysis. The numbers in parenthesis are the pre-fit background estimates using the most accurate theoretical cross-sections available (cf. section 5).

bCb_high	Obs.	Fitted (estimated) background			
		Total	$t\bar{t}$	$W+\text{jets}$	Other
TCR	1111	1108 ± 34 (1131)	880 ± 50 (881)	62 ± 17 (82)	165^{+30}_{-28} (169)
WCR	4089	4090 ± 60 (4968)	530 ± 90 (535)	3140 ± 130 (4010)	420^{+60}_{-50} (423)
VR	12	13.9 ± 3.0 (16)	9.3 ± 2.7 (10)	2.9 ± 0.6 (4)	$1.7^{+1.0}_{-0.5}$ (2)
$83.3 < am_{T2} < 166.7$ GeV	11	12.9 ± 2.0 (14)	11.4 ± 1.9 (12)	0.034 ± 0.028 (0.0)	1.5 ± 0.6 (2)
$166.7 < am_{T2} < 250.0$ GeV	6	5.8 ± 1.2 (6)	4.0 ± 1.1 (4)	0.78 ± 0.26 (1)	1.07 ± 0.31 (1)
$250.0 < am_{T2} < 333.3$ GeV	4	5.1 ± 0.8 (6)	2.0 ± 0.6 (2)	1.23 ± 0.32 (2)	1.9 ± 0.5 (2)
$333.3 < am_{T2} < 416.7$ GeV	1	1.7 ± 0.6 (2)	0.47 ± 0.28 (0.6)	0.29 ± 0.15 (0.4)	$0.9^{+0.4}_{-0.4}$ (0.9)
$416.7 < am_{T2} < 500.0$ GeV	0	0.49 ± 0.23 (0.6)	$0.08^{+0.10}_{-0.08}$ (0.1)	0.17 ± 0.08 (0.2)	$0.24^{+0.18}_{-0.17}$ (0.2)

Table 17. Results of the all-bins background fit for the bCb_high analysis. The numbers in parenthesis are the pre-fit background estimates using the most accurate theoretical cross-sections available (cf. section 5).

bCb_med2		Obs.	Fitted (estimated) background			
			Total	$t\bar{t}$	$W+\text{jets}$	Other
$\frac{am_{T2}}{80 \text{ GeV}} >$	$60 < m_T < 90 \text{ GeV} + b\text{-veto}$	1069	$1067 \pm 33 \text{ (1405)}$	$103 \pm 34 \text{ (101)}$	$890 \pm 50 \text{ (1222)}$	$76 \pm 24 \text{ (80)}$
$80 < am_{T2} < 175 \text{ GeV}$	$60 < m_T < 90 \text{ GeV}$	65	$61 \pm 6 \text{ (60)}$	$57 \pm 6 \text{ (55)}$	$1.1 \pm 0.4 \text{ (2)}$	$3.1 \pm 1.1 \text{ (4)}$
	$90 < m_T < 120 \text{ GeV}$	17	$16.8 \pm 2.1 \text{ (17)}$	$15.8 \pm 2.1 \text{ (15)}$	$0.26 \pm 0.29 \text{ (0.4)}$	$0.76 \pm 0.30 \text{ (0.9)}$
	$m_T > 120 \text{ GeV}$	6	$7.5 \pm 1.1 \text{ (8)}$	$6.6 \pm 1.2 \text{ (7)}$	$0.11 \pm 0.11 \text{ (0.2)}$	$0.71 \pm 0.27 \text{ (0.8)}$
$175 < am_{T2} < 250 \text{ GeV}$	$60 < m_T < 90 \text{ GeV}$	33	$33 \pm 4 \text{ (37)}$	$20.6 \pm 3.5 \text{ (21)}$	$6.1 \pm 1.6 \text{ (9)}$	$5.9 \pm 2.0 \text{ (7)}$
	$90 < m_T < 120 \text{ GeV}$	10	$10.8 \pm 1.3 \text{ (12)}$	$7.7 \pm 1.2 \text{ (8)}$	$1.5 \pm 0.8 \text{ (2)}$	$1.6 \pm 0.6 \text{ (2)}$
	$m_T > 120 \text{ GeV}$	10	$7.0 \pm 1.0 \text{ (7)}$	$4.6 \pm 0.9 \text{ (4)}$	$0.45 \pm 0.19 \text{ (0.7)}$	$1.9 \pm 0.6 \text{ (2)}$
$am_{T2} > 250 \text{ GeV}$	$60 < m_T < 90 \text{ GeV}$	65	$72 \pm 5 \text{ (82)}$	$40 \pm 6 \text{ (40)}$	$16 \pm 4 \text{ (24)}$	$15 \pm 5 \text{ (18)}$
	$90 < m_T < 120 \text{ GeV}$	16	$18.2 \pm 2.3 \text{ (21)}$	$10.6 \pm 2.3 \text{ (11)}$	$3.5 \pm 1.4 \text{ (5)}$	$4.1 \pm 1.6 \text{ (5)}$
	$m_T > 120 \text{ GeV}$	9	$8.4 \pm 1.3 \text{ (10)}$	$3.6 \pm 0.9 \text{ (4)}$	$2.2 \pm 0.8 \text{ (3)}$	$2.6 \pm 0.8 \text{ (3)}$

Table 18. Results of the all-bins background fit for the bCb_med2 analysis. The numbers in parenthesis are the pre-fit background estimates using the most accurate theoretical cross-sections available (cf. section 5).

bCd_bulk		Obs.	Fitted (estimated) background			
			Total	$t\bar{t}$	$W+\text{jets}$	Other
$80 < am_{T2} < 175 \text{ GeV}$	$60 < m_T < 90 \text{ GeV} + b\text{-veto}$	1345	1340 ± 40 (1702)	270 ± 60 (260)	990 ± 80 (1354)	86 ± 24 (86)
	$60 < m_T < 90 \text{ GeV}$	2229	2220 ± 90 (2216)	1920 ± 90 (1846)	161 ± 30 (220)	150 ± 40 (150)
	$90 < m_T < 120 \text{ GeV}$	583	590 ± 40 (602)	516 ± 31 (518)	30 ± 6 (42)	41 ± 12 (42)
	$m_T > 120 \text{ GeV}$	361	362 ± 16 (362)	332 ± 16 (328)	8.8 ± 2.4 (13)	21 ± 5 (21)
$175 < am_{T2} < 250 \text{ GeV}$	$60 < m_T < 90 \text{ GeV} + b\text{-veto}$	705	705 ± 27 (864)	62 ± 13 (68)	594 ± 34 (749)	48 ± 14 (47)
	$60 < m_T < 90 \text{ GeV}$	547	551 ± 29 (626)	338 ± 27 (375)	140 ± 23 (177)	74 ± 19 (73)
	$90 < m_T < 120 \text{ GeV}$	144	141 ± 13 (152)	93 ± 10 (99)	30 ± 7 (37)	17 ± 5 (16)
	$m_T > 120 \text{ GeV}$	78	77 ± 5 (82)	49 ± 5 (52)	12.4 ± 3.5 (15)	15.3 ± 3.0 (15)
$am_{T2} > 250 \text{ GeV}$	$60 < m_T < 90 \text{ GeV} + b\text{-veto}$	260	260 ± 16 (344)	17 ± 5 (21)	222 ± 19 (302)	21 ± 7 (20)
	$60 < m_T < 90 \text{ GeV}$	241	239 ± 13 (285)	117 ± 19 (136)	75 ± 14 (102)	47 ± 12 (47)
	$90 < m_T < 120 \text{ GeV}$	61	65 ± 5 (78)	32 ± 6 (38)	20 ± 4 (27)	13 ± 4 (13)
	$m_T > 120 \text{ GeV}$	29	26.3 ± 2.0 (31)	10.5 ± 2.2 (12)	7.0 ± 1.5 (10)	8.8 ± 1.9 (9)

Table 19. Results of the all-bins background fit for the bCd_bulk analysis. The numbers in parenthesis are the pre-fit background estimates using the most accurate theoretical cross-sections available (cf. section 5).

3body		Obs.	Fitted (estimated) background			
			Total	$t\bar{t}$	$W+\text{jets}$	Other
$80 < am_{T2}^2 < 90 \text{ GeV}$	$60 < m_T < 90 \text{ GeV} + b\text{-veto}$	8	$9.8 \pm 2.0 \ (13)$	$2.6 \pm 0.8 \ (3)$	$6.3 \pm 2.0 \ (9)$	$0.8 \pm 0.5 \ (0.7)$
	$60 < m_T < 90 \text{ GeV}$	3	$5.9 \pm 0.8 \ (6)$	$5.1 \pm 0.8 \ (5)$	$0.52 \pm 0.31 \ (0.2)$	$0.26 \pm 0.22 \ (0.4)$
	$90 < m_T < 120 \text{ GeV}$	12	$14.6 \pm 1.7 \ (14)$	$12.0 \pm 1.7 \ (11)$	$1.6 \pm 0.7 \ (2)$	$1.0 \pm 0.6 \ (1)$
	$m_T > 120 \text{ GeV}$	8	$7.3 \pm 1.3 \ (7)$	$6.5 \pm 1.3 \ (7)$	$0.13 \pm 0.20 \ (0.1)$	$0.69 \pm 0.18 \ (0.5)$
$90 < am_{T2}^2 < 100 \text{ GeV}$	$60 < m_T < 90 \text{ GeV} + b\text{-veto}$	12	$16.8 \pm 2.9 \ (21)$	$4.1 \pm 1.1 \ (4)$	$11.8 \pm 2.8 \ (16)$	$1.0 \pm 0.6 \ (0.8)$
	$60 < m_T < 90 \text{ GeV}$	14	$16.1 \pm 1.7 \ (16)$	$13.1 \pm 1.6 \ (13)$	$1.1 \pm 0.5 \ (2)$	$1.9 \pm 0.6 \ (2)$
	$90 < m_T < 120 \text{ GeV}$	29	$30.2 \pm 2.3 \ (32)$	$24.7 \pm 2.2 \ (26)$	$3.9 \pm 1.3 \ (3)$	$1.6 \pm 1.2 \ (3)$
	$m_T > 120 \text{ GeV}$	22	$26.0 \pm 2.1 \ (26)$	$22.9 \pm 2.3 \ (23)$	$1.1 \pm 0.6 \ (1)$	$2.0 \pm 0.7 \ (2)$
$100 < am_{T2}^2 < 120 \text{ GeV}$	$60 < m_T < 90 \text{ GeV} + b\text{-veto}$	36	$35 \pm 4 \ (34)$	$7.0 \pm 1.9 \ (7)$	$26 \pm 4 \ (26)$	$2.1 \pm 0.7 \ (2)$
	$60 < m_T < 90 \text{ GeV}$	29	$32.4 \pm 2.3 \ (32)$	$27.9 \pm 2.2 \ (28)$	$3.0 \pm 1.2 \ (3)$	$1.5 \pm 0.9 \ (1)$
	$90 < m_T < 120 \text{ GeV}$	57	$59 \pm 4 \ (61)$	$51 \pm 4 \ (51)$	$3.7 \pm 2.0 \ (5)$	$3.9 \pm 2.1 \ (5)$
	$m_T > 120 \text{ GeV}$	74	$70 \pm 5 \ (66)$	$62 \pm 6 \ (58)$	$4.4 \pm 1.4 \ (4)$	$3.9 \pm 1.2 \ (4)$
$am_{T2} > 120 \text{ GeV}$	$60 < m_T < 90 \text{ GeV} + b\text{-veto}$	114	$112 \pm 10 \ (115)$	$14.4 \pm 3.3 \ (13)$	$90 \pm 11 \ (95)$	$8.0 \pm 1.9 \ (5)$
	$60 < m_T < 90 \text{ GeV}$	108	$88 \pm 5 \ (82)$	$66 \pm 5 \ (62)$	$16 \pm 4 \ (15)$	$6.2 \pm 1.7 \ (5)$
	$90 < m_T < 120 \text{ GeV}$	160	$162 \pm 10 \ (167)$	$131 \pm 10 \ (131)$	$20 \pm 5 \ (22)$	$11 \pm 4 \ (14)$
	$m_T > 120 \text{ GeV}$	281	$281 \pm 12 \ (277)$	$216 \pm 15 \ (211)$	$33 \pm 8 \ (32)$	$32 \pm 7 \ (33)$

Table 20. Results of the all-bins background fit for the 3body analysis. The numbers in parenthesis are the pre-fit background estimates using the most accurate theoretical cross-sections available (cf. section 5).

tN_diag	$E_T^{\text{miss}} \geq 150 \text{ GeV}, m_T \geq 140 \text{ GeV}$	e-channel			μ -channel		
		N_{raw}	N_{weighted}	ε	N_{raw}	N_{weighted}	ε
No requirements	200000	200000.0	100.00%	200000	200000.0	100.00%	
Trigger	113816	113762.4	56.88%	112570	112553.3	56.28%	
Event DQ	112255	112381.0	56.19%	111025	111199.1	55.60%	
Lepton (exactly 1 baseline)	28518	28785.2	14.39%	24828	25087.3	12.54%	
Lepton (exactly 1 signal)	19875	20063.4	10.03%	20034	20244.5	10.12%	
At least 3 jets $\geq 25 \text{ GeV}$	17959	18080.2	9.04%	18172	18321.3	9.16%	
At least 4 jets $\geq 25 \text{ GeV}$	13682	13647.5	6.82%	13922	13977.3	6.99%	
$\text{jet}_1 p_T \geq 60 \text{ GeV}$	12804	12765.0	6.38%	13133	13189.9	6.59%	
$\text{jet}_2 p_T \geq 60 \text{ GeV}$	9489	9502.9	4.75%	9853	9905.4	4.95%	
$\text{jet}_3 p_T \geq 40 \text{ GeV}$	8556	8613.4	4.31%	8844	8896.2	4.45%	
# b -tagged jets (70% eff.) ≥ 1	7192	7127.3	3.56%	7340	7254.7	3.63%	
$d\phi(\text{jet}_1, E_T^{\text{miss}}) \geq 0.8$	6611	6552.4	3.28%	6777	6716.6	3.36%	
$d\phi(\text{jet}_2, E_T^{\text{miss}}) \geq 0.8$	5147	5130.9	2.57%	5330	5257.5	2.63%	
$E_T^{\text{miss}} \geq 150 \text{ GeV}$	1314	1322.9	0.66%	1466	1390.2	0.70%	
$E_T^{\text{miss}}/\sqrt{H_T} \geq 5 \sqrt{\text{GeV}}$	1314	1322.9	0.66%	1465	1389.1	0.69%	
$m_T \geq 140 \text{ GeV}$	446	448.6	0.22%	535	506.7	0.25%	
$m_{\text{had-top}} = 130 - 205 \text{ GeV}$	283	271.2	0.14%	349	321.6	0.16%	
veto on loose τ 's	257	246.3	0.12%	324	298.8	0.15%	

Cut flow for tN_diag (highest E_T^{miss} and m_T bin) using a stop $\rightarrow t\chi_1^0$ signal model with $m_{\text{stop}}=350 \text{ GeV}$, $m_{\chi_1^0}=150 \text{ GeV}$. The column labelled N_{raw} shows the results for the generated number of events, while N_{weighted} includes all correction factors applied to simulation and the pileup weights. The last column labelled ε shows the full cut flow efficiency based on the N_{weighted} numbers.

tN_diag	$E_T^{\text{miss}} \geq 150 \text{ GeV}, m_T \geq 140 \text{ GeV}$	e-channel			μ -channel		
		N_{raw}	N_{weighted}	ϵ	N_{raw}	N_{weighted}	ϵ
No requirements		499999	499999.0	100.00%	499999	499999.0	100.00%
Trigger		215924	215262.1	43.05%	210250	209321.4	41.86%
Event DQ		212698	212388.4	42.48%	207080	206506.1	41.30%
Lepton (exactly 1 baseline)		66790	67474.7	13.49%	58694	58746.0	11.75%
Lepton (exactly 1 signal)		49153	49808.2	9.96%	48554	48752.9	9.75%
At least 3 jets $\geq 25 \text{ GeV}$		43828	44290.8	8.86%	43354	43416.1	8.68%
At least 4 jets $\geq 25 \text{ GeV}$		32267	32353.6	6.47%	32004	31856.9	6.37%
$\text{jet}_1 p_T \geq 60 \text{ GeV}$		29699	29763.0	5.95%	29722	29634.9	5.93%
$\text{jet}_2 p_T \geq 60 \text{ GeV}$		21368	21463.5	4.29%	21292	21218.6	4.24%
$\text{jet}_3 p_T \geq 40 \text{ GeV}$		18999	19091.0	3.82%	18921	18904.6	3.78%
# b -tagged jets (70% eff.) ≥ 1		15996	15873.5	3.17%	15959	15668.1	3.13%
$d\phi(\text{jet}_1, E_T^{\text{miss}}) \geq 0.8$		14294	14204.0	2.84%	14372	14130.6	2.83%
$d\phi(\text{jet}_2, E_T^{\text{miss}}) \geq 0.8$		10848	10798.6	2.16%	11040	10859.4	2.17%
$E_T^{\text{miss}} \geq 150 \text{ GeV}$		1492	1519.5	0.30%	1600	1590.3	0.32%
$E_T^{\text{miss}}/\sqrt{H_T} \geq 5 \sqrt{\text{GeV}}$		1490	1516.9	0.30%	1600	1590.3	0.32%
$m_T \geq 140 \text{ GeV}$		286	279.0	0.06%	320	306.6	0.06%
$m_{\text{had-top}} = 130 - 205 \text{ GeV}$		171	163.0	0.03%	216	206.2	0.04%
veto on loose τ 's		150	145.3	0.03%	183	175.1	0.04%

Cut flow for tN_diag (highest E_T^{miss} and m_T bin) using a stop $\rightarrow t\chi_1^0$ signal model with $m_{\text{stop}}=250 \text{ GeV}$, $m_{\chi_1^0}=50 \text{ GeV}$. The column labelled N_{raw} shows the results for the generated number of events, while N_{weighted} includes all correction factors applied to simulation and the pileup weights. The last column labelled ϵ shows the full cut flow efficiency based on the N_{weighted} numbers.

tN _{med}	e-channel			μ-channel		
	N _{raw}	N _{weighted}	ε	N _{raw}	N _{weighted}	ε
No requirements	100000	100000.0	100.00%	100000	100000.0	100.00%
Trigger	85484	85510.9	85.51%	85808	85953.7	85.95%
Event DQ	84453	84595.2	84.60%	84754	85008.6	85.01%
Lepton (exactly 1 baseline)	16915	16910.1	16.91%	13647	13829.8	13.83%
Lepton (exactly 1 signal)	11618	11595.0	11.59%	11130	11295.1	11.30%
At least 3 jets \geq 25 GeV	10744	10714.9	10.71%	10362	10497.1	10.50%
At least 4 jets \geq 25 GeV	8584	8523.2	8.52%	8338	8420.9	8.42%
jet ₁ p _T \geq 80 GeV	7720	7682.4	7.68%	7560	7631.3	7.63%
jet ₂ p _T \geq 60 GeV	6756	6755.0	6.76%	6678	6769.3	6.77%
jet ₃ p _T \geq 40 GeV	6234	6254.8	6.25%	6169	6249.3	6.25%
#b-tagged jets (70% eff.) \geq 1	5130	5071.4	5.07%	5107	5060.0	5.06%
d ϕ (jet ₂ , E _T ^{miss}) \geq 0.8	4408	4389.5	4.39%	4437	4400.6	4.40%
E _T ^{miss} \geq 200 GeV	2055	2035.4	2.04%	2024	2084.3	2.08%
H _{T,sig} ^{miss} \geq 12.5	1089	1081.7	1.08%	1115	1150.3	1.15%
m _T \geq 140 GeV	876	883.9	0.88%	898	917.9	0.92%
m _{had-top} =130 – 195 GeV	569	582.9	0.58%	589	603.0	0.60%
a m_{T2} \geq 170 GeV	372	384.9	0.38%	403	405.5	0.41%

Cut flow for tN_{med} using a stop \rightarrow t χ_1^0 signal model with m_{stop}=500 GeV, m _{χ_1^0} =200 GeV. The column labelled N_{raw} shows the results for the generated number of events, while N_{weighted} includes all correction factors applied to simulation and the pileup weights. The last column labelled ε shows the full cut flow efficiency based on the N_{weighted} numbers.

tN_high	e-channel			μ-channel		
	N_{raw}	N_{weighted}	ϵ	N_{raw}	N_{weighted}	ϵ
No requirements	20000	20000.0	100.00%	20000	20000.0	100.00%
Trigger	19069	19061.8	95.31%	19097	19133.1	95.67%
Event DQ	18856	18872.9	94.36%	18888	18949.1	94.75%
Lepton (exactly 1 baseline)	3403	3436.9	17.18%	2585	2536.4	12.68%
Lepton (exactly 1 signal)	2443	2462.9	12.31%	2213	2175.9	10.88%
At least 3 jets ≥ 25 GeV	2288	2304.5	11.52%	2084	2060.8	10.30%
At least 4 jets ≥ 25 GeV	1885	1929.3	9.65%	1777	1757.3	8.79%
$\text{jet}_1 p_T \geq 100$ GeV	1776	1811.6	9.06%	1675	1659.9	8.30%
$\text{jet}_2 p_T \geq 80$ GeV	1528	1565.1	7.83%	1433	1414.4	7.07%
$\text{jet}_3 p_T \geq 40$ GeV	1462	1496.5	7.48%	1371	1355.5	6.78%
# b -tagged jets (70% eff.) ≥ 1	1190	1184.6	5.92%	1145	1099.7	5.50%
$dR(\text{lepton}, \text{bjet}_1) \leq 3$	1087	1070.4	5.35%	1037	1000.6	5.00%
$E_T^{\text{miss}} \geq 320$ GeV	573	555.6	2.78%	546	518.6	2.59%
$H_{T,\text{sig}}^{\text{miss}} \geq 12.5$	552	534.0	2.67%	525	501.3	2.51%
$m_T \geq 200$ GeV	479	464.7	2.32%	451	427.2	2.14%
$m_{\text{had-top}} = 130 - 250$ GeV	374	355.1	1.78%	330	304.9	1.52%
$am_{T2} \geq 170$ GeV	330	311.7	1.56%	296	271.5	1.36%
$m_{T2}^\tau \geq 120$ GeV	317	303.5	1.52%	284	260.5	1.30%

Cut flow for tN_high using a stop $\rightarrow t\chi_1^0$ signal model with $m_{\text{stop}}=700$ GeV, $m_{\chi_1^0}=1$ GeV. The column labelled N_{raw} shows the results for the generated number of events, while N_{weighted} includes all correction factors applied to simulation and the pileup weights. The last column labelled ϵ shows the full cut flow efficiency based on the N_{weighted} numbers.

tN_boost	e-channel			μ-channel		
	N_{raw}	N_{weighted}	ε	N_{raw}	N_{weighted}	ε
No requirements	20000	20000.0	100.00%	20000	20000.0	100.00%
Trigger	19069	19061.8	95.31%	19097	19133.1	95.67%
Event DQ	18361	18813.7	94.07%	18394	18826.6	94.13%
Lepton (exactly 1 baseline)	6614	6750.2	33.75%	6582	6698.7	33.49%
Lepton (exactly 1 signal)	2234	2281.9	11.41%	2671	2670.1	13.35%
≥ 4 jets (75, 65, 40, 25) GeV	1516	1548.3	7.74%	1905	1912.7	9.56%
$\Delta\phi(\text{jet}_{1,2}, \vec{p}_T^{\text{miss}}) > 0.5, 0.3$	1437	1471.3	7.36%	1803	1805.8	9.03%
≥ 1 b-tag in 4 leading jets	1174	1162.7	5.81%	1501	1460.2	7.30%
$E_T^{\text{miss}} > 315$ GeV	600	584.8	2.92%	804	785.2	3.93%
$m_T > 175$ GeV	533	529.1	2.65%	711	688.8	3.44%
≥ 1 large- R jet, $p_T > 270$ GeV and jet mass > 75 GeV	452	440.2	2.20%	459	454.6	2.27%
$\Delta\phi(2\text{nd large-}R\text{ jet}, \vec{p}_T^{\text{miss}}) > 0.85$	444	430.2	2.15%	448	444.2	2.22%
τ veto*	419	404.1	2.02%	429	427.0	2.14%
$\min(\Delta R(\text{signal lepton}, b\text{-jet})) < 2.6$	419	404.1	2.02%	429	427.0	2.14%
topness > 7	374	357.0	1.79%	393	392.3	1.96%
$am_{T2} > 145$ GeV	362	345.7	1.73%	380	377.4	1.89%
$H_T^{\text{miss,sig}} > 10$	361	344.3	1.72%	378	377.1	1.89%

Cut flow for tN_boost using a stop $\rightarrow t\chi_1^0$ signal model with $m_{\text{stop}}=700$ GeV, $m_{\chi_1^0}=1$ GeV. *The τ veto rejects events with τ jet

BDT score > 0.55 and $\min(\text{deltaR}(\tau^{\text{had}}, \text{top/W-tagged/large-R jet})) > 2.6$. The column labelled N_{raw} shows the results for the generated number of events, while N_{weighted} includes all correction factors applied to simulation and the pileup weights. The last column labelled ε shows the full cut flow efficiency based on the N_{weighted} numbers.

bCa_med	N_{raw}	N_{weighted}	ϵ			
No requirements	10405773	10405773.0	100.00%			
Generator filter ($E_T^{\text{miss}}(\text{gen}) > 250$ GeV)	99500	99500.0	0.96%			
$E_T^{\text{miss}} \text{ trigger}$	99469	98261.3	0.94%			
Event DQ	96429	95314.1	0.92%			
$E_T^{\text{miss}} > 300$ GeV	45736	45285.2	0.44%			
	e-channel		μ-channel			
	N_{raw}	N_{weighted}	ϵ	N_{raw}	N_{weighted}	ϵ
Lepton (exactly 1 baseline)	3852	3788.1	0.036%	4638	4562.7	0.044%
Lepton (exactly 1 signal)	3635	3612.3	0.035%	4433	4423.6	0.043%
Lepton $p_T < 50$ GeV	3446	3438.4	0.033%	4276	4272.2	0.041%
At least 3 jets ≥ 25 GeV	2823	2813.3	0.027%	3542	3550.4	0.034%
$\text{jet}_1 p_T > 180$ GeV	2717	2695.3	0.026%	3433	3444.6	0.033%
# b -tagged jets (70% eff.) ≥ 1	1945	1930.7	0.019%	2458	2472.8	0.024%
jet_1 is not b -tagged	1846	1835.1	0.018%	2323	2332.0	0.022%
$m_T > 100$ GeV	218	235.1	0.0023%	219	227.3	0.0022%
$E_T^{\text{miss}}/m_{\text{eff}} > 0.3$	184	191.3	0.0018%	184	189.2	0.0018%
Lepton $p_T < 25$ GeV	116	127.2	0.0012%	124	128.1	0.0012%

Cut flow for bCa_low using a stop $\rightarrow b\chi_1^\pm$ signal model with $m_{\text{stop}}=175$ GeV, $m_{\chi_1^\pm}=165$ GeV, $m_{\chi_1^0}=145$ GeV. The column labelled N_{raw} shows the results for the generated number of events, while N_{weighted} includes all correction factors applied to simulation and the pileup weights. The last column labelled ϵ shows the full cut flow efficiency based on the N_{weighted} numbers. The generator filter of $E_T^{\text{miss}}(\text{gen}) > 250$ GeV (a vectorial sum of invisible particles) was applied to improve statistical precision. (In the actual analysis, the sample was used by combining it with another sample with $E_T^{\text{miss}}(\text{gen}) = [60, 250]$ GeV to estimate signal contamination in the control regions. The fraction of the second sample in $E_T^{\text{miss}} > 300$ GeV is less than 1%.)

bCa_low	N_{raw}	N_{weighted}	ϵ			
No requirements	7324720	7324720.0	100.00%			
Generator filter ($E_T^{\text{miss}}(\text{gen}) > 250$ GeV)	99499	99499.0	1.36%			
E_T^{miss} trigger	99478	98160.2	1.34%			
Event DQ	97010	95792.0	1.31%			
$E_T^{\text{miss}} > 370$ GeV	20202	19923.9	0.27%			
	e-channel		μ-channel			
	N_{raw}	N_{weighted}	ϵ	N_{raw}	N_{weighted}	ϵ
Lepton (exactly 1 baseline)	1680	1640.0	0.022%	1971	1951.2	0.027%
Lepton (exactly 1 signal)	1575	1557.6	0.021%	1815	1887.1	0.026%
Lepton $p_T < 50$ GeV	1493	1483.6	0.020%	1815	1827.9	0.025%
At least 2 jets ≥ 25 GeV	1473	1466.1	0.020%	1791	1809.4	0.025%
$\text{jet}_1 p_T > 180$ GeV	1325	1305.2	0.018%	1638	1665.5	0.023%
# b-tagged jets (70% eff.) ≥ 1	446	470.0	0.0064%	564	583.7	0.0080%
jet_1 is not b-tagged	401	414.8	0.0057%	509	522.8	0.0071%
$m_T > 90$ GeV	95	92.4	0.0013%	121	129.6	0.0018%
$E_T^{\text{miss}}/m_{\text{eff}} > 0.35$	81	81.7	0.0011%	103	114.9	0.0016%
Lepton $p_T < 25$ GeV	53	52.2	0.0007%	81	89.6	0.0012%

Cut flow for bCa_low using a stop $\rightarrow b\chi_1^\pm$ signal model with $m_{\text{stop}}=175$ GeV, $m_{\chi_1^\pm}=165$ GeV, $m_{\chi_1^0}=145$ GeV. The column labelled N_{raw} shows the results for the generated number of events, while N_{weighted} includes all correction factors applied to simulation and the pileup weights. The last column labelled ϵ shows the full cut flow efficiency based on the N_{weighted} numbers. The generator filter of $E_T^{\text{miss}}(\text{gen}) > 250$ GeV (a vectorial sum of invisible particles) was applied to improve statistical precision. (In the actual analysis, the sample was used by combining it with another sample with $E_T^{\text{miss}}(\text{gen}) = [60, 250]$ GeV to estimate signal contamination in the control regions. The fraction of the second sample in $E_T^{\text{miss}} > 300$ GeV is less than 1%).

bCb_med1	N_{raw}	N_{weighted}	ε			
No requirements	118408	118408.0	100.00%			
Generator filter ($E_T^{\text{miss}}(\text{gen}) > 60$ GeV)	100000	100000.0	84.45%			
E_T^{miss} trigger	80637	79923.5	67.50%			
Event DQ	78696	78172.5	66.02%			
$E_T^{\text{miss}} > 150$ GeV	40209	40022.2	33.80%			
	e-channel		μ-channel			
	N_{raw}	N_{weighted}	ε	N_{raw}	N_{weighted}	ε
Lepton (exactly 1 baseline)	3570	3505.1	2.96%	4829	4773.5	4.03%
Lepton (exactly 1 signal)	3377	3342.5	2.82%	4710	4717.6	3.98%
Lepton $p_T < 25$ GeV	2475	2408.0	2.03%	3651	3669.2	3.10%
jet ₁ $p_T > 60$ GeV	2469	2403.9	2.03%	3641	3657.1	3.09%
jet ₂ $p_T > 60$ GeV	1977	1901.0	1.61%	2893	2917.5	2.46%
Leading two jets are b-tagged (60% eff.)	486	434.0	0.37%	726	655.0	0.55%
$\Delta\phi(j, E_T^{\text{miss}}) > 0.4$	474	426.6	0.36%	712	642.1	0.54%
$H_{T,2} < 50$ GeV	282	253.2	0.21%	400	356.8	0.30%
$m_{bb} > 150$ GeV	199	168.5	0.14%	269	235.0	0.20%
$am_{T2} > 170$ GeV	162	141.8	0.12%	224	197.9	0.17%

Cut flow for bCb_med1 using a stop $\rightarrow b\chi_1^\pm$ signal model with $m_{\text{stop}}=300$ GeV, $m_{\chi_1^\pm}=120$ GeV, $m_{\chi_1^0}=100$ GeV. The column labelled N_{raw} shows the results for the generated number of events, while N_{weighted} includes all correction factors applied to simulation and the pileup weights. The last column labelled ε shows the full cut flow efficiency based on the N_{weighted} numbers. The generator filter of $E_T^{\text{miss}}(\text{gen}) > 60$ GeV (a vectorial sum of invisible particles) was applied.

bCb_high	N_{raw}	N_{weighted}	ε			
No requirements	15676	15676.0	100.00%			
Generator filter ($E_T^{\text{miss}}(\text{gen}) > 60$ GeV)	15000	15000.0	95.69%			
E_T^{miss} trigger	14216	14115.7	90.05%			
Event DQ	13811	13719.3	87.52%			
$E_T^{\text{miss}} > 250$ GeV	7386	7280.3	46.44%			
	e-channel		μ-channel			
	N_{raw}	N_{weighted}	ε	N_{raw}	N_{weighted}	ε
Lepton (exactly 1 baseline)	808	795.1	5.07%	1006	1000.1	6.38%
Lepton (exactly 1 signal)	751	746.3	4.76%	970	971.4	6.20%
Lepton $p_T < 25$ GeV	404	403.2	2.57%	567	562.0	3.59%
$\text{jet}_1 p_T > 60$ GeV	404	403.2	2.57%	567	562.0	3.59%
$\text{jet}_2 p_T > 60$ GeV	382	378.3	2.41%	545	535.6	3.42%
Leading two jets are b-tagged (60% eff.)	103	83.6	0.53%	151	120.7	0.77%
$\Delta\phi(j, E_T^{\text{miss}}) > 0.4$	99	80.3	0.51%	148	117.0	0.75%
$m_{bb} > 150$ GeV	90	72.9	0.47%	132	103.8	0.66%
$am_{T2} > 200$ GeV	86	71.3	0.45%	127	100.7	0.64%

Cut flow for bCb_high using a stop $\rightarrow b\chi_1^\pm$ signal model with $m_{\text{stop}}=550$ GeV, $m_{\chi_1^\pm}=120$ GeV, $m_{\chi_1^0}=100$ GeV. The column labelled N_{raw} shows the results for the generated number of events, while N_{weighted} includes all correction factors applied to simulation and the pileup weights. The last column labelled ε shows the full cut flow efficiency based on the N_{weighted} numbers. The generator filter of $E_T^{\text{miss}}(\text{gen}) > 60$ GeV (a vectorial sum of invisible particles) was applied.

bCb_med2	$am_{T2} \geq 250$ GeV	e-channel			μ -channel		
		N_{raw}	N_{weighted}	ϵ	N_{raw}	N_{weighted}	ϵ
No requirements	238296	238295.7	100.00%	238296	238295.7	0.63%	
Generator filter (lepton)	150000	150000.0	62.95%	150000	150000.0	62.95%	
Trigger	113739	114048.4	47.86%	113942	114184.3	47.92%	
Event DQ	112265	112727.9	47.31%	112469	112859.7	47.36%	
Lepton (exactly 1 baseline)	30284	30911.7	12.97%	28911	29078.0	12.20%	
Lepton (exactly 1 signal)	18031	18542.3	7.78%	19216	19337.1	8.11%	
At least 3 jets ≥ 25 GeV	16314	16710.8	7.01%	17315	17293.8	7.26%	
At least 4 jets ≥ 25 GeV	11883	11946.5	5.01%	12669	12414.2	5.21%	
$jet_1 p_T \geq 80$ GeV	11645	11719.1	4.92%	12375	12129.5	5.09%	
$jet_2 p_T \geq 60$ GeV	10893	10988.0	4.61%	11629	11400.8	4.78%	
$jet_3 p_T \geq 40$ GeV	9928	10043.3	4.21%	10570	10359.3	4.35%	
# b -tagged jets (80% eff.) ≥ 2	6562	6300.9	2.64%	6959	6411.4	2.69%	
$bjet_1 p_T \geq 140$ GeV	4604	4317.6	1.81%	4937	4495.4	1.89%	
$bjet_2 p_T \geq 75$ GeV	3710	3447.3	1.45%	3940	3562.9	1.50%	
$d\phi(jet_1, E_T^{\text{miss}}) \geq 0.8$	3559	3312.4	1.39%	3769	3408.7	1.43%	
$d\phi(jet_2, E_T^{\text{miss}}) \geq 0.8$	2891	2692.2	1.13%	3021	2737.6	1.15%	
$E_T^{\text{miss}} \geq 170$ GeV	999	926.9	0.39%	1029	926.2	0.39%	
$E_T^{\text{miss}}/\sqrt{H_T} \geq 6 \sqrt{\text{GeV}}$	983	914.1	0.38%	1017	915.0	0.38%	
$m_T \geq 60$ GeV	435	403.7	0.17%	436	376.1	0.16%	
$am_{T2} \geq 250$ GeV	206	183.3	0.08%	210	193.3	0.08%	
veto on isolated tracks	168	145.4	0.06%	174	152.6	0.06%	
veto on tight τ 's	163	140.3	0.06%	172	151.3	0.06%	
topness ≥ 7.5	162	139.8	0.06%	172	151.3	0.06%	

Cut flow for bCb_med2 (high am_{T2} bin, sum of all m_T bins) using a $\text{stop} \rightarrow b\chi_1^\pm$ signal model with $m_{\text{stop}}=350$ GeV, $m_{\chi_1^\pm}=100$ GeV, $m_{\chi_1^0}=50$ GeV. The generator lepton filter requires at least one stable electron or muon with $p_T > 10$ GeV and $|\eta| < 2.8$.

The column labelled N_{raw} shows the results for the generated number of events, while N_{weighted} includes all correction factors applied to simulation and the pileup weights. The last column labelled ϵ shows the full cut flow efficiency based on the N_{weighted} numbers.

bCb_med2 $am_{T2} \geq 250$ GeV	e-channel			μ -channel		
	N_{raw}	N_{weighted}	ϵ	N_{raw}	N_{weighted}	ϵ
No requirements	118828	118828.4	100.00%	118828	118828.4	0.67%
Generator filter (lepton)	80000	80000.0	67.32%	80000	80000.0	67.32%
Trigger	67553	67531.1	56.83%	67151	67171.0	56.53%
Event DQ	66800	66836.6	56.25%	66405	66481.0	55.95%
Lepton (exactly 1 baseline)	19571	19714.7	16.59%	17212	17428.8	14.67%
Lepton (exactly 1 signal)	13859	13978.1	11.76%	14105	14273.3	12.01%
At least 3 jets ≥ 25 GeV	13328	13433.1	11.30%	13552	13678.4	11.51%
At least 4 jets ≥ 25 GeV	11271	11389.1	9.58%	11479	11572.8	9.74%
$\text{jet}_1 p_T \geq 80$ GeV	11061	11177.3	9.41%	11300	11393.9	9.59%
$\text{jet}_2 p_T \geq 60$ GeV	10554	10676.3	8.98%	10780	10893.2	9.17%
$\text{jet}_3 p_T \geq 40$ GeV	9970	10100.2	8.50%	10229	10376.3	8.73%
# b -tagged jets (80% eff.) ≥ 2	6230	6000.5	5.05%	6465	6227.6	5.24%
$\text{bjet}_1 p_T \geq 140$ GeV	4396	4169.8	3.51%	4638	4402.7	3.71%
$\text{bjet}_2 p_T \geq 75$ GeV	3570	3371.5	2.84%	3786	3560.8	3.00%
$d\phi(\text{jet}_1, E_T^{\text{miss}}) \geq 0.8$	3331	3125.6	2.63%	3558	3352.1	2.82%
$d\phi(\text{jet}_2, E_T^{\text{miss}}) \geq 0.8$	2646	2506.7	2.11%	2862	2714.9	2.28%
$E_T^{\text{miss}} \geq 170$ GeV	1310	1223.6	1.03%	1412	1357.6	1.14%
$E_T^{\text{miss}}/\sqrt{H_T} \geq 6 \sqrt{\text{GeV}}$	1302	1217.7	1.02%	1403	1348.7	1.13%
$m_T \geq 60$ GeV	1068	996.4	0.84%	1157	1105.9	0.93%
$am_{T2} \geq 250$ GeV	500	443.5	0.37%	532	501.4	0.42%
veto on isolated tracks	415	378.3	0.32%	435	404.8	0.34%
veto on tight τ 's	412	373.9	0.31%	430	402.3	0.34%
topness ≥ 7.5	411	373.9	0.31%	430	402.3	0.34%

Cut flow for bCb_med2 (high am_{T2} bin, sum of all m_T bins) using a stop $\rightarrow b\chi_1^\pm$ signal model with $m_{\text{stop}}=500$ GeV, $m_{\chi_1^\pm}=300$ GeV, $m_{\chi_1^0}=150$ GeV. The generator lepton filter requires at least one stable electron or muon with $p_T > 10$ GeV and $|\eta| < 2.8$.

The column labelled N_{raw} shows the results for the generated number of events, while N_{weighted} includes all correction factors applied to simulation and the pileup weights. The last column labelled ϵ shows the full cut flow efficiency based on the N_{weighted} numbers.

bCc_diag	e-channel			μ-channel		
	N _{raw}	N _{weighted}	ε	N _{raw}	N _{weighted}	ε
No requirements	874542	874542.0	100.00%	874542	874542.0	0.46%
Generator filter (lepton)	399998	399998.0	45.74%	399998	399998.0	45.74%
Trigger	189811	190006.4	21.73%	182028	182029.8	20.81%
Event DQ	188379	188602.8	21.57%	180458	180480.6	20.64%
Lepton (exactly 1 baseline)	110795	112160.2	12.83%	99137	99227.0	11.35%
Lepton (exactly 1 signal)	89206	90483.3	10.35%	85244	85343.3	9.76%
At least 3 jets ≥ 25 GeV	28978	29210.3	3.34%	28590	28542.4	3.26%
jet ₁ p _T ≥ 80 GeV	12870	13239.6	1.51%	13074	13284.1	1.52%
jet ₂ p _T ≥ 40 GeV	10871	11202.8	1.28%	11031	11215.4	1.28%
jet ₃ p _T ≥ 30 GeV	8960	9235.3	1.06%	9073	9238.3	1.06%
no b-tagged jets (70% eff.)	7439	7623.9	0.87%	7552	7651.5	0.87%
lepton $\eta \leq 1.2$	5937	6100.8	0.70%	5610	5679.5	0.65%
d ϕ (jet ₁ , E _T ^{miss}) ≥ 2	4968	5109.0	0.58%	4702	4755.8	0.54%
d ϕ (jet ₂ , E _T ^{miss}) ≥ 0.8	3721	3813.9	0.44%	3477	3513.9	0.40%
dR(lepton, jet ₁)=0.8 – 2.4	1106	1124.5	0.13%	1196	1202.8	0.14%
E _T ^{miss} ≥ 140 GeV	342	352.0	0.04%	391	397.1	0.05%
E _T ^{miss} / $\sqrt{H_T} \geq 5 \sqrt{\text{GeV}}$	342	352.0	0.04%	391	397.1	0.05%
m _T ≥ 120 GeV	174	178.9	0.02%	184	184.8	0.02%

Cut flow for bCc_diag using a stop $\rightarrow b\chi_1^\pm$ signal model with m_{stop}=180 GeV, m _{χ_1^\pm} =174 GeV, m _{χ_1^0} =87 GeV. The generator lepton filter requires at least one stable electron or muon with p_T > 10 GeV and |η| < 2.8. The column labelled N_{raw} shows the results for the generated number of events, while N_{weighted} includes all correction factors applied to simulation and the pileup weights. The last column labelled ε shows the full cut flow efficiency based on the N_{weighted} numbers.

bCd_bulk $m_T \geq 120$ GeV, $am_{T2} \geq 175$ GeV	e-channel			μ -channel		
	N_{raw}	N_{weighted}	ϵ	N_{raw}	N_{weighted}	ϵ
No requirements	662634	662634.0	100.00%	662634	662634.0	0.60%
Generator filter (lepton)	399999	399999.0	60.37%	399999	399999.0	60.37%
Trigger	240852	240973.5	36.37%	237662	237758.8	35.88%
Event DQ	238011	238405.8	35.98%	234844	235194.9	35.49%
Lepton (exactly 1 baseline)	92532	93655.4	14.13%	83724	84324.8	12.73%
Lepton (exactly 1 signal)	66085	67153.8	10.13%	66832	67346.1	10.16%
At least 3 jets ≥ 25 GeV	59446	60204.0	9.09%	60209	60460.6	9.12%
At least 4 jets ≥ 25 GeV	43977	44254.9	6.68%	44806	44711.1	6.75%
$jet_1 p_T \geq 80$ GeV	34495	34827.8	5.26%	35533	35527.0	5.36%
$jet_2 p_T \geq 60$ GeV	28644	29083.9	4.39%	29441	29489.7	4.45%
$jet_3 p_T \geq 40$ GeV	25782	26240.1	3.96%	26495	26592.1	4.01%
# b -tagged jets (70% eff.) ≥ 1	22293	22142.4	3.34%	23054	22766.3	3.44%
$d\phi(jet_1, E_T^{\text{miss}}) \geq 0.8$	20417	20292.6	3.06%	21238	21004.8	3.17%
$d\phi(jet_2, E_T^{\text{miss}}) \geq 0.8$	15617	15483.2	2.34%	16315	16173.9	2.44%
$E_T^{\text{miss}} \geq 150$ GeV	3584	3625.1	0.55%	3907	3888.2	0.59%
$E_T^{\text{miss}} / \sqrt{H_T} \geq 7 \sqrt{\text{GeV}}$	3407	3449.9	0.52%	3694	3669.8	0.55%
$m_T \geq 120$ GeV	1252	1284.2	0.19%	1557	1519.3	0.23%
$am_{T2} \geq 175$ GeV	339	346.3	0.05%	467	475.3	0.07%
veto on isolated tracks	253	255.5	0.04%	368	365.4	0.06%
veto on tight τ 's	247	250.3	0.04%	365	363.0	0.05%

Cut flow for bCd_bulk (intermediate+high am_{T2} , highest m_T bins) using a stop $\rightarrow b\chi_1^\pm$ signal model with $m_{\text{stop}}=300$ GeV, $m_{\chi_1^\pm}=200$ GeV, $m_{\chi_1^0}=100$ GeV. The generator lepton filter requires at least one stable electron or muon with $p_T > 10$ GeV and $|\eta| < 2.8$. The column labelled N_{raw} shows the results for the generated number of events, while N_{weighted} includes all correction factors applied to simulation and the pileup weights. The last column labelled ϵ shows the full cut flow efficiency based on the N_{weighted} numbers.

bCd_high1	e-channel			μ -channel		
	N_{raw}	N_{weighted}	ε	N_{raw}	N_{weighted}	ε
No requirements	115297	115297.0	100.00%	115297	115297.0	0.69%
Generator filter (lepton)	80000	80000.0	69.39%	80000	80000.0	69.39%
Trigger	69610	69568.9	60.34%	69596	69595.6	60.36%
Event DQ	68794	68818.5	59.69%	68790	68859.4	59.72%
Lepton (exactly 1 baseline)	19352	19586.1	16.99%	16955	16945.7	14.70%
Lepton (exactly 1 signal)	13626	13854.3	12.02%	13737	13769.9	11.94%
At least 3 jets ≥ 25 GeV	13169	13378.5	11.60%	13256	13249.1	11.49%
At least 4 jets ≥ 25 GeV	11315	11551.6	10.02%	11457	11458.8	9.94%
$\text{jet}_1 p_T \geq 80$ GeV	11230	11467.5	9.95%	11359	11354.3	9.85%
$\text{jet}_2 p_T \geq 60$ GeV	10858	11088.0	9.62%	11010	11022.2	9.56%
$\text{jet}_3 p_T \geq 40$ GeV	10396	10613.9	9.21%	10531	10572.8	9.17%
# b -tagged jets (80% eff.) ≥ 2	6675	6344.8	5.50%	6744	6305.6	5.47%
$\text{bjet}_1 p_T \geq 75$ GeV	6604	6266.1	5.43%	6679	6229.2	5.40%
$\text{bjet}_2 p_T \geq 75$ GeV	5337	4999.8	4.34%	5386	4960.4	4.30%
$d\phi(\text{jet}_1, E_T^{\text{miss}}) \geq 0.8$	5048	4726.7	4.10%	5116	4689.2	4.07%
$d\phi(\text{jet}_2, E_T^{\text{miss}}) \geq 0.8$	4150	3922.6	3.40%	4235	3884.0	3.37%
$E_T^{\text{miss}} \geq 150$ GeV	2625	2458.3	2.13%	2718	2497.2	2.17%
$E_T^{\text{miss}}/\sqrt{H_T} \geq 9 \sqrt{\text{GeV}}$	1681	1558.9	1.35%	1725	1547.0	1.34%
$m_T \geq 120$ GeV	927	852.6	0.74%	1039	961.8	0.83%
$m_{eff} \geq 600$ GeV	903	832.1	0.72%	1016	937.8	0.81%
$am_{T2} \geq 200$ GeV	757	689.0	0.60%	851	782.9	0.68%
veto on isolated tracks	609	569.8	0.49%	702	639.5	0.55%
veto on tight τ 's	601	563.6	0.49%	693	630.9	0.55%

Cut flow for bCd_high1 using a stop $\rightarrow b\chi_1^\pm$ signal model with $m_{\text{stop}}=550$ GeV, $m_{\chi_1^\pm}=300$ GeV, $m_{\chi_1^0}=150$ GeV. The generator lepton filter requires at least one stable electron or muon with $p_T > 10$ GeV and $|\eta| < 2.8$. The column labelled N_{raw} shows the results for the generated number of events, while N_{weighted} includes all correction factors applied to simulation and the pileup weights. The last column labelled ε shows the full cut flow efficiency based on the N_{weighted} numbers.

bCd_high2	e-channel			μ -channel		
	N_{raw}	N_{weighted}	ϵ	N_{raw}	N_{weighted}	ϵ
No requirements	69358	69357.7	100.00%	69358	69357.7	0.72%
Generator filter (lepton)	50000	50000.0	72.09%	50000	50000.0	72.09%
Trigger	44923	44878.7	64.71%	45048	45086.2	65.01%
Event DQ	44355	44352.4	63.95%	44485	44557.6	64.24%
Lepton (exactly 1 baseline)	11735	11817.5	17.04%	10559	10615.8	15.31%
Lepton (exactly 1 signal)	7872	7942.4	11.45%	8162	8182.6	11.80%
At least 3 jets ≥ 25 GeV	7669	7724.3	11.14%	7969	7975.5	11.50%
At least 4 jets ≥ 25 GeV	6663	6762.9	9.75%	6987	7051.6	10.17%
$\text{jet}_1 p_T \geq 80$ GeV	6651	6750.0	9.73%	6974	7038.0	10.15%
$\text{jet}_2 p_T \geq 80$ GeV	6301	6399.0	9.23%	6611	6659.4	9.60%
$\text{jet}_3 p_T \geq 40$ GeV	6087	6185.8	8.92%	6412	6465.6	9.32%
# b -tagged jets (80% eff.) ≥ 2	3931	3690.1	5.32%	4192	3883.6	5.60%
$\text{bjet}_1 p_T \geq 170$ GeV	3341	3096.3	4.46%	3605	3286.7	4.74%
$\text{bjet}_2 p_T \geq 80$ GeV	3030	2769.8	3.99%	3243	2953.8	4.26%
$d\phi(\text{jet}_1, E_T^{\text{miss}}) \geq 0.8$	2944	2680.6	3.86%	3145	2862.1	4.13%
$d\phi(\text{jet}_2, E_T^{\text{miss}}) \geq 0.8$	2443	2202.4	3.18%	2615	2389.5	3.45%
$E_T^{\text{miss}} \geq 160$ GeV	1742	1569.0	2.26%	1881	1726.2	2.49%
$E_T^{\text{miss}}/\sqrt{H_T} \geq 8 \sqrt{\text{GeV}}$	1296	1177.9	1.70%	1457	1329.1	1.92%
$m_T \geq 120$ GeV	469	425.8	0.61%	569	511.1	0.74%
$am_{T2} \geq 250$ GeV	368	324.4	0.47%	463	385.0	0.56%
veto on isolated tracks	282	252.7	0.36%	371	314.9	0.45%
veto on tight τ 's	280	252.4	0.36%	366	309.7	0.45%

Cut flow for bCd_high2 using a $\text{stop} \rightarrow b\chi_1^\pm$ signal model with $m_{\text{stop}}=600$ GeV, $m_{\chi_1^\pm}=200$ GeV, $m_{\chi_1^0}=100$ GeV. The generator lepton filter requires at least one stable electron or muon with $p_T > 10$ GeV and $|\eta| < 2.8$. The column labelled N_{raw} shows the results for the generated number of events, while N_{weighted} includes all correction factors applied to simulation and the pileup weights. The last column labelled ϵ shows the full cut flow efficiency based on the N_{weighted} numbers.

3body	$m_T \geq 120$ GeV, $am_{T2} \leq 100$ GeV	e-channel			μ -channel		
		N_{raw}	N_{weighted}	ε	N_{raw}	N_{weighted}	ε
No requirements	2145802	2145802.3	100.00%	2145802	2145802.3	0.19%	
Generator filter (lepton, E_T^{miss})	399999	399999.0	18.64%	399999	399999.0	18.64%	
Trigger	261559	261725.6	12.20%	265171	264835.6	12.34%	
Event DQ	257663	258318.9	12.04%	261126	261260.8	12.18%	
Lepton (exactly 1 baseline)	121380	122905.5	5.73%	105784	106571.4	4.97%	
Lepton (exactly 1 signal)	95153	96551.4	4.50%	92209	92883.3	4.33%	
At least 3 jets ≥ 25 GeV	72548	72958.4	3.40%	71471	71331.5	3.32%	
At least 4 jets ≥ 25 GeV	46281	46290.4	2.16%	46093	45593.5	2.12%	
$\text{jet}_1 p_T \geq 80$ GeV	28392	28579.3	1.33%	29138	29145.7	1.36%	
$\text{jet}_2 p_T \geq 25$ GeV	28392	28579.3	1.33%	29138	29145.7	1.36%	
$\text{jet}_3 p_T \geq 25$ GeV	28392	28579.3	1.33%	29138	29145.7	1.36%	
# b -tagged jets (70% eff.) ≥ 1	20272	20268.0	0.94%	20911	20781.8	0.97%	
$d\phi(\text{jet}_1, E_T^{\text{miss}}) \geq 0.2$	19961	19965.4	0.93%	20641	20542.1	0.96%	
$d\phi(\text{jet}_2, E_T^{\text{miss}}) \geq 0.2$	18686	18701.9	0.87%	19348	19256.1	0.90%	
$d\phi(\text{lepton}, E_T^{\text{miss}}) \geq 1.25$	9729	9706.3	0.45%	10140	10071.7	0.47%	
$dR(\text{lepton}, \text{jet}_1) \geq 1.25$	7945	7930.8	0.37%	8386	8343.2	0.39%	
$dR(\text{lepton}, \text{jet}_2) \geq 2$	3795	3731.4	0.17%	4094	4108.2	0.19%	
$E_T^{\text{miss}} \geq 150$ GeV	374	363.8	0.02%	454	458.3	0.02%	
$E_T^{\text{miss}}/\sqrt{H_T} \geq 5 \sqrt{\text{GeV}}$	374	363.8	0.02%	454	458.3	0.02%	
$m_T \geq 120$ GeV	243	233.8	0.01%	297	304.8	0.01%	
$am_{T2}=80 - 100$ GeV	59	57.1	0.00%	99	98.6	0.00%	
veto on tight τ 's	51	51.3	0.00%	93	92.0	0.00%	

Cut flow for the 3body signal region (two lowest am_{T2} bins, sum of all m_T bins) using a three-body stop decay signal model with $m_{\text{stop}}=200$ GeV, $m_{\chi_1^0}=50$ GeV. The generator filter requires at least one stable electron or muon with $p_T > 20$ GeV and $|\eta| < 2.8$, as well as $E_T^{\text{miss}} > 60$ GeV. The column labelled N_{raw} shows the results for the generated number of events, while N_{weighted} includes all correction factors applied to simulation and the pileup weights. The last column labelled ε shows the full cut flow efficiency based on the N_{weighted} numbers.

3body $m_T \geq 120$ GeV, $am_{T2} \leq 100$ GeV	e-channel			μ -channel		
	N_{raw}	N_{weighted}	ε	N_{raw}	N_{weighted}	ε
No requirements	915106	915106.2	100.00%	915106	915106.2	0.22%
Generator filter (lepton, E_T^{miss})	198999	198999.0	21.75%	198999	198999.0	21.75%
Trigger	136697	137284.9	15.00%	138676	139256.7	15.22%
Event DQ	134774	135650.3	14.82%	136669	137519.2	15.03%
Lepton (exactly 1 baseline)	61592	62541.2	6.83%	52946	53587.5	5.86%
Lepton (exactly 1 signal)	47828	48672.2	5.32%	45952	46546.4	5.09%
At least 3 jets ≥ 25 GeV	38160	38511.9	4.21%	37071	37327.4	4.08%
At least 4 jets ≥ 25 GeV	25510	25601.6	2.80%	25050	25045.3	2.74%
$\text{jet}_1 p_T \geq 80$ GeV	16479	16691.4	1.82%	16461	16573.5	1.81%
$\text{jet}_2 p_T \geq 25$ GeV	16479	16691.4	1.82%	16461	16573.5	1.81%
$\text{jet}_3 p_T \geq 25$ GeV	16479	16691.4	1.82%	16461	16573.5	1.81%
# b -tagged jets (70% eff.) ≥ 1	11521	11618.5	1.27%	11489	11465.9	1.25%
$d\phi(\text{jet}_1, E_T^{\text{miss}}) \geq 0.2$	11360	11455.7	1.25%	11339	11308.6	1.24%
$d\phi(\text{jet}_2, E_T^{\text{miss}}) \geq 0.2$	10616	10683.0	1.17%	10687	10669.8	1.17%
$d\phi(\text{lepton}, E_T^{\text{miss}}) \geq 1.25$	5701	5731.1	0.63%	5720	5733.5	0.63%
$dR(\text{lepton}, \text{jet}_1) \geq 1.25$	4613	4639.3	0.51%	4763	4772.9	0.52%
$dR(\text{lepton}, \text{jet}_2) \geq 2$	2273	2297.2	0.25%	2325	2317.1	0.25%
$E_T^{\text{miss}} \geq 150$ GeV	404	412.6	0.05%	477	484.4	0.05%
$E_T^{\text{miss}}/\sqrt{H_T} \geq 5 \sqrt{\text{GeV}}$	404	412.6	0.05%	477	484.4	0.05%
$m_T \geq 120$ GeV	317	324.9	0.04%	366	369.4	0.04%
$am_{T2}=80 - 100$ GeV	98	103.5	0.01%	111	109.7	0.01%
veto on tight τ 's	89	95.4	0.01%	108	107.5	0.01%

Cut flow for the 3body signal region (two lowest am_{T2} bins, sum of all m_T bins) using a three-body stop decay signal model with $m_{\text{stop}}=250$ GeV, $m_{\chi_1^0}=100$ GeV. The generator filter requires at least one stable electron or muon with $p_T > 20$ GeV and $|\eta| < 2.8$, as well as $E_T^{\text{miss}} > 60$ GeV. The column labelled N_{raw} shows the results for the generated number of events, while N_{weighted} includes all correction factors applied to simulation and the pileup weights. The last column labelled ε shows the full cut flow efficiency based on the N_{weighted} numbers.

tNbC_mix	e-channel			μ -channel		
	N_{raw}	N_{weighted}	ϵ	N_{raw}	N_{weighted}	ϵ
No requirements	100000	100000.0	100.00%	100000	100000.0	100.00%
Trigger	90949	91065.2	91.07%	91243	91395.1	91.40%
Event DQ	89867	90071.8	90.07%	90154	90394.6	90.39%
Lepton (exactly 1 baseline)	17166	17314.6	17.31%	13606	13644.0	13.64%
Lepton (exactly 1 signal)	11918	11958.9	11.96%	11247	11258.1	11.26%
At least 3 jets ≥ 25 GeV	11119	11109.1	11.11%	10638	10626.9	10.63%
At least 4 jets ≥ 25 GeV	9018	9042.4	9.04%	8680	8733.0	8.73%
$\text{jet}_1 p_T \geq 80$ GeV	8492	8542.7	8.54%	8244	8317.8	8.32%
$\text{jet}_2 p_T \geq 70$ GeV	7111	7169.8	7.17%	6871	7000.0	7.00%
$\text{jet}_3 p_T \geq 50$ GeV	6044	6076.9	6.08%	5884	5985.5	5.99%
# b -tagged jets (70% eff.) ≥ 1	4977	4879.5	4.88%	4819	4787.9	4.79%
$\text{bjet}_1 p_T \geq 60$ GeV	4576	4446.0	4.45%	4445	4386.2	4.39%
$d\phi(\text{jet}_1, E_T^{\text{miss}}) \geq 0.6$	4459	4325.1	4.33%	4343	4281.1	4.28%
$d\phi(\text{jet}_2, E_T^{\text{miss}}) \geq 0.6$	4075	3953.3	3.95%	3970	3923.3	3.92%
$d\phi(\text{lepton}, E_T^{\text{miss}}) \geq 0.6$	3592	3494.2	3.49%	3500	3450.1	3.45%
$dR(\text{lepton}, \text{jet}_1) \leq 2.75$	2788	2706.2	2.71%	2729	2705.7	2.71%
$dR(\text{lepton}, \text{bjet}_1) \leq 3$	2673	2581.9	2.58%	2630	2607.8	2.61%
$E_T^{\text{miss}} \geq 270$ GeV	1286	1251.8	1.25%	1321	1307.6	1.31%
$E_T^{\text{miss}}/\sqrt{H_T} \geq 9 \sqrt{\text{GeV}}$	1285	1251.8	1.25%	1320	1306.6	1.31%
$m_T \geq 130$ GeV	1231	1205.8	1.21%	1270	1255.3	1.26%
$m_{jjj} \leq 360$ GeV	1118	1105.0	1.10%	1153	1143.7	1.14%
$am_{T2} \geq 190$ GeV	840	828.9	0.83%	821	827.8	0.83%
veto on tight τ 's	817	808.6	0.81%	807	811.5	0.81%
topness ≥ 2	804	793.6	0.79%	793	798.9	0.80%

Cut flow for tNbC_mix using a 100% stop $\rightarrow t\chi_1^0$ signal model with $m_{\text{stop}}=550$ GeV, $m_{\chi_1^0}=150$ GeV. The column labelled N_{raw} shows the results for the generated number of events, while N_{weighted} includes all correction factors applied to simulation and the pileup weights. The last column labelled ϵ shows the full cut flow efficiency based on the N_{weighted} numbers.

tNbC_mix	e-channel			μ-channel		
	N_{raw}	N_{weighted}	ϵ	N_{raw}	N_{weighted}	ϵ
No requirements	115297	115297.0	100.00%	115297	115297.0	0.69%
Generator filter (lepton)	80000	80000.0	69.39%	80000	80000.0	69.39%
Trigger	69610	69568.9	60.34%	69596	69595.6	60.36%
Event DQ	68794	68818.5	59.69%	68790	68859.4	59.72%
Lepton (exactly 1 baseline)	19352	19586.1	16.99%	16955	16945.7	14.70%
Lepton (exactly 1 signal)	13626	13854.3	12.02%	13737	13769.9	11.94%
At least 3 jets ≥ 25 GeV	13169	13378.5	11.60%	13256	13249.1	11.49%
At least 4 jets ≥ 25 GeV	11315	11551.6	10.02%	11457	11458.8	9.94%
$\text{jet}_1 p_T \geq 80$ GeV	11230	11467.5	9.95%	11359	11354.3	9.85%
$\text{jet}_2 p_T \geq 70$ GeV	10504	10704.5	9.28%	10680	10703.9	9.28%
$\text{jet}_3 p_T \geq 50$ GeV	9358	9554.9	8.29%	9573	9617.0	8.34%
# b -tagged jets (70% eff.) ≥ 1	8368	8143.9	7.06%	8648	8308.1	7.21%
$\text{bjet}_1 p_T \geq 60$ GeV	8225	7964.5	6.91%	8486	8114.2	7.04%
$d\phi(\text{jet}_1, E_T^{\text{miss}}) \geq 0.6$	7911	7662.4	6.65%	8177	7804.0	6.77%
$d\phi(\text{jet}_2, E_T^{\text{miss}}) \geq 0.6$	6862	6661.0	5.78%	7145	6850.0	5.94%
$d\phi(\text{lepton}, E_T^{\text{miss}}) \geq 0.6$	5007	4861.8	4.22%	5242	5007.5	4.34%
$dR(\text{lepton}, \text{jet}_1) \leq 2.75$	3893	3760.2	3.26%	4070	3889.8	3.37%
$dR(\text{lepton}, \text{bjet}_1) \leq 3$	3675	3527.5	3.06%	3857	3667.0	3.18%
$E_T^{\text{miss}} \geq 270$ GeV	705	678.2	0.59%	796	751.2	0.65%
$E_T^{\text{miss}}/\sqrt{H_T} \geq 9 \sqrt{\text{GeV}}$	698	670.8	0.58%	783	740.3	0.64%
$m_T \geq 130$ GeV	578	554.3	0.48%	663	630.3	0.55%
$m_{jjj} \leq 360$ GeV	469	433.7	0.38%	543	504.0	0.44%
$am_{T2} \geq 190$ GeV	377	350.1	0.30%	452	415.8	0.36%
veto on tight τ 's	367	341.5	0.30%	438	400.8	0.35%
topness ≥ 2	356	327.7	0.28%	411	368.7	0.32%

Cut flow for tNbC_mix using a 100% stop $\rightarrow b\chi_1^\pm$ signal model with $m_{\text{stop}}=550$ GeV, $m_{\chi_1^\pm}=300$ GeV, $m_{\chi_1^0}=150$ GeV. The generator lepton filter requires at least one stable electron or muon with $p_T > 10$ GeV and $|\eta| < 2.8$. The column labelled N_{raw} shows the results for the generated number of events, while N_{weighted} includes all correction factors applied to simulation and the pileup weights. The last column labelled ϵ shows the full cut flow efficiency based on the N_{weighted} numbers.

tNbC_mix	e-channel			μ-channel		
	N_{raw}	N_{weighted}	ϵ	N_{raw}	N_{weighted}	ϵ
No requirements	10000	10000.0	100.00%	10000	10000.0	100.00%
Trigger	9061	9053.3	90.53%	9068	9051.1	90.51%
Event DQ	8971	8969.9	89.70%	8975	8967.0	89.67%
Lepton (exactly 1 baseline)	1744	1760.9	17.61%	1407	1406.1	14.06%
Lepton (exactly 1 signal)	1189	1203.6	12.04%	1181	1173.8	11.74%
At least 3 jets ≥ 25 GeV	1123	1134.0	11.34%	1118	1097.0	10.97%
At least 4 jets ≥ 25 GeV	940	959.5	9.60%	894	879.0	8.79%
$\text{jet}_1 p_T \geq 80$ GeV	922	942.0	9.42%	874	866.3	8.66%
$\text{jet}_2 p_T \geq 70$ GeV	824	839.1	8.39%	770	769.6	7.70%
$\text{jet}_3 p_T \geq 50$ GeV	714	728.1	7.28%	677	665.7	6.66%
# b -tagged jets (70% eff.) ≥ 1	611	603.6	6.04%	574	540.2	5.40%
$b\text{jet}_1 p_T \geq 60$ GeV	573	563.6	5.64%	545	505.9	5.06%
$d\phi(\text{jet}_1, E_T^{\text{miss}}) \geq 0.6$	550	540.5	5.41%	524	479.6	4.80%
$d\phi(\text{jet}_2, E_T^{\text{miss}}) \geq 0.6$	490	482.2	4.82%	471	439.8	4.40%
$d\phi(\text{lepton}, E_T^{\text{miss}}) \geq 0.6$	405	399.4	3.99%	380	352.7	3.53%
$dR(\text{lepton}, \text{jet}_1) \leq 2.75$	323	320.5	3.20%	296	285.5	2.86%
$dR(\text{lepton}, b\text{jet}_1) \leq 3$	309	304.2	3.04%	281	266.8	2.67%
$E_T^{\text{miss}} \geq 270$ GeV	94	92.4	0.92%	110	107.1	1.07%
$E_T^{\text{miss}}/\sqrt{H_T} \geq 9 \sqrt{\text{GeV}}$	94	92.4	0.92%	110	107.1	1.07%
$m_T \geq 130$ GeV	83	80.2	0.80%	99	95.5	0.96%
$m_{jjj} \leq 360$ GeV	71	67.6	0.68%	81	78.4	0.78%
$am_{T2} \geq 190$ GeV	61	59.9	0.60%	65	63.6	0.64%
veto on tight τ 's	60	58.5	0.58%	63	60.5	0.61%
topness ≥ 2	56	52.3	0.52%	61	58.0	0.58%

Cut flow for tNbC_mix using a 100% tNbC signal model with $m_{\text{stop}}=550$ GeV, $m_{\chi_1^\pm}=300$ GeV, $m_{\chi_1^0}=150$ GeV. The column labelled N_{raw} shows the results for the generated number of events, while N_{weighted} includes all correction factors applied to simulation and the pileup weights. The last column labelled ϵ shows the full cut flow efficiency based on the N_{weighted} numbers.